High Resolution for X-ray Spectroscopy Studies with Highly Charged Heavy Ions at the CRYRING@ESR Electron Cooler

seit 1558

DISSERTATION

zur Erlangung des akademischen Grades

doctor rerum naturalium (Dr. rer. nat.)

vorgelegt dem Rat der Physikalisch-Astronomischen Fakultät

der Friedrich-Schiller-Universität Jena

von Dipl.-Phys. **Binghui Zhu**

geboren am 29. Oktober 1993 in Anhui, China

Gutachter:

1. Prof. Dr. Thomas Stöhlker, Friedrich-Schiller-Universität Jena
2. PD Dr. Wolfgang Quint, GSI Helmholtzzentrum für Schwerionenforschung GmbH
3. Prof. Dr. Andrey Surzhykov, Physikalisch-Technische Bundesanstalt

Tag der Disputation: 10. Januar 2023

Zusammenfassung

In dieser Arbeit berichte ich über die erste röntgenspektroskopische Untersuchung des Prozesses der radiativen Rekombination (RR) für nackte Blei-Ionen (Pb^{82+}) am Elektronenkühler des CRYRING@ESR-Speicherrings, der kürzlich an der GSI/FAIR installiert und in Betrieb genommen wurde. Die Kopplung des CRYRING, der sich ursprünglich im Marne-Siegbahn-Labor in Stockholm befand, mit dem Experimentier Speicherring (ESR) der GSI-Beschleunigeranlage ermöglichte es uns zum ersten Mal, hochgeladene Schwerionen im CRYRING@ESR zu speichern und die Röntgenstrahlung zu untersuchen, die durch ihre Wechselwirkung mit Elektronen aus dem ultrakalten Elektronenkühler entsteht. Dazu wurden die Pb^{82+}-Ionen im ESR von der Injektionsenergie von 400 MeV/u auf 10 MeV/u abgebremst und anschließend zum CRYRING@ESR transferiert, dort gespeichert und gekühlt. Der Nachweis der im Kühler emittierten Röntgenstrahlung wurde durch die Installation spezieller Kammern für die Montage von Röntgenfenstern im geraden Kühlerabschnitt des Speicherrings bei Beobachtungswinkeln von 0° bzw. 180° ermöglicht. Darüber hinaus wurde die Röntgenemission in Koinzidenz mit umgeladenen Pb^{81+}-Ionen aufgezeichnet, was sehr saubere Röntgenspektren ohne Kontamination durch Hintergrundstrahlung, die nicht mit dem gespeicherten Ionenstrahl korreliert ist, ermöglicht.

Eine detailierte, zeitabhängige Modellierung der beobachteten Röntgenspektren ermöglichte es, die detaillierten aufgenommenen Spektren quantitativ zu reproduzieren. Neben den prompten Rekombinationsübergängen für RR in die K-, L-, und M-Schalen werden alle charakteristischen Röntgenemissionsmerkmale, wie die beobachteten Lyman-, Balmer- und Paschen-Linien, durch das angewandte Modell gut beschrieben. Diese Ergebnisse wurden durch die vorteilhaften Eigenschaften des Röntgenspektroskopieaufbaus am CRYRING@ESR Elektronenkühler ermöglicht. Zu nennen sind hier beispielsweise die Beryllium-Vakuumfenster, die eine hohe Transmission auch für Röntgenstrahlen im Bereich von wenigen keV ermöglichen, sowie die ausgezeichnete Gesamtleistung des CRYRING@ESR, der sehr gut definierte elektronengekühlte Pb^{82+}-Strahlen bei einer Energie von nur 10 MeV/u liefert. Darüber hinaus ermöglichte die genau definierte Beobachtungsgeometrie die Beobachtung aller Röntgenlinien ohne Verzerrungseffekte und ohne nennenswerte Doppler Verbreiterung. Infolgedessen konnten sogar die komplette Balmer-Serien und die Paschen-

Linien eines Hoch-Z Elements zum ersten Mal unverzerrt in der Kühlsektion von CRYRING@ESR beobachtet werden.

Aus diesen Ergebnissen folgt, dass der RR Prozess an Elektronenkühlern gut für die detaillierte Präzisionsspektroskopie schwerer hochgeladener Ionen genutzt werden kann. Wie in der vorliegenden Studie gezeigt wurde, werden die relativen (n, l) Populationskoeffizienten bei den hier gegebenen niedrigen Relaitivgeschwindigkeiten zwischen Elektronen und Ionen nur geringfügig durch eine Variation der Kühlertemperatur beeinflusst, da RR bei niedrigen relativen Energien hohe Quantenzustände begünstigt, was schließlich zu einer Yrast-Kaskaden-Kette führt, wie sie im aktuellen Experiment beobachtet wurde. Darüber hinaus stellen wir fest, dass ein großer Teil der Elektronen, die über RR in die angeregten Niveaus der Ionen eingefangen wurden, innerhalb unserer experimentellen Beobachtungszeit von etwa 70 ns den Grundzustand erreicht haben. In der Tat beweist unser Experiment, dass der Hauptbeitrag zur Röntgenemission von RR-Zuständen mit Hauptquantenzahlen bis zu etwa $n = 100$ stammt.

Darüber hinaus wurden in dieser Arbeit erste vorläufige Ergebnisse einer experimentellen Untersuchung der Strahlungszerfallsmodi von hohen Ryberg-Zuständen zur Bildung von sequentiellen Balmer-Serien und $L \rightarrow K$ übergängen in U^{90+}-Ionen vorgestellt. In diesem Experiment wurde die zustandsselektive Population der Substruktur in angeregten Zuständen über RR von ursprünglich H-artigem Uran mit hoher Auflösung untersucht. Dies wurde durch den Einsatz von zwei hochgranularen, neuartigen hochauflösenden maXs-100 Detektoren erreicht, die unter 0° und 180°-Beobachtungswinkeln in Bezug auf die Ionenstrahlrichtung platziert wurden. Die vorläufigen Daten belegen erneut das einzigartige Potenzial der experimentellen Methode der Röntgenspektroskopie am Elektronenkühler von CRYRING@ESR und unterstreichen die Bedeutung des oben vorgestellten Kaskadensimulationsprogramms für die Interpretation und Modellierung der gemessenen Röntgenspektren.

Contents

Chapter 1

Introduction

Radiative recombination occurring in electron-ion collisions is one of the most fundamental processes which was barely possible to be observed in the laboratory in the beginning of the 1980s. Then, revolutionary development came at the end of the 1980s with the advent of heavy-ion cooler storage rings [1, 2, 3] and electron beam ion traps (EBITs) [4, 5]. These devices allow to investigate reactions between electrons and ions for almost any charge state with high resolution as well as with increased signal-to-background ratio, and with high luminosity. Storage rings, in particular, have the strength to investigate radiative recombination in the low impact energy range. One particular advantage is that they enable us to perform photon spectroscopy studies of elementary atomic processes. The CRYRING@ESR storage ring [6], shipped from the Manne Siegbahn Laboratory in Stockholm to Darmstadt as a Swedish in-kind contribution to FAIR [1] (see [7] and references therein), has the potential of an excellent energy resolution and the selectivity in ion charge states as well as the easy detection of recombined ions.

Stored highly charged ions offer the unique possibility to analyze the main constituents and evolution of typical astrophysical plasmas, and to pursue detailed studies of electronic transitions, and of collisional processes and to investigate their influence on the level population and the emission of characteristic radiation. In addition, highly charged heavy ions provide a distinctive probe for our understanding of relativistic particle dynamics in the presence of extreme electromagnetic fields. Here, elementary atomic processes like photoionization in the relativistic domain can nowadays be studied by its time-reversal process, i.e. the radiative recombination process (RR), with an accuracy which is otherwise inaccessible [8].

The reason for studying RR of electrons with bare or few-electron ions is due to several practical applications and fundamental questions. The applications are in plasma physics or in astrophysics where electron-ion recombination and their spectroscopy play an important role [9], e.g. population dynamics, ionization equi-

[1] Facility for Antiproton and Ion Research in Europe GmbH, Planckstraße 1, D-64291 Darmstadt, Germany.

librium, and radiative power losses, also of high practical relevance is electron cooling itself, where recombination could cause significant ion beam losses and is expected to be useful for the diagnosis of the beam properties. For fundamental studies two classes of highly charged ions are presently most interesting: the one-electron (H-like) ions and the two-electron (He-like) ion species. The quantum mechanics of the H-like ions is well understood so that they provide the best testing ground for strong QED effects in extreme electromagnetic fields [10]. The understanding of the two-electron systems is a necessary precursor for developing theoretical models for many electron systems. With the extension from H and He atoms to highly charged ions at high atomic number Z, a more systematic investigation is indispensable since the relative contributions of atomic structure corrections vary, such as correlation or QED effects. These effects can be deduced from x-ray spectroscopy by the detection of RR photons and characteristic x-rays from highly ionized high-Z species.

Most of the RR experiments were performed at electron cooler devices of storage rings for the low velocity regime [11, 12, 13, 14]. In this process a free electron undergoes direct transition into a bound state of a stationary ions via emission of a photon, carrying away the energy difference between the initial (continuum) and final (bound) electronic state. At such low-relative velocities, states with large principle and angular momentum quantum number (n, l) are predominantly populated, which then decay radiatively forming characteristic projectile x-rays from these high Rydberg levels via radiative cascades [15, 16]. At the ESR storage ring in Darmstadt, the very first x-ray emission study for initially bare gold ions due to RR process was conducted in the electron cooler [17]. In this experiment, in particular, a very strong cascade contribution feeds the L-shell levels and subsequently results in relative intense Lyman-α emission [15, 17]. Afterwards, an application of deceleration mode in the ESR was used to reduce tremendously the ion beam energy, and enabled the efficient production of characteristic x-rays under almost background free conditions, thus allowing for a state-selective investigation of the L-RR [18, 19] and the characteristic Balmer transitions [18, 20] at the low-energy part of the spectra.

Since 2020, the CRYRING@ESR storage ring has been fully commissioned with beams from an independent local ion injector as well as for all ion species presently accessible in the ESR storage ring by using the full GSI accelerator chain. As discussed in detail in the current thesis, recently the first x-ray spectroscopy production runs for a real high-Z ion, namely hydrogen-like lead provided by the ESR, was successfully conducted at the electron cooler of the CRYRING@ESR. By utilizing dedicated x-ray detection chambers installed at 0° and 180° observation geometry [21] while maintaining the ring of typically 10^{-11} mbar ultra-high vacuum (UHV) environment, it enabled us to observe the full x-ray emission pattern for a wide energy range, spanning from prompt RR transitions into the K-, L- and M-shells to

the subsequent radiative deexcitation cascades forming well resolved Lyman, Balmer and Paschen series. Most remarkably, the x-rays are detected without any line distortion effects which might be caused mainly by delayed x-ray emission affecting in particular the Lyman-α transitions as observed in previous experiments at the ESR [18, 19, 22, 23]. Further on the current thesis lays the basis for a successful effort to push the experimental resolution of x-ray spectroscopy for $L \rightarrow K$ ground-state transitions at high-Z of below 80 eV at about 100 keV. This was done in an RR experiment of free electrons into the bound states of U^{91+} ions by adopting low-temperature x-ray detectors [24]. Such an experiment allowed us for the first time to resolve the substructure of the $K\alpha_2$ line and partially the $K\alpha_1$ line in U^{90+} ions.

This PhD work essentially reports about x-ray production processes: recombination of free electrons and highly charged heavy ions at zero relative electron-ion velocity (on average) in an electron cooler, and the investigation of the prevalent cascade decay dynamics to gain more insight into the final state populations of the recombination process itself both for H-like and He-like heavy ions.

The thesis is organized as follows:

• Chapter 2 widely describes the experimental environment of GSI, in which the measurements have been taken place. The accelerator facilities, the storage rings and the technique of electron cooling are presented. The current progress in the basic field of atomic structure research involving high-Z ions is closely related to the application of both advanced ion sources and advanced accelerator and storage techniques.

• Chapter 3 gives a short introduction to the structure of one- and few-electron systems, which includes also a detailed discussion of the scaling of radiative transition rates for the most probable electronic transitions.

• Chapter 4 establishes in a brief way the theoretical frame of the work. Here, the main processes that lead to projectile x-ray production are discussed. The importance of understanding and using these theoretical tools is emphasized, in order to analyze and predict atomic physics related phenomena.

• Chapter 5 reveals the role of radiative feeding transitions followed by RR of bare lead ions with cooling electrons to the formation of observed intense Lyman and Balmer lines. For this purpose, an elaborate theoretical model for the radiative decay dynamics for each (n, l, j) state population is developed and tested in detail by comparison with the experimental data. As a result, the presented rigorous treatment reproduces the observed line intensities for RR and characteristic x-ray transitions very well. Also, a strong enhancement for $l = n - 1$ states in inner shells due to radiative cascades from high Rydberg states is found, which contributes strikingly to the observed intensities of characteristic x-ray lines, e.g. Lyman-$\alpha_{1,2}$.

• Chapter 6 describes the state-selective x-ray studies associated with RR of U^{91+} ions with free electrons at threshold energies. Moreover, for future application of the

established radiative cascade simulation program a prediction of the population of excited projectile substate (n, l, j) is presented for the case of U^{90+} ions. Emphasize is given particularly to the formation of $^3S_1$ and $^3P_1$ levels, as the substructure of $K\alpha_2$ transition line was resolved for the first time by using novel high-resolution microcalorimeters. Up to now, rare experimental information about $K\alpha_2$ substructure in the domain of medium-Z and high-Z helium-like ions is available.

• Chapter 7 summarizes the work presented in this thesis and chapter 8 gives an outlook on future studies.

Chapter 2

The experimental environment

The measurements presented in this work were carried out at the electron cooler of the CRYRING@ESR storage ring complex at GSI by utilizing the free cooler electrons as target. In the following the production and storage of highly charged heavy ions at GSI SchwerIonen Synchrotron SIS and the Experimental Storage Ring ESR are discussed. Particular emphasis is given to ion beam cooling, beam extraction from the ESR to the CRYRING@ESR and to detectors with high energy resolution and large energy bandwidth dedicated to RR x-ray spectroscopy.

2.1 Production of highly charged heavy ions

The production of highly charged ion beams is a difficult task, due to the increase in binding of inner shell electrons ($E_n \sim \mathrm{Ry} \cdot Z^2/n^2$). To ionize inner shell electrons in heavy atoms, corresponding high energy or momentum transfers are needed. For photons, the necessary high flux at high energies are presently not available for the efficient ionization. Currently, only impact ionization in collisions with atoms or electrons can provide sufficient numbers of highly charged heavy ions for experiments. For instance, uranium K-shell electrons ($E_k \approx 132$ keV) can be removed efficiently in atomic or electronic collisions at energies beyond 200 MeV/u (atomic collisions) or 150 keV (electronic collisions).

In heavy ion accelerators the highly-charged ions are produced by stripping, i.e. ionization by heavy particle impact. With the increase of the accelerator beam energy over the last 40 years, heavier and heavier systems were made accessible to scientific research. At the GSI accelerator facility [25, 26], all heavy ion species across the periodic table, up to naked U^{92+}, can now be produced with reasonable intensities. Here, in an injector, heavy ions are accelerated to high energies and then stripped before they are accumulated in an ion storage ring. The layout of the accelerator facility and experimental area at GSI (Germany) are displayed in Fig. 2.1.

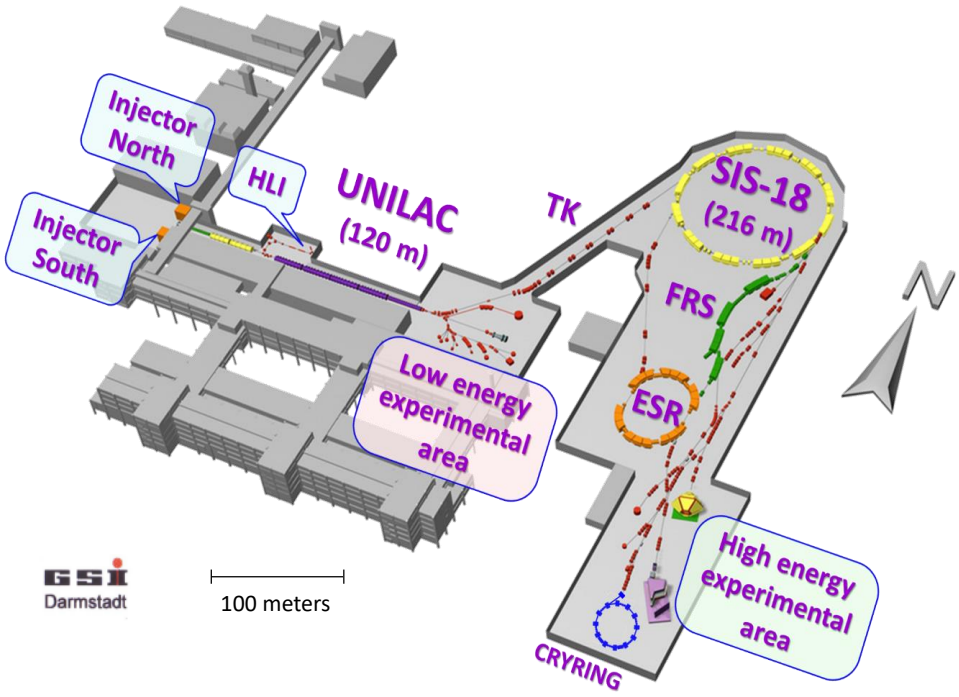

Figure 2.1: Layout of the heavy ion accelerator facility and experimental areas at GSI in Darmstadt.

2.1.1 Comparison between electron beam ion trap and storage rings

An alternative method to produce heavy few-electron ions is the successive ionization of confined ions by continuous energetic electron bombardment as it is realized in an electron beam ion trap devices (EBIT) [4, 27], in which the ions are confined by magnetic and electric fields in a dedicated ion trap. If the electron energy is sufficiently high, the trapped ions will consecutively be ionized until they have lost even their last electron, provided that recombination is less probable compared to the electron loss process. In particular, the Doppler effect which is often the limiting factor for accelerator-based spectroscopy is not the dominant source of uncertainties for an EBIT-based spectroscopy. The main drawback here is the limit in ionization power for the innermost electrons in heavy ions. Bare and H-like ions of e.g. lead or uranium are difficult to produce. As schematically shown in Fig. 2.2 the Super-EBIT device in Livemore, the electron beam energy was turned up to about 198 keV, which in uranium is well above the ionization energy for the last K-shell electron [28], however, only a small number of bare U^{92+} ions had been produced inside the EBIT.

In storage rings, which can also be considered as traps for ions at high energies, the drawback of charge-state mixing is clearly avoided by utilizing bending magnets for q/A separation. Here, q and A denote the ionic charge and mass number, respectively. However, the high ion velocity may cause via the Doppler effect restric-

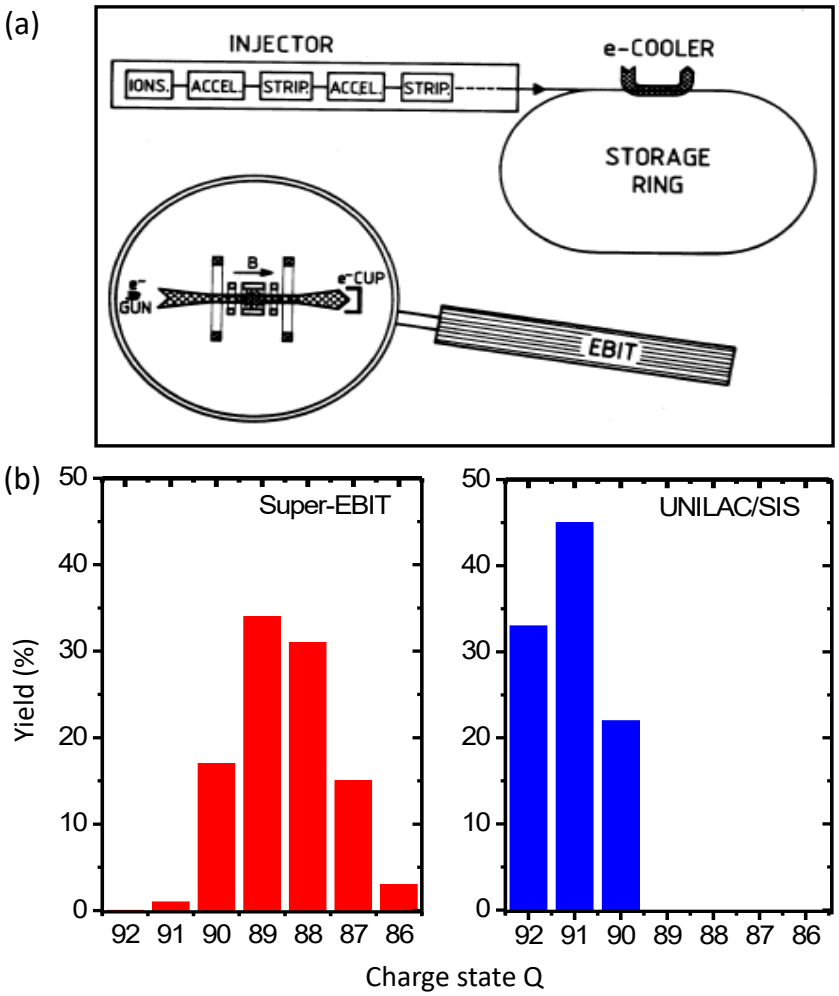

Figure 2.2: Two methods to produce highly-charged heavy ions in (a) [29]. Top: the storage ring technique, where ions are accelerated to high energies and then stripped to high-charge states before they are stored and cooled in a huge ring. Bottom: the EBIT technique, where ions stored in a small trap are continuously ionized by a very dense, high energy electron beam to high ionization stages. Charge-state distributions for uranium ions in (b). Left: trapped, stationary uranium ions by continuous 198 keV electron beams bombardment in Super-EBIT [28]. Right: Fast moving uranium ions penetrate through a 100 mg/cm^2 thick Cu stripper foil at 360 MeV/u ($\beta \approx 0.69$) in UNILAC/SIS complex [8].

tions for precision experiments. On the other hand, decelerating of fast few-electron projectiles at an accelerator after stripping will certainly allow a Doppler-reduced accelerator-based spectroscopy. Hence, really high intensities of the heaviest and ultimately charged ions can be provided by the acceleration-stripping-decelerating-storing technique. In the storage ring at the heavy ion accelerator facility at GSI in Darmstadt, up to 10^8 bare U^{92+} ions had been stored already for experiments in the ESR storage ring. To strip the heavy ions to the necessary high-charge states before injection into the ring, one must accelerate them to velocities corresponding to about the orbital velocities of the most strongly bound electrons of concern (Bohr criteria). For fast uranium ions, energies between 250 and 500 MeV/u are needed to

produce sufficiently high fractions of completely stripped ions [30]. In this case, the acceleration-stripping technique has to be applied in several stages, as is indicated in Fig. 2.2.

The stripping technique will certainly increase the emittance of the ion beam which means it will become more divergent, i.e. slightly hotter. Such a stored ion beam will further heat up by intra-beam scattering and distant collisions with the remnant gas molecules in the ring. Hence, the advent of efficient beam cooling techniques [31, 32] was crucial for the prosperous development of x-ray spectroscopy study at heavy-ion storage rings. By various beam cooling techniques and in particular electron cooling, stored heavy ion beams can be cooled down to low emittances. Thus, even for high intensity beams, all highly charged ions have almost exactly the same velocity vector, and the ions are confined to a small beam diameter. The cooling techniques fix the ion velocity with extreme stability over long time periods. It also counterbalances the energy loss of the ions colliding with remnant gas atoms and molecules. Beam cooling is the prerequisite for heavy ion storage rings providing high luminosity beams of ultimately charged heavy ions even for precision spectroscopy investigation. Moreover, in a ring the charge states of the ions are well defined and accessible to experiments before and after any reactions.

2.2 Ion beam cooling

Cooling of an ion beam means a decrease of the four equivalent quantities, i.e. phase-space volume, emittance, temperature and entropy. It does not violate Liouville's theorem or the second law of thermodynamics because beam cooling couples to an outer system with additional degree of freedom. The coupling can be provided by different mechanisms resulting in various cooling techniques like radiation self cooling, laser cooling, stochastic cooling and electron cooling. For the case of heavy ions, cooling by light-pressure and by synchrotron radiation damping can be neglected. The following will concentrate on a short review of stochastic cooling which applies self-correction of ion trajectory, and electron cooling where the coupling mechanism is maintained by Coulomb collisions.

At the ESR, stochastic cooling [33, 34] is mainly used as a precooling stage for secondary beams after storing. Hot beams of projectile fragments (secondary ions) are produced in a rather thick target and selected by a magnetic separator FRS (see Fig. 2.1). For the cooling of 10^8 bare U^{92+} fragment ions at 400 MeV/u precooling will start at a transverse emittances of $\epsilon = 20\pi$ mm mrad and a momentum spread of $\Delta p/p \sim 10^{-3}$. Electron cooling [35, 36] is applied at $\epsilon = 2\pi$ mm mrad and $\Delta p/p \sim 10^{-4}$. The final values of $\epsilon = 0.1\pi$ mm mrad and $\Delta p/p \sim 10^{-5}$ are reached by consecutive application of stochastic cooling and electron cooling. For this procedure, a time of about a few-second is necessary as shown in Fig. 2.3.

After about 3 s of stochastic cooling and subsequent electron cooling, an extremely well-cooled beam, i.e. well defined beam with respect to energy and momentum definition, can be observed 5 s after injection.

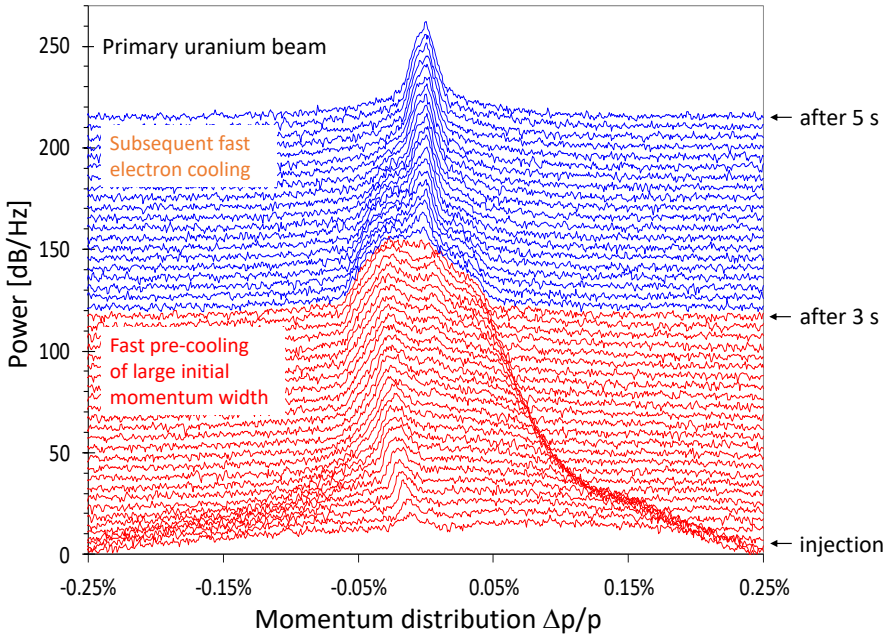

Figure 2.3: Waterfall diagram of the Schottky power density for a circulating beam of 400 MeV/u U^{92+} ions at the ESR storage ring [37]. The broad distribution refers to the uncooled initial beam, the distributions in red denote stochastic precooling measured after injection into the ESR. The blue narrow distributions reflect the momentum profiles of a continuously cooled ion beam.

2.2.1 Stochastic precooling

Using a pick-up probe, the position of the ion beam can be measured at a fixed position via the induced electronic signal. A deviation of the beam from the ideal orbit can be corrected by the amplification of this signal. This amplified signal can now be used as a correction signal which acts on the beam at a second position via a "kicker", as schematically depicted in Fig. 2.4 (a). This method was invented for the cooling of hot antiprotons by Van der Meer [38, 39]. He was able to show that after a cooling time of $\tau \propto N/C$ (N: Particle number, C: Bandwidth of the amplifier) a momentum width of the beam of about $\Delta p/p \sim 10^{-3}$ can be achieved by stochastic cooling. For details, the principle of these techniques was comprehensively summarized in the literature [40, 41].

The stochastic cooling system at the experimental storage ring ESR had been used for various experiments with stored radioactive and stable fragment beams. They arrive from the fragment separator with momentum spreads and emittances for which electron cooling is too slow. Both longitudinal and transverse stochastic cooling have been demonstrated in Fig. 2.4 (b). In stochastic cooling, the mean

position of a small bunch of particles in the phase space is measured, and then this bunch is transferred by active kickers to the correct spot, i.e., to the center of the emittance ellipse. Stochastic cooling is particularly appropriate for hot beams, i.e., beams with large emittances. This is, for instance, important if the reaction products from nuclear reactions (exotic nuclei) are accumulated in the ring. At the ESR, stochastic cooling installed in 1990th had successfully demonstrated its efficiency to cool a mixture of different ion species [33, 34, 42] from the fragment separator FRS placed between SIS and ESR (see Fig. 2.1).

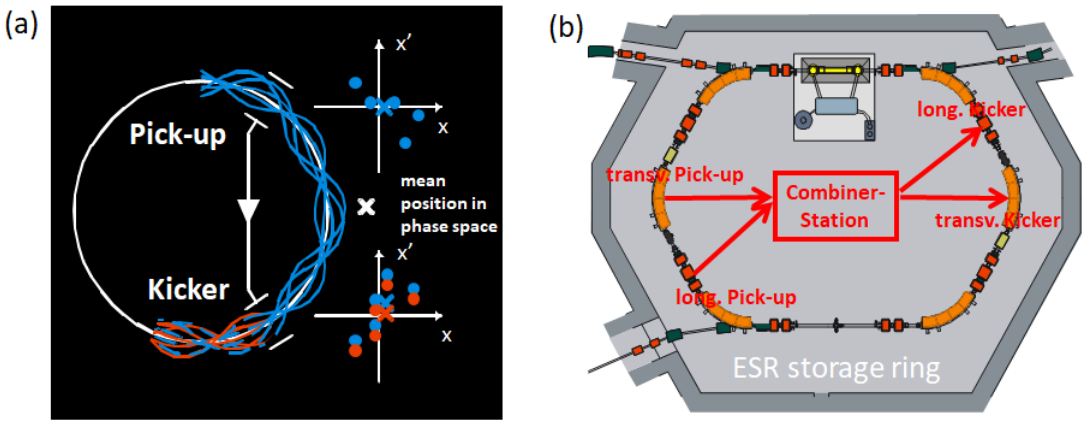

Figure 2.4: (a) A cartoonist's view of a transverse stochastic cooling system. (b) Layout of the ESR with stochastic cooling lines.

2.2.2 Electron cooling

Cooling a heavy-ion beam is a fascinating idea because it offers a number of advantages. It was in 1966 when Budker [43] was the first to point out that a cold beam of electrons moving at the same velocity parallel to the hot ion beam on a straight section of the ring could provide a refrigerant. It compensates various unavoidable heating processes like intra-beam scattering, focusing errors, small angle scattering and energy loss in an internal target introduced into a storage ring for experiments. This results in a lower equilibrium ion temperature and in larger storage time. For experiments the more brilliant beams mean higher event rates and at the same time a minimal kinematic broadening of particle and radiation spectra.

Electron cooling is based on the exchange of energy between the ion beam and a low-temperature beam of electrons having the same velocity as the ions [44]. The basic principle of electron cooling of a stored beam of ions is sketched in Fig. 2.5 with the utilization of an electron cooler. Over a fraction of the circumference of the storage ring, for instance the ESR or CRYRING, the ions are merged with a stream of continuously refreshed cold electrons. The mean electron velocity in the laboratory system $\langle v_{e,lab} \rangle$ is tuned to the mean ion velocity $\langle v_{i,lab} \rangle$, and the electron

temperature T_e is less than the ion temperature T_i. The dissipative force introduced via Coulomb interactions between electrons and ions leads to a heat exchange and, in the absence of processes heating the ions, to an equilibration of the temperatures $T_i = T_e$. Because of the high mass m_i of a heavy ion as compared to the electron mass m_e the ion velocity in the co-moving system can be very small

$$\langle v_i^2 \rangle = \frac{m_e}{m_i} \langle v_e^2 \rangle , \tag{2.1}$$

and accordingly the divergence and momentum spread of the ion beam can be small as compared to those of the electron beam. For a comprehensive compilation of the theoretical understanding and the technical developments in electron cooling, one can refer to the workshop [45] on beam cooling and related topics held at CERN in Switzerland.

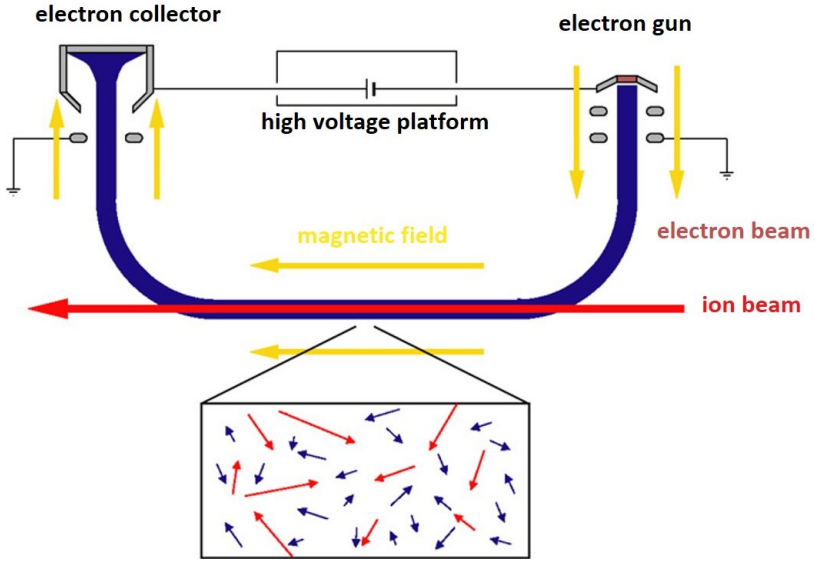

Figure 2.5: The principle of electron cooling in an ion storage ring: a stream of cold electrons moving collinearly with the ion beam over a fraction of the circumference serves as a refrigerant.

2.3 Experimental storage rings ESR and CRYRING

The coupling of ESR and CRYRING@ESR storage ring complex serves as the platform for the experiment, as shown in Fig. 2.6, since the CRYRING here can be used to perform experiments with cooled ions, while the ESR prepares the next ion bunch. Usually, 400 MeV/u bare Pb ions from the heavy-ion synchrotron SIS18 were injected into the storage ring ESR and then compressed into a small phase space volume with typical momentum spread of $\Delta p/p \sim 10^{-5}$ by combined stochastic and electron cooling [32]. Thereafter, the ions were decelerated down to 10 MeV/u, electron cooled again. This is followed by the extraction of the ions out of the ESR and injection into the CRYRING@ESR.

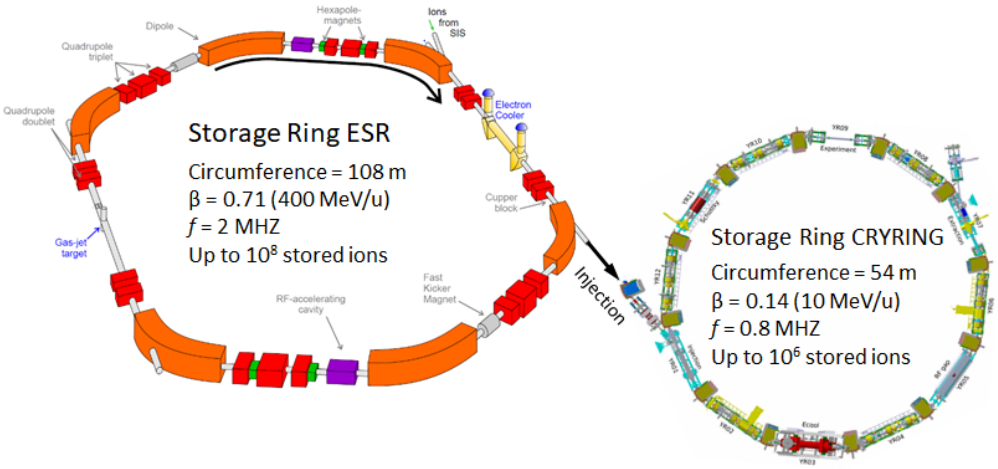

Figure 2.6: Schematic sketch of the coupling of ESR and CRYRING@ESR storage ring at GSI-Darmstadt. The layout of ESR depicts the beam guiding system (dipole bending magnets, quadrupoles and hexapoles) as well as the most important installations for beam handling and disgnostics kicker, rf cavities, Schottky noise pick up, electron cooler. The layout of CRYRING@ESR will be depicted seperately in Fig. 2.7.

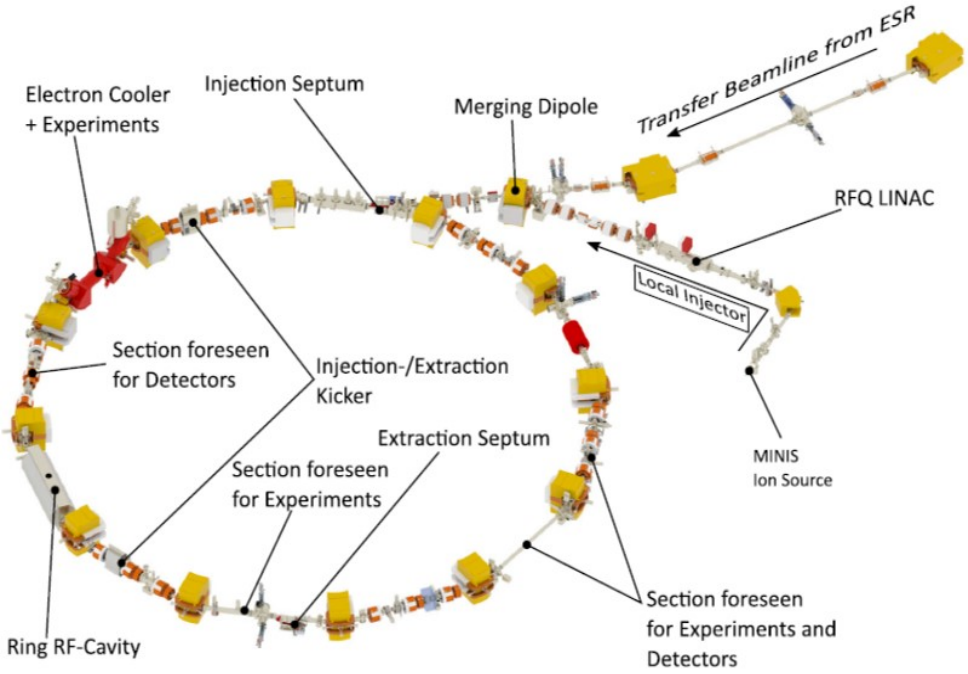

Figure 2.7: Overview of the main CRYRING@ESR facilities including the local injector, the transfer beamline from ESR and ring sections where experimental installations and/or particle detectors will be placed [46].

Both ESR and CRYRING@ESR are very flexible experiment facilities and offer unique possibilities for a large number of experiments in the realm of atomic, quantum and fundamental physics based on electronic, photonic, or atomic interactions [6]. A full technical description of the original CRYRING setup in its original form at the Manne Siegbahn Laboratory at Stockholm University in Sweden is given by

Danared *et al.* [47]. To further leverage its capabilities into the realm of intense beams of highly charged ions, exotic isotopes, and of antiprotons, the ring was modernized and adapted to the GSI/FAIR standards [48, 49] and installed downstream of the ESR. At its new location downstream of ESR (see Fig. 2.1), all ion species presently accessible in ESR can be transferred to the CRYRING, in which ions with rigidity between 0.054 and 1.44 Tm can be stored. The original Swedish layout has been modified by reconfiguring the sequence of straight sections and by slightly increasing the circumference to ESR/2. Ions can be injected from ESR or from an independent 300 keV/u RFQ test injector. A closer view of the new CRYRING installations can be seen in Fig. 2.7 [46].

Table 2.1: Operation parameters of CRYRING@ESR with heavy ions from SIS18/ESR facility [6, 46].

Circumference	54.17 m (ESR/2)
Bending radius in 30° dipole magnets	1.2 m
Rigidity at injection	
– for p, $\bar{p}$	0.08 Tm
– for heavy ions	1.44 Tm
Highest possible injection energy	
– for p, $\bar{p}$	30 MeV (capped by radiation safety)
– for $^{12}C^{6+}$	24.7 MeV/u
– for $^{238}U^{92+}$	14.8 MeV/u
Lowest rigidity	0.054 Tm
Lowest energy	charge exchange limited
Ion beam lifetimes	3 s - 15 min
Magnetic ramping (de- and acceleration)	1 T/s (4 T/s, 7 T/s)
Vacuum pressure (N_2 equiv.)	10^{-11} – 10^{-12} mbar
Beam injection	multi-turn and fast
Beam extraction	slow and fast
Local injector beamline	
– for $A/q > 2.85$	40 keV/q
– for $A/q \leq 2.85$	300 keV/u (RF-power limited)

Table 2.1 summarizes the operation parameters of CRYRING@ESR. The instrumentation of the ring includes an RF drift tube system for acceleration and deceleration (1 T/s, with a possibility for an upgrade to 7 T/s), electron cooling, a free experimental section, and both fast and slow extraction of ions. The ring is arranged in a sixfold symmetry with every second straight section implementing beam focusing through a set of quadrupole triplets and with two sextupoles for correcting chromaticity [50] (not denote in Fig. 2.7). CRYRING@ESR can store, cool and decelerate heavy, highly charged ions down to a few keV/u, which ranges ideally below the lower limit of ESR operation. The ions are kept in orbit by twelve 30° magnetic dipoles and a number of quadrupoles. The ring features also excellent vac-

uum conditions to achieve ion beam lifetimes of several seconds to minutes for even the highest charge states of ions. It is equipped with a high-performance electron cooler, as well as with an internal gas-jet target. Moreover, an independent injector beam-line allows for standalone operation during commissioning and prototyping. Hence, with dual injection, beams can be either injected from ESR or independently from a local ion source. The local source is set up in a 40 kV high-voltage platform and connected to a 300 keV/u RFQ accelerator (for $A/q \leq 2.85$).

2.3.1 The transfer beam-line from ESR

A schematic overview of the ESR-CRYRING@ESR transfer beam-line is depicted in Fig. 2.8 with a length of almost 100 m, and fast extraction is used in the transfer of beam from one circular ring to another [51]. As ESR is not equipped with a dedicated kicker magnet for fast extraction towards CRYRING, the extraction is performed with the existing injection kicker magnet of ESR applying a particular closed orbit detuning [48]. In August 2014 a beam of 30 MeV/u $^{14}N^{7+}$ ions [52] was used to test the complete ESR-CRYRING@ESR beam transfer line and to optimize beam-line settings. At each energy via step-wise deceleration down to 4 MeV/u, the beam was successfully extracted, varying only the kick angle of the injection kicker, and the distortion orbit was unchanged.

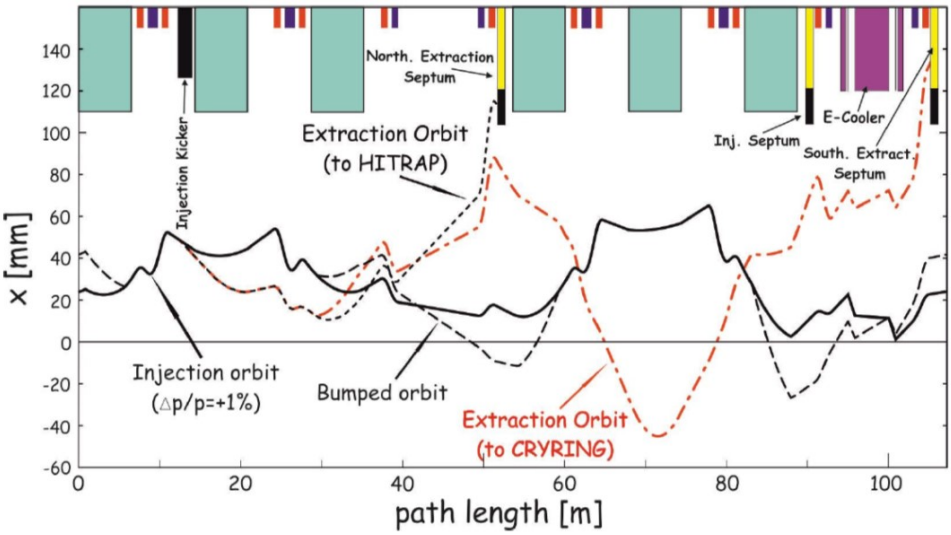

Figure 2.8: Schematic overview of the ion beam fast extraction from ESR to CRYRING@ESR [53]. The black solid and dashed lines refer to injection and bumped orbit, the extraction orbit to HITRAP [54] and CRYRING are indicated by black dotted and red dash-dotted lines, respectively.

The reason for the installation of CRYRING@ESR at GSI are experiments with slow, highly-charged ions being transferred through ESR from the GSI accelerator chain. The very first commissioning run experiment with bare Pb^{82+} ions from the ESR transferred to CRYRING@ESR was conducted successfully in spring beam

time of 2020, as beams with useful intensities enable us to accumulate meaningfully spectral information when combining the signals from x-ray detectors and particle counter. In late April 2021, the second experiment using beams from the ESR, focusing on the x-ray spectroscopy of He-like uranium ions, was partially demonstrated. There, intensities of about 2×10^6 ions of U^{91+} could be transferred from ESR and stored in CRYRING@ESR. Dominant losses ($> 90\%$) were observed already during deceleration and subsequent electron cooling in the ESR before extraction. It should be also noted that the space charge limit of CRYRING@ESR is nearly 2 orders of magnitude above the reached intensities and that injection efficiency of beams delivered to CRYRING@ESR was near 100%. Thus, the deceleration efficiency and reliability as well as the beam lifetimes need further substantial improvement for the next upcoming beam times.

2.3.2 The electron cooler

In the present experiment the CRYRING@ESR electron cooler serves a twofold task: first, phase-space cooling of the ion beam and, second, the use of the as a target of electrons to study the recombination processes. For cooling, the electron beam energy is tuned to match the velocity of electrons to the velocity of ions on average. Since the electron beam is cold and used in single pass, on average the momentum spread of the initially hot ion beam approaches the momentum spread of the electron beam and a net cooling effect of the ion beam can be observed, leading to an increased phase space intensity and a much better defined ion momentum with $\Delta p/p$ reducing from $\sim 10^{-3}$ of initially stochastic precooling to $\sim 10^{-5}$ after electron cooling.

In an electron cooler the electrons are accelerated first to the full energy and from there on they drift in a longitudinal magnetic field (solenoids and toroids) to the collector. A CAD model and a cross section of the cooler are shown in Fig. 2.9. Before being dissipated there, they are decelerated to kinetic energies below a few keV. Secondary electrons liberate from the collector surface and primary electrons which pick up a high transverse energy are re-accelerated into the system. Due to the longitudinal magnetic field the transverse motion is transformed into cyclotron spirals around the field lines. Electrons leaving the collector can bounce back and forth between gun and collector entrance with a spiral radius continuously increasing because of residual gas collisions. Eventually they hit a grounded surface at nearly full electron beam energy.

For target operation of an electron cooler, the energy of the electrons is slightly detuned and varied from the cooling condition for some time (for dielectronic recombination experiments). One of the key features in CRYRING@ESR is the electron cooler with adiabatic transverse expansion of the electron beam [55]. This yields

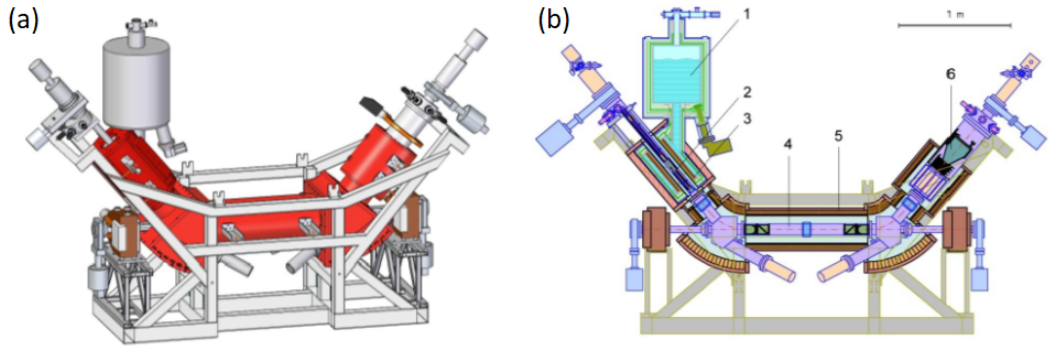

Figure 2.9: (a) CAD model and (b) cross section of the CRYRING electron cooler [47] with 1) liquid-helium reservoir, 2) electron gun, 3) superconducting gun solenoid, 4) vacuum chamber, 5) normal-conducting magnets, 6) electron collector.

about 100 times lower transverse electron temperature than in the ESR and achieves ultracold electron beams [56] with $\sim$ 1 meV transverse and $\sim$ 100 μeV longitudinal electron beam temperatures. These are very favorable conditions for recombination experiments allowing for high resolution studies in recombination spectroscopy with merged ion-electron beams (dielectronic recombination resonances).

2.4 X-ray detectors

For the detection of x-rays it is important to choose suitable detectors. As already mentioned, the exact geometry of the electron cooler devices only allows for x-ray detection under the two observation angles of 0° and 180°. The photon energy to be detected ranges from a few keV to over 100 keV. For this energy range, semiconductor detectors made of high-purity germanium (HPGe) had been chosen for our first experiment at CRYRING@ESR as discussed in Chapter 5. Afterwards, in Chapter 6, metallic magnetic calorimeters were used to pursue high energy resolution for x-ray spectroscopy studies, while maintaining broad spectral range and high photon-flux tolerance.

2.4.1 Germanium detector

Germanium is a frequently used material in photon detection technology. Due to the low average energy of 2.96 eV required for the generation of an electron-hole pair and the resulting high number of generated charge carriers per energy of a photon, a comparable energy resolution than that of a silicon detector is expected. To ensure the detected number of electron-hole pairs is proportional to the photon energy, the detector must be cooled. For this purpose, the detector is connected to a cryostat, which uses nitrogen to cool the crystal to a constant temperature. To prevent condensed water from settling on the cooled detector, the crystal is located

in a vacuum which is delimited by a thin beryllium window.

Germanium has a relatively high atomic number of $Z = 32$ for crystals used in detectors in particular compared to silicon ($Z = 14$) . The larger the atomic number Z, the higher the absorption capacity over a wide energy range. This becomes clear when considering the absorption coefficient, which shows a strong dependence on the atomic number, namely $\tau \propto Z^4$, which results from the photoabsorption. Because of this dependence, beryllium windows are adopted in many detectors, since the atomic number is very small ($Z = 4$) and thus the absorption capacity is very low and most of the photons are transmitted. However, it must be taken into account that for semiconductor detectors, the efficiency drops significantly above a certain energy, the reason is the so-called absorption edges [57]. Here, the absorption of photons in an atom increases abruptly at the binding energy of a shell. The largest change occurs at the K-shell energy. For germanium this edge is roughly at 11 keV, i.e., at this energy the efficiency of the detector decreases and increases again to the maximum value with increasing energy. Figure 2.10 shows the absorption edge for germanium in the efficiency spectrum for different crystal thicknesses and thicknesses of the beryllium window. Due to the absorption edge in the x-ray spectra it has to be taken into account that the intensity in the energy range above 11 keV does not correspond to the actual one.

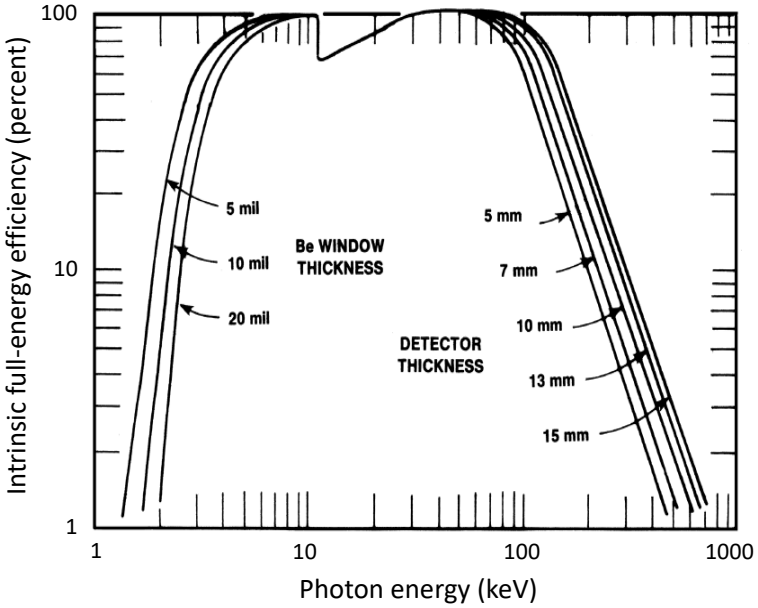

Figure 2.10: Detector efficiency of a germanium detector plotted against photon energy [57]. The left half of the figure shows the influence of the thickness of beryllium window and the right half of the figure shows the influence of the thickness of crystal.

The detectors used in my experiment are two different sized HPGe detectors. The germanium detector at 0° (GLP-16195/10P) has a crystal diameter of 16 mm and a thickness of 10 mm, at 180° the germanium detector (GEM-S5020P4-B) used

has a crystal diameter of 49.7 mm and a thickness of 21 mm. For background suppression a collimator with a diameter of 13 mm at 0 ° and of 35 mm at 180° was mounted in front of each detector. Furthermore, there is a difference in geometry, whereby the smaller one has a planar geometry and the larger one has a coaxial geometry. An example of a planar HPGe detector and a coaxial HPGe detector using a p-type crystal is shown in Fig. 2.11. In planar configuration, the electric contacts are provided on the two flat surfaces of a germanium crystal. In coaxial configuration, one electrode is fabricated at the outer surface of a cylindrical crystal and the other electrode is located at the inner surface of the central hole. In this way, much larger active volumes can be achieved.

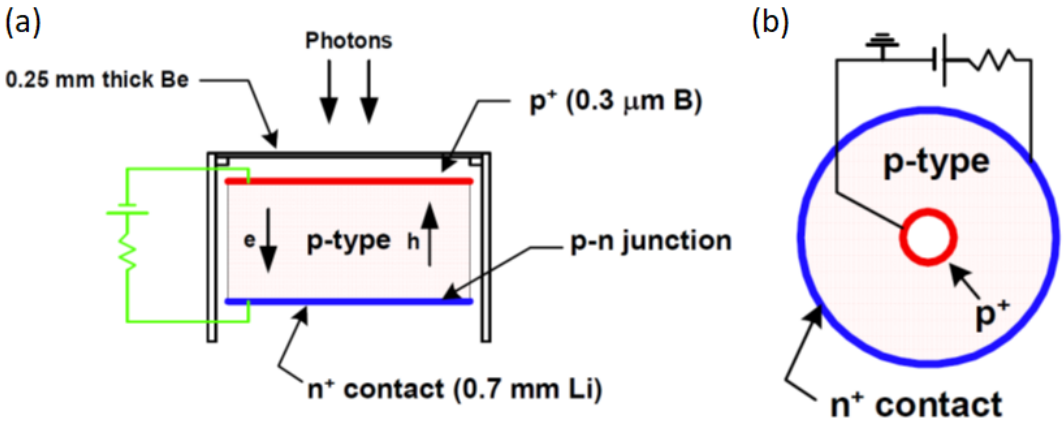

Figure 2.11: Electrode configurations for (a) a planar detector and (b) a coaxial detector using p-type crystals [58].

2.4.2 Magnetic microcalorimeter

Metallic magnetic calorimeters (MMC) are calorimetric particle detectors operated at temperatures below 100 mK, and usually consist of a massive particle absorber with a certain heat capacity C that is suited for the particles to be detected and that is in tight thermal contact to a paramagnetic temperature sensor. The latter is placed in a week magnetic field to create a temperature dependent sensor magnetization, the sensor is weakly coupled to a thermal bath kept at constant temperature to allow the detector to take a well-defined state in the absence of an energy input. A sketch of the detection principle of a microcalorimeter is displayed in Fig. 2.12.

If a particle or photon deposits its kinetic energy E in the absorber, it excites phonons or excitons which decay into phonons after a certain recombination time. After a thermalization time, thermal equilibrium in the absorber is established and the temperature has changed by an amount $\Delta T = E/C$. The absorber is coupled to a thermometer which monitors this temperature rise. The thermal energy is then transferred to a heat sink via a defined thermal link with a thermal conductance G.

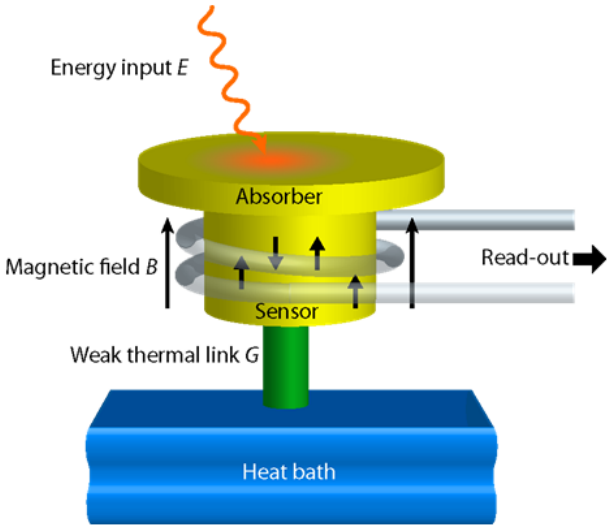

Figure 2.12: Schematic drawing of a metallic magnetic calorimeter [59]. It consists of an x-ray absorber and a paramagnetic sensor, which is placed in a weak external magnetic field. The absorption of a particle increases the temperature and thus decrease the magnetization of the sensor, the changes of the temperature is read out by a low-noise high-bandwidth SQUID magnetometer.

After cooling down again to the operating temperature, the absorber can detect the next photon. Microcalorimeters are, therefore, single-photon detectors [59]

According to the calorimetric detection principle [60], a temperature rise of the detector upon the deposition of energy in the absorber leads to a change of sensor magnetization. The latter can be precisely measured as a change of magnetic flux using a superconducting quantum interference device (SQUID) as shown in Fig. 2.13. The depicted detector layout makes use of two single pixels that are read out in parallel. This gradiometric setup minimizes the effect of temperature fluctuations of the heat bath and allows the preparation of a superconducting persistent current in the pick-up coil that generates the magnetic field that is required for the temperature sensor. More remarkably, the well-fabricated metallic magnetic calorimeters developed by KIP, Heidelberg University [61, 62] combine high energy resolution, fast detector rise times ($\tau_0 < 100\ ns$), high quantum efficiency and large dynamic range, turning them into promising tools for numerous precision experiments in atomic and nuclear physics at GSI/FAIR [24, 63, 64].

Gold is used as an absorber material due to its high stopping power for photons. A thickness of 5 μm provides a stopping power close to 100% for photons of energies up to 6 keV and 45% at 20 keV calculated with Monte Carlo simulation using the software PENELOPE [66]. The first detector, maXs-20, consists of a linear array of eight pixels with an absorber size of $250 \times 250\ \mu m^2$ and a gap of 5 μm in between pixels [62]. In experiments with ^{55}Fe and ^{241}Am calibration sources measured by maXs-20 detector, an energy resolution below 3 eV had been demonstrated for the detection of x-rays with energies up to 20 keV [67]. The absorbers of the second

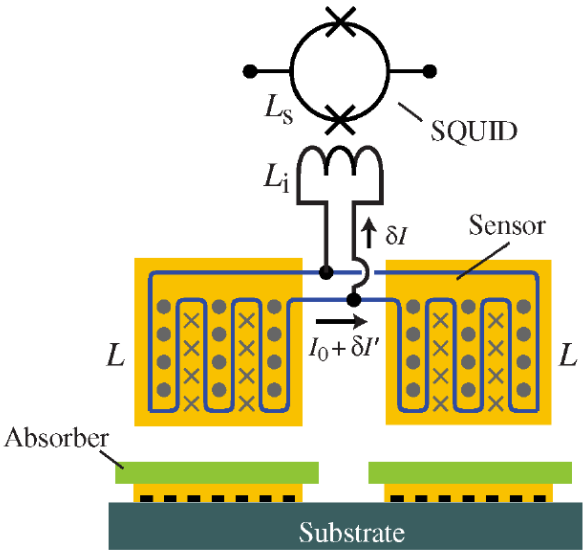

Figure 2.13: Schematic drawing of a gradiometric detector consisting of two single metallic magnetic calorimeters [65]. A persistent current I_0 circulates in the superconducting meander-shaped pickup coil polarizing the magnetic moment in the sensor. As the magnetic flux in a superconducting loop is conserved, a change of flux driven by a temperature-induced change of magnetization induces an additional screening current (δI), which is read out as a voltage drop over the dc-SQUID.

device, maXs-200 detector, are designed to be made of 200 μm thick gold, it provides sufficient stopping power for x-ray photons up to 200 keV with an absorption efficiency above 75% for energies around 100 keV [24, 64] and an energy resolution of $\Delta E_{\mathrm{FWHM}} = 46$ eV at 60 keV [68]. The maXs-200 detector is very well suited for spectroscopic studies of the Lamb Shift in hydrogen-like U^{91+}, i.e. the $2p_{3/2} \rightarrow 1s_{1/2}$ Lyα_1 transition energy is around 102 keV. For a metallic magnetic calorimeter the energy resolution should be almost independent of the absorbed energy. By increasing the temperature stability of the cryostat, an intrinsic energy resolution of $\Delta E_{\mathrm{FWHM}} = 27$ eV at 0 keV could be achieved [63].

The first two-dimensional detector array maXs-30 consisting of 64 pixels with a total active detection area of 16 mm^2 were developed for x-ray energies up to 30 keV [69]. In a configuration with a 30 μm thick absorber made of gold it has an absorption efficiency above 80% for x-rays with energies up to 30 keV. A quantum efficiency above 30% is achieved for x-ray energies up to 50 keV as well as between 80 keV and 90 keV [70]. For our interested Lyα-transition of hydrogen-like U^{91+} with an energy of around 100 keV, it only has an absorption efficiency of about 25%.

In recent beam time at the CRYRING@ESR in the spring time of 2021, a new generation maXs-100 detector towards two-dimensional arrays and towards larger pixel counts was developed for state resolved x-ray spectroscopy precision study via radiative recombination with H-like uranium at the electron cooler. The maXs-100 detector aims especially for an increased detection area of 1 cm^2 while at the same

time keeping the good energy resolution of metallic magnetic calorimeters. It is equipped with 8×8 array of 50 μm thick gold absorbers, hence has an absorption efficiency of 49% for x-ray photons at around 90 keV, a quantum efficiency of 40% and 34% for x-ray energies at 100 keV and 110 keV, respectively. This type of maXs-100 detector chip together with the first stage readout electronics is integrated into a detector head, as shown in Fig. 2.14. More remarkably, the large energy bandwidth comparable to semiconductor detectors enables simultaneous measurements of "Balmer"-transitions occurring at energies 15 - 25 keV in the emitter frame, whereby the QED corrections on these lines are negligibly small and therefore allows for in-situ Doppler correction in beam-time experiments. At the same time the high energy resolution maXs-100 detector may also entitle us for the first time to resolve the doublet splitting of the Kα_1 and the Kα_2 lines in He-like uranium spectrum, which, beam time at the ESR electron cooler in August 2001 [71], was impeded by the energy resolution of intrinsic Ge(i) detectors of about 700 eV at 100 keV.

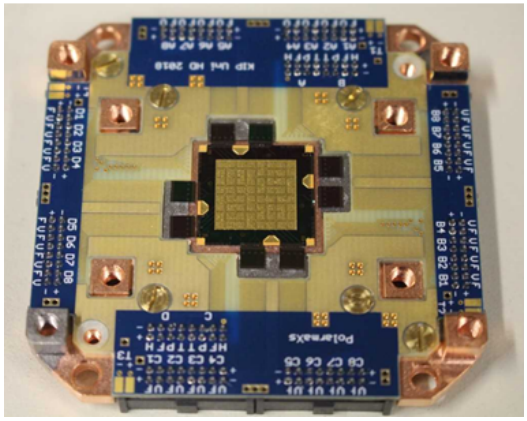

Figure 2.14: Physical map of one of the detector heads used in the present experiment [21]. In the center the 8×8 pixels of maXs-100 chip are visible. They are surround by 8 chips containing the 32 first stage readout SQUIDs.

Chapter 3

Structure of few-electron systems at high-Z

To date, our knowledge about the atomic structure of the hydrogen and helium atom is extremely precise and the expansion of research along the one- and two-electron isoelectronic sequences up to the heaviest ions is a central subject of the present research in atomic and fundamental physics. Highly charged ions of heavy elements represent a crucial field of atomic structure that offers numerous challenges from theoretical and practical viewpoints, since for such atomic systems the light matter coupling constant $v/c \sim \alpha Z$ (α is the fine-structure constant) is close to one. At high-Z we are dealing therefore with the regime of strong coupling, their basic atomic characteristics, such as energy levels, transition probabilities, are substantially influenced by relativistic effects or even by quantum electrodynamics (QED) in the extremely strong field regime, which often bring about new spectral patterns that are remarkably different from the spectra of light elements.

3.1 One-electron systems

Since the early days of quantum mechanics the simple level scheme of atomic hydrogen has provided a stringent testing ground for atomic structure theory. For hydrogen, Lamb and Rotherfold in 1947, using microwave techniques, discovered that the binding energy of the $2s_{1/2}$ state is shifted towards smaller value relative to the $2p_{1/2}$ state [72], named as Lamb shift at that time, which cannot be explained within the relativistic corrected formulation of quantum mechanics, the so-called Dirac theory. This leads to the development of modern quantum electrodynamics (QED) that explains the very tiny level spacing between the $2s_{1/2}$ and $2p_{1/2}$ states, amounting to 4.4×10^{-6} eV, by the interaction of the electron with its own radiation field. In atomic theory of spectra for neutral and weakly ionized atoms, relativistic effects are considered as small corrections in contrast to the case of highly

charged heavy ions for which relativistic and QED effects strongly depends on the ion charge [10], for example, the level splitting between $2s_{1/2}$ state and $2p_{1/2}$ state in H-like U^{91+} is roughly 75.29 eV, which is seven orders of magnitude larger than that of hydrogen.

3.1.1 Nonrelativistic theory

Hydrogenic atoms consist of a single electronic charge orbiting a positively charged nucleus. It was demonstrated by Rutherford in 1911 that the nucleus is orders of magnitude smaller than the size of the atom. After this discovery the atom was visualized as a miniature planetary system in which the nucleus could be approximated by a point charge. The conceptual step to the modern atom was made by Bohr in 1913. By quantization of the planetary motion, Bohr formulated the famous Bohr model for the atom which explained the optical spectrum of atomic hydrogen and defined the principle structure of the atom.

The Bohr atom with the method was developed by Schrödinger in 1926, where the Coulomb interaction between electron and nucleus give rise to a central potential. Hence, the Hamiltonian operator to calculate the energy eigenvalues in the absence of externally applied fields is of the general form $\mathcal{H}_0 = -\frac{\hbar^2}{2m_r}\Delta + \mathcal{V}(r)$ and will be referred as the Schrödinger Hamiltonian for the atom,

$$\mathcal{H}_0 = \frac{\mathbf{P^2}}{2m_r} + \mathcal{V}(r) = -\frac{\hbar^2}{2m_r}\Delta - \frac{Ze^2}{4\pi\varepsilon_0 r}. \tag{3.1}$$

Here r is the electron-nuclear radial distance and m_r the reduced mass,

$$m_r = m_e/(1 + m_e/M), \tag{3.2}$$

with $m_e \simeq 9.1 \times 10^{-31}$Kg the electronic and and M the nuclear rest mass.

In terms of the principal quantum number the quantization condition takes the famous form of the Bohr formula, one obtains for the energy eigenvalues

$$E_n = -\alpha^2 m_r c^2 \frac{Z^2}{2n^2} = -\frac{Z^2}{n^2}\mathrm{Ry}. \tag{3.3}$$

with Rydberg atomic unit is used, 1Ry $\simeq 13.6\ eV$, and the fine structure constant $\alpha \simeq 1/137$. Writing $E_n \simeq \frac{1}{2}m_e\langle v^2\rangle$ we infer that $\alpha^2 Z^2 \simeq \langle (v/c)^2\rangle$. States with a large principle quantum number are called Rydberg states and atoms excited to thoses states are called Rydberg atoms. Eq. 3.3 defines the complete spectrum of the hydrogen atom according to the Schrödinger theory, it shows degeneracy of the energy levels, which means that different states have the same energy, e.g., states of given n but differing in l.

The atomic energy levels are illustrated in Fig. 3.1 along with the name of some

well-known atomic transitions between hydrogenic levels [73]: Lyman-α (Lα) and Balmer-α (Hα). In the case of optically induced transitions the change in state of atom is accompanied by a simultaneous change of light field, this happens through the exchange of a photon between the atom and the field in such a way that the total energy and momentum are conserved. The first series of this type was discovered empirically by Balmer in 1885 [74] for the spectral lines of hydrogen in the visible part of the spectrum. The Balmer series is defined by all optical excitation decay to $n = 2$ level. Analogously, the Lyman series involves the transitions to the ground state. In 1888 Rydberg generalized the expression for the Balmer series into the Rydberg formula, which yields the wavelength of any transition (in vacuum) between two hydrogenic energy levels,

$$\frac{1}{\lambda_n} = -R_M \left[\left(\frac{1}{n}\right)^2 - \left(\frac{1}{n_0}\right)^2 \right], \tag{3.4}$$

with $R_M = R_\infty/(1 + m_e/M)$ and $R_\infty = \alpha^2 m_e c/2h$ being the finite-mass/infinite-mass Rydberg constants, respectively, and $n > n_0$, with n_0 being the principal quantum number of the common and lowest level in all transitions considered, i.e., the defining level of the series. The corresponding energy splitting is given by

$$\Delta E_n = E_n - E_0 = \frac{hc}{\lambda_n} = \frac{m_e c^2 \alpha^2}{2\,(1 + m_e/M)} \left(\frac{1}{n^2} - \frac{1}{n_0^2}\right). \tag{3.5}$$

The typical energy level separation turns out to be a factor α^2 smaller than the electron rest mass energy, which justifies the nonrelativistic Ansatz.

3.1.2 Relativistic theory

The energy structure of hydrogen(-like) system calculated by Bohr's model from non-relativistic Hamiltonian agrees well with the experimental measurements. However, in high resolution experiments, small deviations were observed as energy shifts and splitting of spectral lines. These divergences, so-called fine structure, were not predicted by non-relativistic theory, which suggests there are weak additional effects that do not strongly affect the position of the spectral lines but remove the energy degeneracy of the orbital quantum number l. Revealing the origin of fine structure was one of the great puzzles of modern physics. A rigorous relativistic description was possible only after Dirac in 1928 [75] formulated his famous relativistic quantum theory for the electron, in this theory the appearance of spin and the associated magnetic moment were identified as intrinsic relativistic phenomena.

The wave equation that simultaneously satisfies the requirements of quantum mechanics and special relativity is the Dirac equation. In free space including electromagnetic interactions it describes all massive particles of semi-integer spin with

parity as a symmetry, such as electrons and quarks. It was the first theory to fully explain special relativity in the context of quantum mechanics. The Dirac equation pictures the fine structure of the hydrogen(-like) spectrum in a completely meticulous manner. The equation also justifies a posteriority the introduction of spinors, that is, of the vector wavefunctions introduced by Pauli in a heuristic way. Due to the relativistic effects, the Dirac equation adopts the form of a Schrödinger equation but with the modified Hamiltonian [76],

$$\mathcal{H} = -i\hbar c\boldsymbol{\alpha}\cdot\nabla + \mathcal{V}(r) + m_e c^2\gamma^0, \tag{3.6}$$

where $\mathcal{V}(r)$ is the Coulomb potential of the nucleus, $\boldsymbol{\alpha}$ denotes the vector formed from the usual four-by-four Dirac matrices, γ^0 is the fourth Dirac matrix, often denoted by β.

For the point-like nucleus, analytical solution of Dirac equation yields the well known formula for the energy of a bound state, written as

$$\begin{aligned} E_{n,j} &= \frac{m_e c^2}{\sqrt{1+\frac{(\alpha Z)^2}{[n-(j+1/2)+\sqrt{(j+1/2)^2-(\alpha Z)^2}]^2}}} \\ &= m_e c^2\left[1-\frac{1}{2}\frac{(\alpha Z)^2}{n^2}-\frac{1}{2}\frac{(\alpha Z)^4}{n^3}\left(\frac{1}{j+1/2}-\frac{3}{4n}\right)-\cdots\right], \end{aligned} \tag{3.7}$$

where the second term represents the nonrelativistic binding energy in a hydrogenic atom depicted in Eq. 3.3. The third term brings us a single expression for the fine-structure shift which depends on only two quantum numbers (n, j),

$$\Delta E_{n,j} = -E_n\frac{Z^2\alpha^2}{n^2}\left(\frac{3}{4}-\frac{n}{j+1/2}\right). \tag{3.8}$$

For $j = 1/2$ this expression corresponds to the $l = 0$ relativistic shift of Eq. 3.3 whereas for $j = l \pm \frac{1}{2}$ it gives the fine-structure splitting for $l > 0$. One may note that, taking into account all relativistic corrections (but without the Lamb shift), there still exists a partial degeneracy of the quantum number j. For example, the value $j = \frac{1}{2}$ is obtained for $l = 0$ but also for $l = 1$ using $j = l - \frac{1}{2}$, this results in an accidental degeneracy of the $^2P_{1/2}$ and $^2S_{1/2}$ levels in hydrogen(-like) atoms. As an example for hydrogen(-like) systems [77], the diagram of fine-structure effects at $n = 2$ level is depicted in Fig. 3.1.

Only remains to discuss is the Lamb shift [72], which can be calculated by taking two extensions of Dirac equation into account. The first extension consists of quantum electrodynamical (QED) corrections, where the interaction of the electron with the quantum vacuum is treated. The second extension takes several effects of the nucleus, e.g. the finite size and the relativistic recoil, into account.

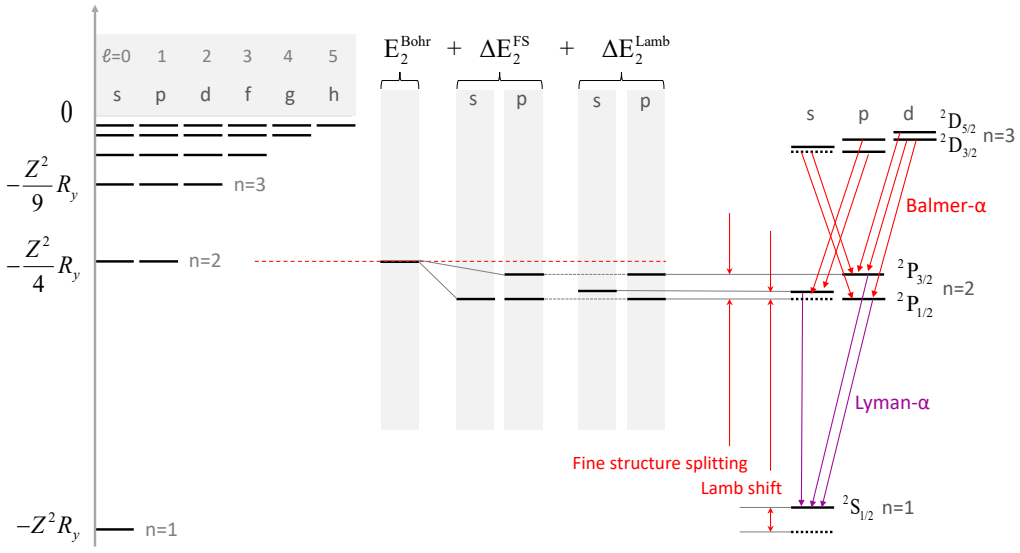

Figure 3.1: Fine-structure effects in hydrogen(-like) systems. From left to right are shown the Bohr level at $E_2^{Bohr} = -\frac{Z^2}{4}R_y$, the fine-structure shift $\Delta_{2,j}^{FS}$ for $j = l \pm \frac{1}{2}$ and the Lamb shift. The latter cannot be understood by classical field but requires quantum electrodynamics (QED). On the far right side the Balmer and Lyman transitions are show with a schematic presentation of single photon electric-dipole emission.

3.1.3 QED effects and the Lamb shift

One may imagine the Coulomb force between charged particles is mediated by a continuous exchange of virtual photons, but each isolated charge also continuously emits and reabsorbs virtual photons, with the result that the position of the electron is smeared over a region of 0.1 fm, this reduces the overlap between the electronic orbits and the nucleus. Hence, the Lamb shift causes corrections that are stronger for small n and small l, the splitting between the $2s_{1/2}$ and $2p_{1/2}$ states occurs because the radiative shifts are much smaller for p state than for s state. Although the term Lamb shift was originally used only for the $2s_{1/2} - 2p_{1/2}$ energy splitting in hydrogen, it is now commonly used for the shift of isolated levels in atoms and ions, e.g. the Lamb shift of the $1s_{1/2}$, $2s_{1/2}$ ... levels. The Lamb shift is defined as the difference between real binding energy and the Dirac-Coulomb energy calculated for a point-like necleus, disregarding all QED effects, for one electron systems (see Fig. 3.1), the Lamb shift is commonly expressed by [78, 79]

$$\Delta E_{lamb} = \frac{\alpha}{\pi}\frac{(Z\alpha)^4}{n^3}F(Z\alpha)\,m_e c^2 \qquad F(Z\alpha) = F_{SE} + F_{VP} + F_{FS} \tag{3.9}$$

where $F(Z\alpha)$ is a dimensionless, slowly varying function comprising all the QED corrections and includes in addition the shift in binding energy caused by the finite size of nucleus. As the Lamb shift scales approximately with Z^4/n^3, these corrections are largest for the ground state and for the strong field of high-Z ions. The leading

QED corrections contributing to the Lamb shift arise from the self energy F_{SE} and vacuum polarization F_{VP} of the electron bound in the external field of the nucleus, both corrections are of the order of $Z^4\alpha^5 m_e c^2$. In QED theory, the different interactions between the electrons, ions and photons are represented by the Feynman diagrams depicted in Fig. 3.2.

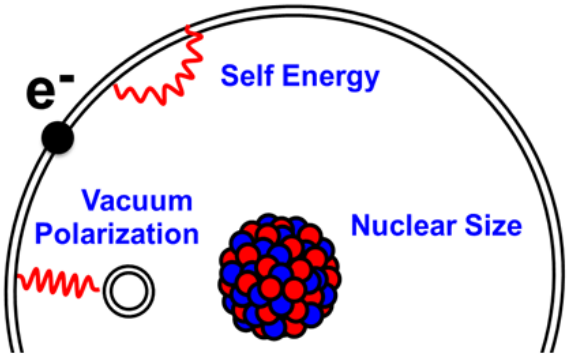

Figure 3.2: Feynman diagrams for the one-electron Lamb shift: self energy (SE); vacuum polarization (VP); and finite nuclear size (FS).

At low-Z the self energy, originating from the emission and re-absorption of a virtual photon, dominates the most important Lamb shift correction. With increasing nuclear charge, however, the influence of the vacuum polarization, describing the virtual creation and annihilation of an electron-positron pair due to the Coulomb interaction of the electron and the nucleus, increases continuously. In Fig. 3.3 the contribution of the self energy (SE), vacuum polarization (VP), and the finite nuclear size (FS) to the Lamb shift in hydrogen-like atoms are given separately as a function of the nuclear charge. For light one-electron systems such as atomic hydrogen, the ground-state Lamb shift had been measured with extraordinary relative accuracy of 3.2×10^{-6}, in agreement with QED calculations, using Doppler-free, two photon laser spectroscopy [80, 81]. Laser-spectroscopic methods cannot be applied in the measurement for the highly charged heavy ions, because the energies of transitions into the ground-state lie in the x-ray region.

For low-Z systems, the experiments are sensitive to the lower orders of the function $F(Z\alpha)$, which can be treated by an $Z\alpha$ expansion method. However, for a test of the higher order terms, which are not accessible using low-Z ions, the heaviest species such as H-like uranium are required. At high-Z the influence of the higher order contributions becomes so crucial that the radiative corrections can no longer be treated by the $Z\alpha$ expansion method but must be calculated to all orders of $Z\alpha$ [85, 86, 87, 88, 89], resulting in nonperturbative calculations (without expansion in $Z\alpha$, in contrast to the methods applied for the low-Z ions) for high-Z hydrogen-like ions which do now comprise all second-order (in α) corrections [90, 91]. The latter is of three kinds, second-order vacuum polarization (VPVP), second-order self energy (SESE), and combined vacuum-polarization-self-energy (SEVP). The effects

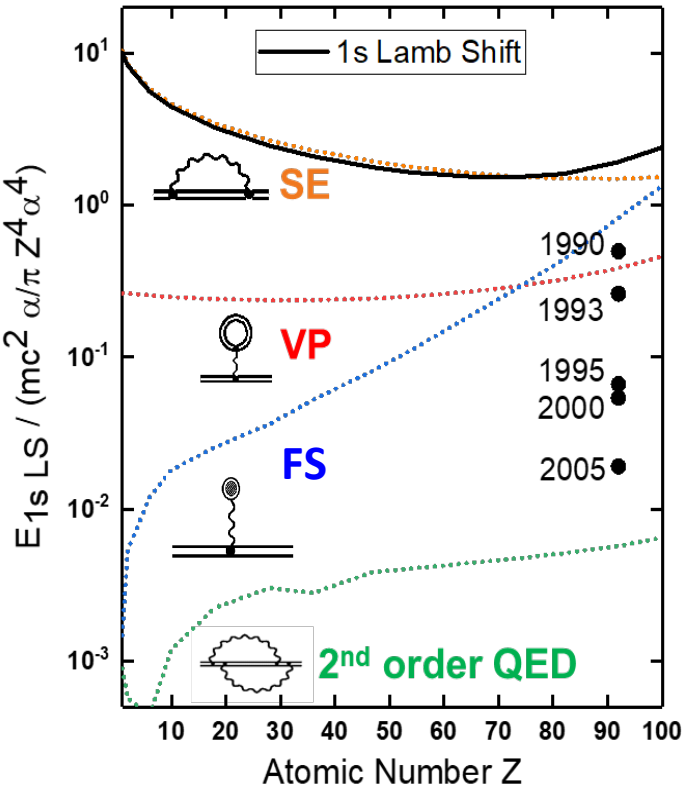

Figure 3.3: Various individual contribution to the ground state Lamb shift in hydrogen-like ions as a function of the nuclear charge, according to Ref. [79], together with the experimental accuracy achieved so far in H-like uranium [22, 23, 82, 83, 84].

of second-order vacuum polarization and the combined vacuum-polarization-self-energy, which are of the order of 1 eV, had been firstly calculated by Soff *et al.*[92, 93], Persson *et al.*[94, 95], and Lindgren *et al.* [96] in 20th century. The second-order self-energy diagrams, on the other hand, which can be expected to be at least of the same order, has been completed recently by Yerokhin *et al.* [97].

All in all, Table 3.1 shows the contributions for the $1s$ and $2s$ states in H-like uranium relative to electron rest energy. It can be seen that the main radiative contributions arise from the self energy (SE) and vacuum polarization (VP) corrections, while the main non-QED correction is due to the finite nuclear size (FS) effect. The sophisticated QED theory predicts a value of 463.57 ± 0.53 eV [98] for the $1s$ Lamb shift, while the experiment accuracy achieved ao far is 460.2 ± 4.6 eV [22], whereby the conventional germanium detector had already utilize all the strength, the experimental accuracy is still about one orders of magnitude lower than the theoretical one. Therefore, to probe QED corrections which are beyond the one photon exchange diagrams, the next generation experiments, dedicated to high resolution x-ray spectrometer (mianly two kinds: the crystal spectrometer FOCAL [99, 100] and the microcalorimeter maXs [24, 63]), devoted to the ground state Lamb shift in high-Z H-like systems are ongoing at GSI in Germany to reach the level of about 1

eV.

Table 3.1: Theoretical contributions (in eV) to the $1s$ and $2s$ level energies, and the Lamb shift in H-like uranium. Experiment: Gumberidze *et al.*, *Phys. Rev. Lett.* **94** 223001 (2005). Theory: Yerokhin and Shabaev, *J. Phys. Chem. Ref. Data.* **44** 3 (2015).

Contribution	$1s$	$2s$
Dirac energy (point-like necleus)	-132279.93	-34215.48
First-order QED		
Self energy	355.06	65.39
Vacuum polarization	-88.61	-15.64
Second-order QED		
VPVP	-0.94	-0.16
SESE	-1.57	-0.29
SEVP	1.13	0.21
Nuclear Contribution		
Finite nuclear size	198.51	37.70
Nuclear recoil	0.51	0.13
Nuclear polarization	-0.20	-0.03
Theoretical Lamb shift [98]	463.57(0.53)	87.25
Experimental Lamb shift [22]	460.2(4.6)	–

3.2 Two-electron systems

For few-electron ions, besides the one-electron radiative corrections, one has to take into account the interelectronic-interaction corrections. These corrections are suppressed by the parameter $1/Z$. For high-Z ions this parameter becomes comparable with the fine structure constant α, which characterizes the radiative corrections. In contrast to neutral atoms with a nuclear charge number $Z \leq 20$ and low-charged ions in low states of excitation, LS coupling scheme is not adequate when the electrostatic interaction V_{es} is much smaller than the spin-orbit one V_{so}: $V_{es} \ll V_{so}$, and the jj coupling is realized for multi-charged heavy ions as the electrostatic interaction increases approximately with Z while the spin-orbit one increase as Z^4. A smooth transformation from the LS to the jj coupling is shown in Fig. 3.4 when the nuclear charge Z increases from $Z = 12$ to $Z = 100$. The example is for the $1s2p$ states of He-like ions and the numerical results from Artemyev *et al.* [101] were taken to generate the plot. As can be seen, for low-Z ions, very small energy splitting of the $^3P_{0,1,2}$ terms is observed whereas at high nuclear charges, the levels are grouped according to their total angular momentum J. It is worth mention that experimentally an unambiguous identification of He-like uranium intra-shell transition $1s_{1/2}2p_{3/2}\ ^3P_2 \rightarrow 1s_{1/2}2s_{1/2}\ ^3S_1$ emitted from the internal gas-jet target of the ESR storage ring [102, 103], adopting the crystal spectrometer FOCAL with a much

higher accuracy for the spectral line position, is possible.

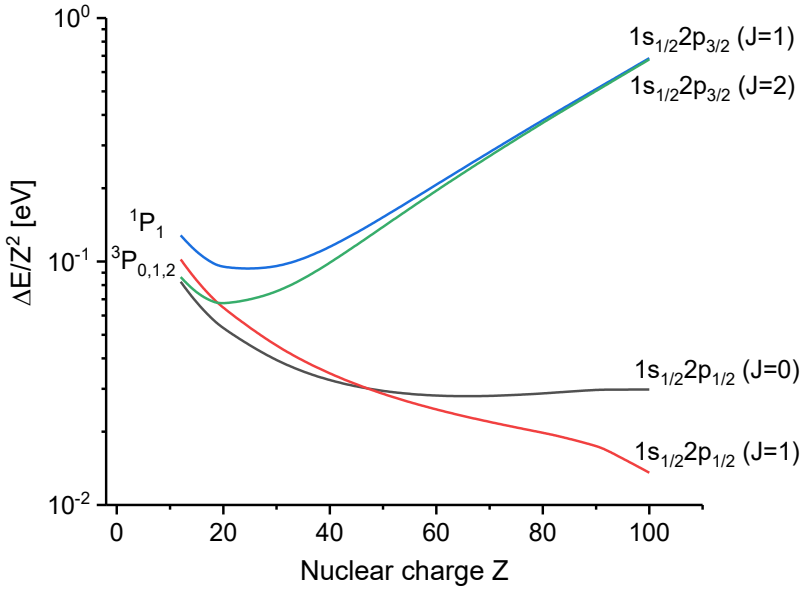

Figure 3.4: Electronic binding energies of the $1s2p$ states in He-like ions as a function of the nuclear charge Z. Plotted are the energy differences to the $1s2s\ ^3S_1$ state divided by the square of nuclear charge. Data are from Ref. [101]

The two-electron ions are of particular interest as they present the simplest multi-electron system. Investigations of these ions along the isoelectronic sequence [104, 105] probe uniquely our understanding of correlation, relativistic, and QED effects. However, the situation of the QED theory of high-Z two-electron ions is more complicated as compared to the one-electron system because of the necessity to include corrections caused by electron-electron interactions. Despite these difficulties, substantial progress in the theory of two-electron systems has been achieved and the theoretical accuracy [106, 107, 108, 109, 110] is now approaching that of one-electron systems.

The energy of a He-like system can be presented as the sum of two independent one-electron contributions and a two-electron contribution. The latter includes effects from the electron-electron interaction such as one- and two-photon exchange diagrams, self-energy and vacuum-polarization screening diagrams, and higher order corrections. A complete QED calculation of the two-electron contribution to second-order had been performed by Yerokhin *et al.* [111] in 20th century, and late by Artemyev *et al.* [101]. Now it is also possible to collect all contributions available to the ionization energies of $n = 1$ and $n = 2$ states of He-like uranium. In Table 3.2 ΔE_{Dirac} is the Dirac value for the ionization energy of the valence electron including the finite-nuclear-size effect, the electron-electron interaction ΔE_{int} comprise the one-, two-, three-, and more photon exchange, ΔE_{1el}^{QED} is the sum of the one- and two-loop one-electron QED corrections, ΔE_{2el}^{QED} and ΔE_{ho}^{QED} are the two-electron QED correction and higher-order QED correction, respectively, the relativistic recoil

correction ΔE_{rel} consists of the one-electron and the two-electron part.

Table 3.2: Theoretical contributions to the $n = 1$ and $n = 2$ ground-state energies of He-like uranium [101], in eV.

Z	State	ΔE_{Dirac}	ΔE_{in}	ΔE_{1el}^{QED}	ΔE_{2el}^{QED}	ΔE_{ho}^{QED}	ΔE_{rel}	Total
92	$(1s)^2$	-132081.59(52)	2253.940(15)	265.16(33)	-8.0020(20)	-0.05(18)	0.4600	-129570.30(64)
	$(1s2s)_0$	-34177.81(10)	843.6097(49)	49.44(22)	-3.8259(4)	-0.009(51)	0.1260	-33288.51(24)
	$(1s2s)_1$	-34177.81(10)	586.3566(21)	49.44(22)	-1.2301(3)	0.0030(16)	0.1266	-33543.15(24)
	$(1s2p_{1/2})_0$	-34211.077(12)	917.4978(17)	6.86(10)	-4.4740(3)	0.002(73)	0.0531	-33291.14(13)
	$(1s2p_{1/2})_1$	-34211.077(12)	805.1940(11)	6.86(10)	-1.6798(2)	0.001(17)	0.0743	-33400.63(11)
	$(1s2p_{3/2})_1$	-29649.8353(26)	682.1945	8.80(10)	-0.6677(5)	-0.003(11)	0.0774	-28959.44(10)
	$(1s2p_{3/2})_2$	-29649.8353(26)	608.3559(4)	8.80(10)	-0.4725(5)	0.0068	0.0324	-29033.12(10)

Experimentally, a novel method was first exploited by Marrs *et al.* [112] at the SuperEBIT at the Lawrence Livermore National Laboratory which exploits radiative recombination (RR) transitions from the continuum into the vacant K-shell of some bare and H-like ions, has allowed one to carry out direct measurement of the two-electron contributions to the ground state binding energies of He-like ions with nuclear charge $32 \leq Z \leq 83$. In particular, the binding energies of H-like and He-like ions of the same element have been compared, which makes all one-electron contributions to the binding energy such as finite-nuclear size corrections and the one-electron self-energy cancel out completely, and to extract the pure two-electron contribution. In Table 3.3 various components of the two-electron contribution to the ground-state energy of He-like ions are compared with experimental results. However, due to the limitation of SuperEBIT that at high nuclear charges such as $Z = 83$ it turned out that the production efficiency for bare ions is not sufficient, as the rapid decrease of the K-shell ionization cross section for electron impact which scales as $1/Z^4$, the results suffered counting statistics. The experimental accuracy for the time being, with a statistical accuracy of 14 eV achieved compared with the predicted two-electron self-energy contributions of 6.73 eV at $Z = 83$, was not sufficient for testing the QED effects. Afterwards, Gumberidze *et al.* [113] extended the measurement of the two-electron contribution to the ground state binding energy to the heaviest stable element in He-like uranium at the storage ring ESR, whereby the statistical accuracy of 9 eV already reaches the size of the calculated specific two-electron self-energy correction [101, 111], i.e., of an α^2 radiative correction.

Table 3.3: Two-electron contribution to the ground-state energy of He-like ions Comparison between theory and experiment (in eV)

Z	1-photon exchange	2-photon exchange non-QED	2-photon exchange QED	Self -energy	Vacuum polarization	$\geq$ 3-photon non-QED	$\geq$ 3-photon QED	Total contribution [111]	Experimental results [112][113]
32	567.61	-5.23	0.04	-0.47	0.04	0.03	±0.01	562.02(1)	562.5(1.6)
54	1036.56	-6.98	0.10	-1.82	0.26	0.04	±0.03	1028.16(3)	1027.2(3.5)
66	1347.45(1)	-8.30	0.06	-3.22	0.56	0.05	±0.04	1336.58(4)	1341.6(4.3)
74	1586.93(2)	-9.33	-0.04(1)	-4.59	0.91	0.05	±0.05	1573.92(6)	1568(15)
83	1897.56(1)	-10.64	-0.30(1)	-6.73	1.55	0.06	±0.07	1881.50(7)	1876(14)
92	2265.88(1)	-12.09	-0.79	-9.78	2.63	0.06	±0.09	2245.92(9)	2248(9)

3.3 Transition probabilities

Radiative transition probabilities per time, or decay rates, of atoms and ions are of significant importance in atomic characteristics defining the lifetimes of excited states, widths and intensities of spectral lines, the interpretation and identification of x-ray spectra emerging from highly charged ions and many other physical applications require the knowledge of transition probabilities and lifetimes of excited states, which will be discussed in this chapter.

There are two main types of radiative transitions: electric multipole Eκ and magnetic multipole Mκ transitions (κ is a positive integer). Within the framework of quantum electrodynamics, the probability per unit time of a one-photon transition from an initial excited state $|a\rangle$ to a final state $|b\rangle$ is given in terms of the matrix element,

$$dA = \frac{e^2 w}{2\pi\hbar c}\left|\langle b|\, \boldsymbol{\alpha}\boldsymbol{\epsilon}^{*} e^{-i\mathbf{kr}}\, |a\rangle\right|^2 d\Omega, \tag{3.10}$$

where $w = (E_a - E_b)/\hbar$ is the frequency of the emitted photon, $\boldsymbol{\epsilon}$ is polarization vector, $\boldsymbol{\alpha}$ ate the usual Dirac matrices, $\mathbf{k}$ is the photon momentum and $d\Omega$ denotes the solid-angle element for the radiation. Here, $|a\rangle$ and $|b\rangle$ are the relativistic wavefunctions obtained from the Dirac equation with a certain effective potential. The radiative lifetime τ_k of an excited state k is the time during which the number of radiative particles decrease e times (the number e is Euler's number) via spontaneous decay mode to the low-lying states, it is defined as

$$\tau_k = \left[\sum_{i<k} A_{ik}\right]^{-1}, \tag{3.11}$$

where the A_{ik} are transition probabilities of all possible radiative transitions including forbidden and intercombination transitions.

For highly charged H- and He-like ions, the formulae for radiative probabilities A via electric or magnetic transitions between the ground and lowest excited states can be obtained in a closed analytical form. These formulae are useful because they reflect the dependence of the $A-$values on the nuclear charge and transition energies. The analytical formulae given below were obtained on the basis of relativistic calculations using Eq. 3.10. Experimentally, most of the data on lifetimes for highly charged ions (HCI) had been obtained employing the beam-foil time-of-flight method covering a wide range of ion charges. Radio frequency traps, ion storage rings [114], and electron-beam ion traps [115] are all qualified for precise lifetime measurements of HCI having one or two electrons outside a closed shell, permit systematic checks of theoretical predictions.

3.3.1 Hydrogen-like ions

In the case of H-like ions, the transition probabilities of the lowest excited states can be expressed in a closed analytical form. The $2s$ state has the same parity as the $1s$ ground state, therefore it can decay to the ground state either by a magnetic dipole transition ($M1$) or by a two-photon electric-dipole transition ($2E1$). For $M1$ transitions the leading term of the relativistic transition probability [116] is

$$A_{M1}\left(2s \to 1s\right) = \frac{\alpha(\alpha Z)^{10}}{972}\frac{m_e c^2}{\hbar} \simeq 2.49 \times 10^{-6} Z^{10}\left[\mathrm{s}^{-1}\right], \tag{3.12}$$

where Z is the nuclear charge number of the ion.

An accurate relativistic calculations for the $2E1$ transitions, take place via intermediate virtual states, in H-like ions had also been carried out late by Drake [117], the corresponding probability can be approximated by a simple analytical expression

$$A_{2E1}\left(2s \to 1s\right) = 8.22983 Z^6 Z_r^4 (1 - m_e/M) \times \frac{1 + 3.9448\left(\alpha Z\right)^2 - 2.040\left(\alpha Z\right)^4}{1 + 4.6019\left(\alpha Z\right)^2}\left[\mathrm{s}^{-1}\right], \tag{3.13}$$

where $-Z_r e$ is the effective radiative charge for the electron, the coefficients of $\left(\alpha Z\right)^2$ represent an empirical fit to the direct relativistic calculations with an error of less than $\pm 0.005\%$ in the range $1 \leq Z \leq 92$. Moreover, $Z-$dependent behavior of one-photon transition probabilities may also be analytically approximated from the properties of Dirac's eigenfunctions by taking the leading term in an expression of $A-$values in powers of αZ [118]. This approach is rather accurate for electric dipole transitions $E1$ with low principle quantum numbers, becoming less accurate for all others. The complete picture of selection rules and orders of magnitude for transitions to the ground state from the first excited levels $n = 2$ are exhibited in Table 3.4. To get an intuitive insight, Fig 3.5 shows the decay scheme and the corresponding transition rates from $n = 2$ to $n = 1$ as function of Z in H-like ions.

Table 3.4: Approximate $Z-$dependent behavior of one-photon emission rates between the states with $n = 1, 2$ in H-like ions.

Transition	Type	Δl	Δj	Order of magnitude
$2s_{1/2} \to 1s_{1/2}$	$M1$	0	0	Z^{10}
$2s_{1/2} \to 1s_{1/2}$	$2E1$	0	0	Z^{6}
$2p_{1/2} \to 1s_{1/2}$	$E1$	1	0	Z^{4}
$2p_{3/2} \to 1s_{1/2}$	$E1$	1	1	Z^{4}
$2p_{3/2} \to 1s_{1/2}$	$M2$	1	1	Z^{8}
$2p_{3/2} \to 2s_{1/2}$	$E1$	1	1	Z^{10}
$2p_{3/2} \to 2s_{1/2}$	$M2$	1	1	Z^{18}
$2p_{3/2} \to 2p_{1/2}$	$M1$	0	1	Z^{12}
$2p_{3/2} \to 2p_{1/2}$	$E2$	0	1	Z^{16}

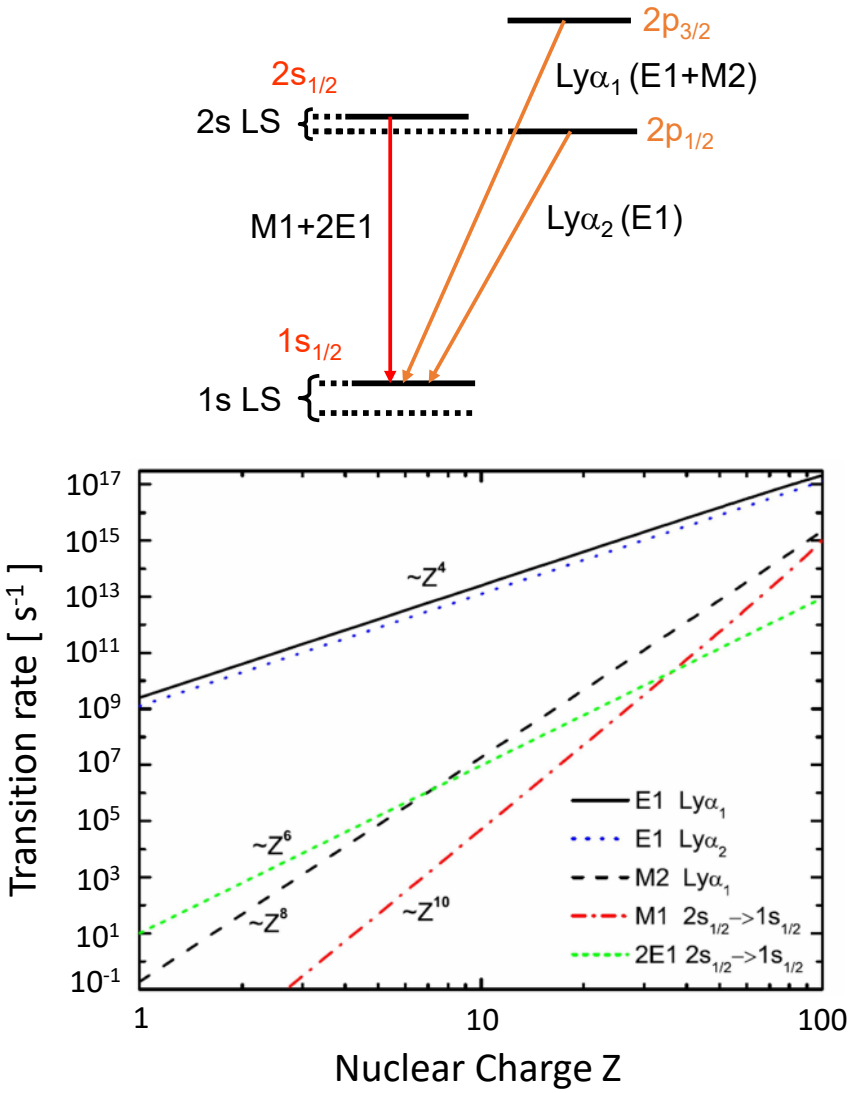

Figure 3.5: Level scheme (top) and transition rates (bottom) as an illustration between the states with $n = 1, 2$ in H-like ions. The transition rates are plotted as a function of nuclear charge number Z [118, 119, 120].

It can be noticed that the $M1$ transitions increase relative to $2E1$ transitions as Z^4 for the $2s$ state and these quantities become comparable at $Z \simeq 43$, and both A_{2E1} and A_{M1} values for $2s$ the state increase with nuclear charge Z more rapidly than the A_{E1} value for the electric dipole transition $2p_{1/2} \to 1s_{1/2}$, which approximately scales as $A_{E1} \sim Z^4$. For the heaviest ions the $M1$ transitions represent the main contribution to the radiative decay of the $2s$ state, for example, the ratio A_{M1}/A_{E1} strongly increases with Z and for H-like uranium reaches the value of about 4.07×10^{-3}, a factor of 12 larger than that of hydrogen. The decay mode for $2p_{3/2} \to 1s_{1/2}$ transition are electric-dipole ($E1$) and magnetic-quadrupole ($M2$) channels, the transition probability for $M2$ decay mode is calculated to be two orders of magnitude less than $E1$ transition rate for H-like uranium. Therefore, for heavy-Z H-like ions one should keep in mind that the Lyα_2 line ($2p_{1/2} \to 1s_{1/2}$)

is blended by the $M1$ transition type ($2s_{1/2} \rightarrow 1s_{1/2}$), and the interference between the $E1$ and $M2$ transition amplitudes may serve as a pronounced effect on the angular distribution and linear polarization of Lyα_1 x-rays following radiative electron capture [121, 122].

Following the work of Pal'chikov [118] who discussed a set of analytical formulas for $E1$, $M1$, $E2$, and $M2$ transition probabilities in H-like atoms and restricted to a subset of all state transitions that may take place between $1s$, $2s$, $3s$, $2p$, $3p$, $4p$, and $3d$. Jitrik and Bunge [119] extended the scope of the relativistic calculations with point-nucleus Dirac eigenfunctions up to $E3$ and $M3$ transition probabilities with large quantum numbers for Z=1-118, and the necessary consideration of different multipole decay mode when more than one is present in a given transition. In contrast to the $E1$ transitions, the Z dependence of relativistic electric and magnetic multipole transitions, particularly the magnetic transitions, do not follow a simple power law, but are governed by the dominant power N and a small relativistic correction a, as expressed here [123]:

$$A(Z) = A(Z = 1)Z^{N \pm a}. \tag{3.14}$$

The significant conclusions shown in Table 3.5 exhibit in which case the weaker multipole partners become dominant within a complete set of transitions.

Table 3.5: Predominance of a given multipole over all allowed transition modes: A $\gg$ B indicates that B is less than 1% of A; A $>$ B, that may be a few percent of A; A $\geq$ B, that B may be smaller than a few percent of A.[123]

Multipoles	Condition
$E1 \gg M2$	$Z \leq 80$
$E1 > M2$	$Z > 80$
$E1 \gg E3$	all Z
$M2 \geq E3$	all Z, $\Delta l = 1$
$E3 \gg M2$	all Z, $\Delta l = 3$
$M1 > E2$	$\Delta n = 0$ and $\Delta l = 0$
$E2 \gg M1$	otherwise
$E2 \gg M3$	all Z

As expected, the $E1$ transitions prevail among both $E1$+$M2$ and $E1$+$M2$+$E3$ transition modes, this fact is reflected in coincidence with the corresponding results for low-Z ions. For $Z = 92$, however, the contribution of one percent in $M2$ transition is observed in intense transitions such as $2p_{3/2} \rightarrow 1s_{1/2}$ mentioned above. Surprisingly, the $M2$+$E3$ results are of particular interesting: for $\Delta l = 1$ and $\Delta j = 2$, $M2$ transition probability is larger than that of $E3$ but they are the same order of magnitude, taking the most intense line transition $3d_{5/2} \rightarrow 2p_{1/2}$ as an example, $E3$ contributes 24.2% for $Z = 1$ and increase slowly up to 28% for $Z = 92$; for

$\Delta l = 3$, $E3$ transitions take the essential part for all Z H-like systems, even though $M2$ channel still exist. $M1$+$E2$ and $M1$+$E2$+$M3$ are entirely dominated by $E2$ except for $\Delta l = 0$ transitions. In the $M1$+$E2$ transition $3p_{3/2} \to 2p_{1/2}$, the $M1$ contribution, negligible for $Z = 1$, increases from 0.1% for $Z = 47$ to 50% for $Z = 92$, since the dependence is $Z^{10\pm0.24}$. In the $M1$+$E2$+$M3$ transition $3p_{3/2} \to 2p_{3/2}$, *i.e.* $\Delta n = 0$ and $\Delta l = 0$, $E2$ only contributes 2.5% for $Z = 92$. In contrast to the ($E1$, $M2$) pair, ($E2$, $M3$) behaves differently as $E2$ always dominant for all Z in $E2$+$M3$ transitions, a contribution of 1.2% of $M3$ in the transition $3d_{5/2} \to 1s_{1/2}$, for example, is estimated for H-like uranium.

3.3.2 Helium-like ions

He-like ions are the simplest many-electron systems. However, the situation of transition probabilities is complex because the atomic structure in He-like ions changes drastically with an increasing nuclear charge. For the ion with two electrons the states are described by the jj coupling scheme. In the pure LS coupling all intercombination transitions $\Delta S = 1$ are forbidden. However, in highly charged ions the selection rule $\Delta S = 0$ is violated through influences of relativistic effects (electromagnetic interactions) which rapidly increase with growing nuclear charge Z. Consequently, the intensive intercombination and forbidden lines are possibly observed by means of experiments for high-Z ions [102]. As in the one-electron case, the theoretical investigation of radiative decay modes for two-electron ions had already been studied thoroughly. Accurate nonrelativistic calculations of transition probabilities in He-like ions [117, 124, 125] have mainly been made for $n = 2 \to n = 1$ and for $n = 2 \to n = 2$ transitions. Relativistic calculations of transition probabilities of high-Z ions are based on the Relativistic Random-Phase Approximation (RRPA) [126, 127], the Multiconfiguration Dirac-Fock (MCDF) [128], Configuration Interaction (CI) expansions [129], relativistic many-body theory [130], and the QED perturbation theory [131, 132], sophisticated relativistic calculations of transition amplitudes and probabilities have been performed in the helium isoelectronic sequence up to the nuclear charge $Z = 100$ [133]. Table 3.6 summarizes the approximate Z dependence of the transition probabilities A in He-like ions for transitions between the $n = 1$ and $n = 2$ states on the basis of sophisticated calculations [133] and fitted in the form [134]:

$$A = a(Z - b)^c \left[\mathrm{s}^{-1}\right]. \tag{3.15}$$

For highly charged heavy ions the decay of triplet states increases dramatically due to the relativistic effects, and the excited L states decay promptly to the ground state, except the $2\,^3P_0$ state. From the point of theoretical and experimental interest, some transition types, dominantly contribute to the intense line intensities, will be discussed below.

Table 3.6: Approximate scaling of the transition probabilities A with the nuclear charge number Z and fitting parameters a, b and c for transitions between $n = 2$ and $n = 1$ levels in He-like ions [133, 134].

Transition	Type	Range of Z	a	b	c
$2\ ^1P_1 \to 1\ ^1S_0$	$E1$	$Z < 80$	$9.6\times\ 10^8$	-0.5	4.0
$2\ ^1P_1 \to 2\ ^1S_0$	$E1$	$Z < 30$	$1.5\times\ 10^4$	-2.14	3.0
$2\ ^1P_1 \to 2\ ^3S_1$	$E1$	$Z > 4$	0.66	1.18	6.0
$2\ ^1S_0 \to 2\ ^3S_1$	$M1$	$2 < Z < 50$	$1.8\times\ 10^{-8}$	1.25	7.0
$2\ ^1S_0 \to 2\ ^3P_1$	$E1$	$10 < Z < 20$	10.8	0.62	2.0
$2\ ^1S_0 \to 1\ ^1S_0$	$2E1$	$Z > 2$	16.5	0.8	6.0
$2\ ^3S_1 \to 1\ ^1S_0$	$M1$	$4 < Z < 80$	$1.8\times\ 10^{-6}$	0.56	10.0
$2\ ^3S_1 \to 1\ ^1S_0$	$2E1$	$Z < 25$	$9.2\times\ 10^{-10}$	1.0	10.0
$2\ ^3P_1 \to 1\ ^1S_0$	$E1$	$6 < Z < 20$	551.0	2.57	8.0
$2\ ^3P_1 \to 1\ ^1S_0$	$E1$	$Z \geq 20$	$6.48\times\ 10^8$	4.13	4.0
$2\ ^3P_1 \to 2\ ^3S_1$	$E1$	$Z < 50$	$1.33\times\ 10^7$	-0.57	1.0
$2\ ^3P_1 \to 2\ ^3S_1$	$E1$	$Z \geq 50$	$1.1\times\ 10^6$	18.25	2.0
$2\ ^3P_2 \to 2\ ^3S_1$	$E1$	$15 < Z \leq 20$	$3.73\times\ 10^9$	10.97	1.0
$2\ ^3P_2 \to 2\ ^3S_1$	$E1$	$Z > 20$	$5.3\times\ 10^8$	5.29	4.0
$2\ ^3P_2 \to 1\ ^1S_0$	$M2$	$Z < 80$	0.038	0.69	8.0
$2\ ^3P_2 \to 2\ ^1S_0$	$M2$	$Z \geq 20$	$1.23\times\ 10^{-9}$	17.5	8.0
$2\ ^3P_0 \to 2\ ^3S_1$	$E1$	$Z < 50$	$1.33\times\ 10^7$	-0.57	1.0

All the three $2\ ^3P_{0,1,2}$ levels can decay to $2\ ^3S_1$ state via optically allowed $E1$ transition, this is the dominate decay mode for low nuclear-charge numbers. The $2\ ^3P_1$ state is mixed with $2\ ^1P_1$ and other $1snp\ ^1P_1$ states because of spin-orbit interaction. The mixture is smaller for low-Z ions like helium but increase rapidly with large nuclear charge numbers. For helium: $A_{\rm He}(2\ ^3P_1 \to 1\ ^1S_0) = 1.787 \times 10^2\ {\rm s}^{-1}$, $A_{\rm He}(2\ ^1P_1 \to 1\ ^1S_0) = 1.799 \times 10^9\ {\rm s}^{-1}$. For He-like uranium: $A_{\rm U^{90+}}(2\ ^3P_1 \to 1\ ^1S_0) = 2.994 \times 10^{16}\ {\rm s}^{-1}$, $A_{\rm U^{90+}}(2\ ^1P_1 \to 1\ ^1S_0) = 5.001 \times 10^{16}\ {\rm s}^{-1}$. The $2\ ^3P_{0,2}$ levels do not mix with the singlet system and they have lifetimes ~ 10 times higher as compared to the $2\ ^3P_1$ level. $2\ ^3P_2$ and $2\ ^3P_0$ have two decay branches each, the $2\ ^3P_2$ state consists of $2\ ^3P_2 \to 2\ ^3S_1$ ($E1$) and $2\ ^3P_2 \to 1\ ^1S_0$ ($M2$) decay modes, the $2\ ^3P_0$ state consists of $2\ ^3P_0 \to 2\ ^3S_1$ ($E1$) and $2\ ^3P_0 \to 1\ ^1S_0$ ($E1M1$) decay modes. As a result, the deexcitation from the $2\ ^3P_2$ state contributes to both $K\alpha_1$ and $K\alpha_2$ lines and the $2\ ^3P_0$ state contributes to the $K\alpha_2$ line via the $E1$ decay branch to the $2\ ^3S_1$ state, the $2\ ^3S_1$ state can decay to the ground state by a relativistically induced $M1$ transition, and emits the $K\alpha_2$ radiation. The direct decay from the $2\ ^3P_0$ state to the ground state proceeds via two-photon emission ($E1M1$), thus it does contribution to the $K\alpha_2$ line with similar consideration of the $2\ ^1S_0$ state decays to the ground state by a two-photon emission $2E1$. Theoretical analysis shows that the probability of $2\ ^3P_2$ state decays to the ground state by an

$M2$ transition, contributing to $K\alpha_1$ line, is small for the low-Z systems, but it becomes the dominant depopulation mode of the $2\,^3P_2$ state for $Z > 20$ as $A_{M2} \sim Z^8$. Another contribution branch to $K\alpha_1$ line is the $2\,^1P_1$ level decay directly to the ground state by $E1$ radiation. To complete the illustration, Fig 3.6 depicts the energy levels and decay scheme for He-like heavy ions, the transition rates are nuclear charge Z dependence.

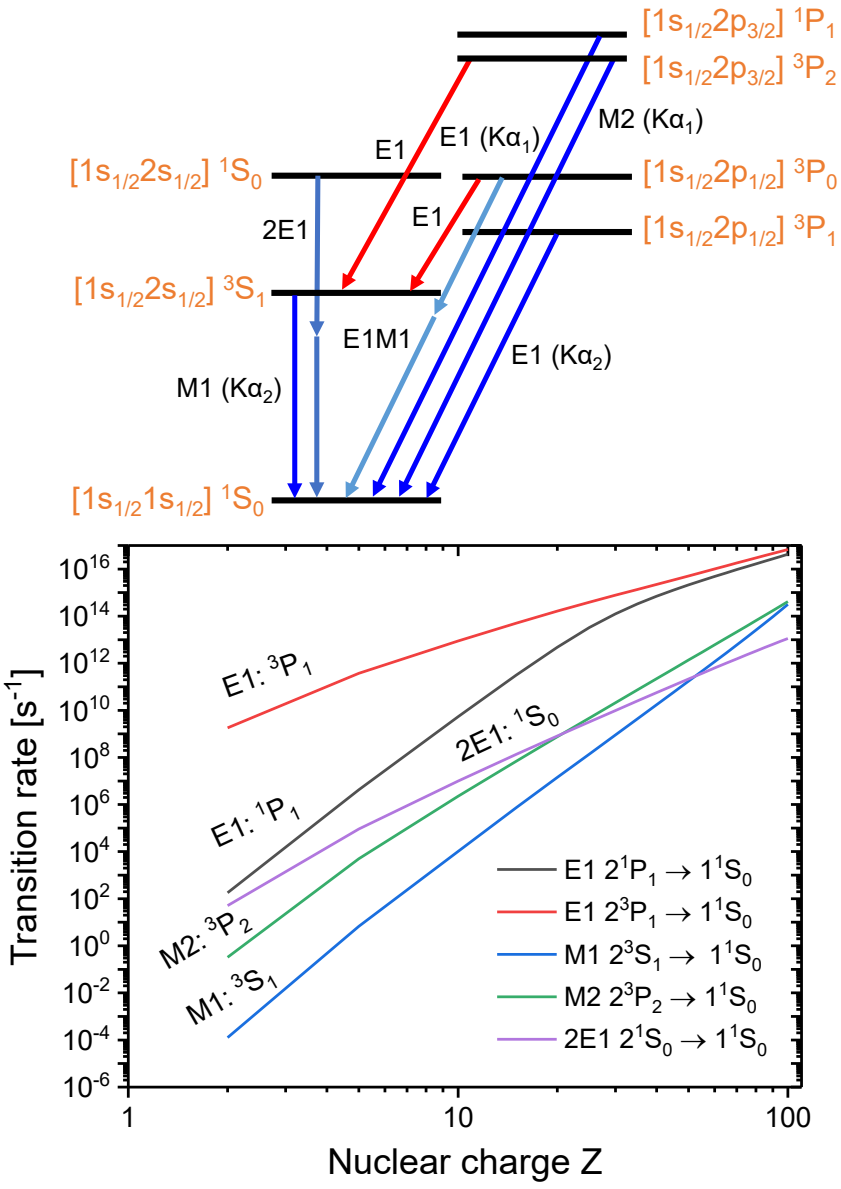

Figure 3.6: Level scheme (top) and transition rates (bottom) as an illustration between the states with $n = 1, 2$ in He-like ions. The transition rates are plotted as a function of nuclear charge number Z [133, 134].

3.4 Computations

Since no existing database can provide the required extensive set of energy levels, radiative transition rates for the relevant ions of few-electron systems, the input

data for radiative recombination related x-ray spectrum simulation need to be generated using accurate atomic code. The Flexible Atomic Code (FAC) developed by Gu [135, 136] based on the relativistic configuration interaction method with independent-particle base wavefunctions was used to generate the required atomic data, in which QED corrections are treated as hydrogenic approximations for self-energy and vacuum polarization effects, and relativistic corrections to the electron-electron interaction are included with the Breit interaction in the zero energy limit for the exchanged photon. For H-like uranium ions, the comparison of energy levels obtained from FAC code with the results from Johnson and Soff [79] as well as from Yerokhin and Shabaev [98] result in an accuracy up to a few eV, and the radiative transition rates are accurate to 99% when compared with tabulated data from Pal'chikov [118], considering relativistic corrections and the retardation effects. For He-like uranium system, deviations on the energy level calculated from FAC code compared to the reference data from Artemyev *et al.* [101] are within 8 eV. This good agreement ensures precise identification of transition types of the observed x-ray peaks in our experiment discussed in Chapter 5 and Chapter 6.

For high Rydberg states of quantum number $n > 100$, a fast computation code [137] was applied for the evaluation of radiative properties in nonrelativistic hydrogenic systems of H-like ions. For bound-bound transitions, the technique based on recurrence relations calculating the dipole matrix elements had proved to be accurate and stable for values of the quantum number n up to $n = 500$.

Chapter 4

Theoretical background: radiative recombination

Extensive theoretical and experimental studies have been carried out for the past 30 years on electron-ion recombination processes, as they are applied to the analysis of astrophysical and laboratory plasmas. Firstly, the basic understanding gained through these efforts will be reviewed, with emphasis on some of the more recent progress made in recombination theory as the recombining system is affected by time-dependent electric fields and plasma particles at low temperature. The radiation emitted by plasmas is usually the principle medium with which to study the plasma condition, as it is produced mainly during the recombination and decay of excited states of ions inside the plasma. This is especially true when the plasmas under study is not readily accessible by direct probes, as in astrophysical plasmas. Therefore one may really into performing astrophysical relevant studies in the laboratory by means of modern accelerators for ions as well as powerful laser light in the XUV and the x-ray wavelength regime, enabling to collect precise atomic data analysis about cross sections of radiative and recombination processes of multiply charged ions. These electron-ion recombination processes may serve as a prerequisite both for the diagnostics and modeling of laboratory fusion and astrophysical plasmas.

4.1 Description of recombination processes

Electron-ion recombination processes play an important role in the determination of the ionization-recombination balance of highly charged ions both in electron-ion beam colliding experiments and in high temperature laboratory and astrophysical plasmas. Motivations for studying these processes include an understanding of fundamental processes in reactions of free electrons with ions, determination of the corresponding cross sections and rate coefficients for use in models of energy trans-

port phenomena and plasma diagnostics.

Electron-ion recombination proceeds in several different modes. The direct modes include one-step radiative recombination (RR) and three-body recombination (TBR), all to the ground- and singly-excited states of the target ions. On the contrary, the indirect resonant mode is a two-step dielectronic recombination (DR), which proceeds first with the formation of doubly-excited states by radiationless excitation via a free electron capture. The resonant states formed thus may relax by autoionization or radiative cascades. For more exotic modes of recombination, it is so called radiative dielectronic recombination (RDR), in which an electron capture is accompanied by simultaneous radiative emission and excitation of the target ion.

Here, schematically description of various recombination processes follows as

$$X^{q+}(i) + e^- \rightarrow X^{(q-1)+}(f) + \hbar\omega \quad \text{(RR)} \tag{4.1}$$

$$X^{q+}(i) + e^- \rightarrow X^{(q-1)+}(d) \rightarrow X^{(q-1)+}(f) + \hbar\omega \quad \text{(DR)} \tag{4.2}$$

$$X^{q+}(i) + e^- \rightarrow X^{(q-1)+}(d) + \hbar\omega \quad \text{(RDR)} \tag{4.3}$$

$$X^{q+}(i) + e^- + e^- \rightarrow X^{(q-1)+}(d) + e^- + E_{kin} \quad \text{(TBR)} \tag{4.4}$$

The main and the simplest recombination mechanism in bare ions is the radiative recombination (RR) or radiative electron capture (REC), in which a free electron or quasi-free target electron is transferred via the photon interaction to the final bound atomic state. In both cases the photon carries away the difference in energy and momentum between the initial and final electron state. RR is the time reversed process to photoionization (PI). Fig. 4.1 demonstrates quite clearly the equivalence of PI and RR (or REC). In the atomic reference system the energy of the photon, $\hbar\omega$, is given by energy conservation:

$$\hbar\omega = E_{kin} + E_{bin} \tag{4.5}$$

where E_{kin} and E_{bin} correspond to the kinetic energy of the free electron and to the binding energy in its final atomic state, respectively.

Dielectronic recombination (DR) is a resonant recombination of a free electron with an ion X^{q+} bearing one or more core electrons. Schematically it can be identified with two-step processes, as depicted in Fig. 4.2. In a first step, often referred as dielectronic capture, a free electron is radiationless transferred to a bound state of the ion and a core electron is simultaneously excited forming a doubly excited state $X^{(q-1)+}(d)$. Because of the quantization of the ionic energy levels, the kinetic energy of the electron has to fulfill a resonance condition for the process to become possible. The dielectronic capture, with two electrons involved, is the inverse of the Auger process. This means that the DR process can occur only if the incident ion X^{q+}

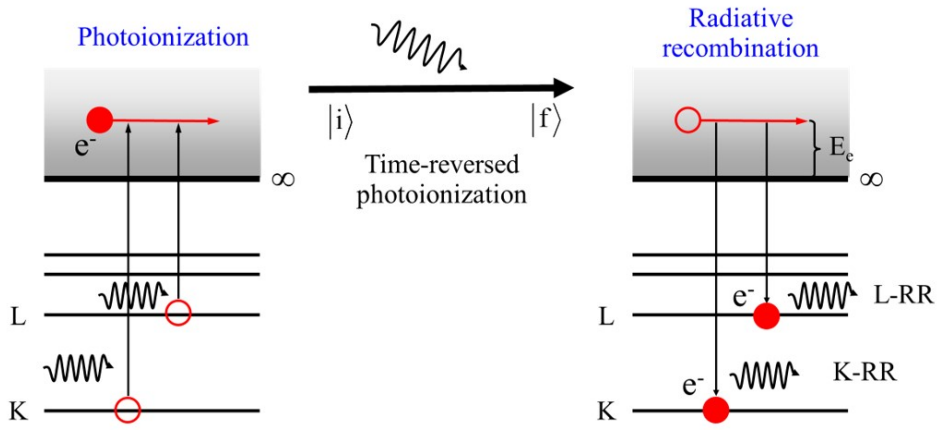

Figure 4.1: Schematic sketch of the time reversed processes: [left] the photoionization (PI) and [right] the radiative recombination (RR). In this example, the ground state K shell and first excited state L shell are shown for illustration.

has one or more core electrons, i.e. DR cannot occur with bare ions. In a second step, the doubly excited ion can radiatively stabilize by decaying to a lower level or to its ground state below ionization limit. Alternatively the doubly excited ion may autoionize thus returning to its original charge state in which case a resonance feature in the elastic scattering will occur.

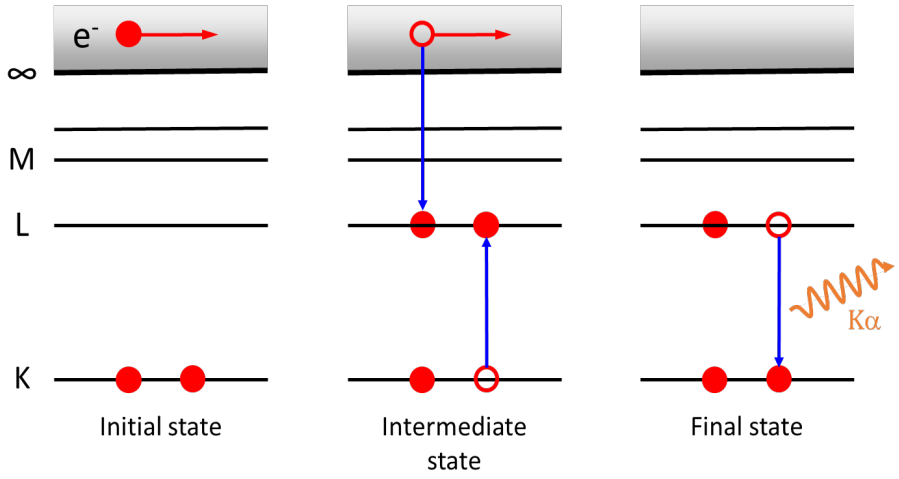

Figure 4.2: Schematic representation of the dieelectronic recombination process. The example is for a KLL resonance in a He-like ion.

DR process is also similar to radiative recombination, in both cases a free electron is captured in the Coulomb field of the ion and a photon is emitted, but in radiative recombination, a photon is radiated due to the transition of a captured electron from an upper state to a lower one, while in dielectronic recombination a photon is radiated due to the transition of a core electron.

There is a competitive process for the decay of the doubly excited ion in Eq. 4.2, that is the autoionization or Auger decay associated not with the radiative transition

but with a change in ion charge:

$$X^{q+}(i) + e^- \rightarrow X^{(q-1)+}(d) \rightarrow X^{q+}(f) + e^- \tag{4.6}$$

However, in highly charged ions, the decay via DR with photon radiation is a more probable process than Auger stabilization with emittance of a free electron.

Another recombination mechanism possible for a bare ion is the three-body recombination (TBR), this process is the time-reversed electron-impact ionization and involves high-Rydberg states with binding energies comparable to the thermal energy kT_e of the electrons. Thus, TBR process is important at high electron densities and very low center-of-mass energies between electrons and ions. The presence of a third particle, i.e. an electron in the process, is necessary to fulfill the momentum and energy conservation, as shown in Fig. 4.3. The difference to DR is that the energy produced by the capture of an electron in continuum state is transferred to a second free electron as kinetic energy and consequently it is not a resonance process. TBR is quite poorly investigated both experimentally and theoretically although it constitutes a crucial charge-changing reaction at low electron temperatures and high plasma densities.

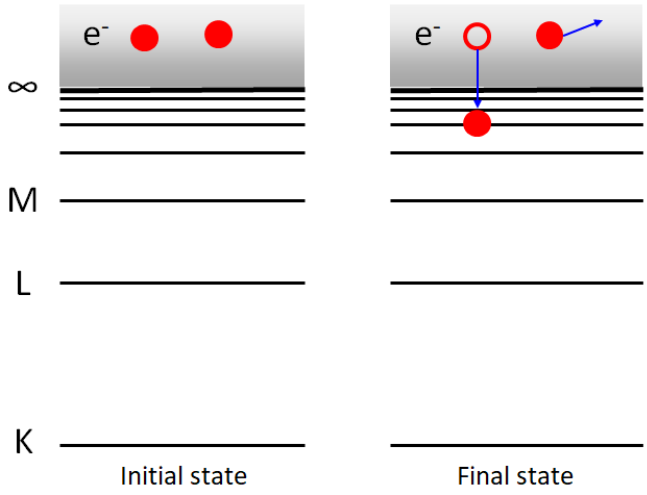

Figure 4.3: Schematic representation of the behavior of three-body recombination process at low relative velocity. The example is for a bare ion.

The RR and DR exhibit quite different dependence on the kinetic energy of the free electron to be captured. The RR, which can be calculated in a closed analytical form [76, 138], attains its maximum if the relative velocity between ion and electron becomes zero, since the RR cross section roughly scales as $1/E_e$ at low kinetic energy E_e of the electron. However, it had been shown [139] that it stays finite for $E_e \rightarrow 0$ if the velocity distribution of cooling electrons is taken into account. Based on these calculations, a radiative recombination rate $\alpha_{RR} = 1/\tau_{RR}$ which is roughly proportional to Z^2, can be estimated.

On the contrary, DR is a resonant process and the resonance condition implies a stringent restriction to the kinetic energy of the free electron. In order to excite the bound electron from state $n1$ to state $n2$, the following energy resonance condition has to be fulfilled

$$E_{n1} - E_{n2} = E_e + E_{n2}. \tag{4.7}$$

This equation shows that the DR cross section will be maximal for electron energies E_e which are determined by the differences of the binding energies of the states involved in the capture. Since these differences usually are not zero (especially if the $1s$ state is involved), recombination processes via DR are crucial only if the electron beam is detuned with respect to the ion beam.

In general, among possible recombination mechanisms of radiative recombination and three-body recombination for bare projectiles at high atomic number Z, TBR, involving loosely bound states, has a smaller contribution rate for typical electron densities and temperatures at an electron cooler [17, 140]. For incoming ions that carries one or more electrons dielectronic recombination is also a possible channel. In the case of H-like ions at high Z, excitation of the $1s$ electron requires a large amount of energy and the DR resonances start at a relatively large impact energy [141]. With the tightly bound $1s$ electron of the H-like heavy ions and electron beam temperature of a few meV achieved in our experimental setup discussed in Chapter 5, however, we are far away from fulfilling the required resonance condition. Therefore, radiative recombination is the most dominant electron-ion recombination mechanism for the systems considered here, and will be discussed in more detail.

4.2 Radiative recombination cross sections

The results of a long-term study of the process of radiative recombination are reviewed in this section. Rigorous descriptions of both nonrelativistic and relativistic electron RR with a hydrogen-like ion are formulated to calculate the state selective RR cross sections.

4.2.1 Nonrelativistic theory

In the past, the radiative recombination process had been studied theoretically starting in the 1920's. Kramers [142] was the first one to obtain an approximate expression for the RR cross section for the hydrogenic target. His mathematical model was based on a semiclassical approach that uses Bohr's correspondence principle because the coupling of matter with the radiation field was not yet fully developed quantum mechanically. Later, Kramers formula was modified to incorporate quantum mechanical effects. Gordon [143] was the first to apply first-order perturbative quantum theory to the RR process. The most extensive study of the process were

done by Stobbe and Burgess *et al.* [138, 144]. More detailed history related to a long-term study of nonrelativistic electron RR theory was reviewed in recent published paper [145]. The principle goal has been to find approximate approximations to overcome the larger and tedious numerical calculations involved. The difficulties mainly originated from the treatment of the excited states of the recombined atom especially for the higher orbitals.

The RR cross section involves interaction matrix element between the initial free and the final bound states. For captures to excited states of the target ions, a sum over all the allowed final states is to be performed. Since the initial and final wave functions are known analytically in the case of a pure coulomb field from a bare ion, the RR cross section is calculated exactly from its time-reversed photoionization process (for details, see Appendix A.1).

For the ions with one or more electron before capture, the pure Coulomb approximation with an effective charge Z_{eff} may be adopted to treat approximately the screening effect due to the inner-shell electrons and calculate the RR cross sections. In the pure Coulomb approximation, the continuum and bound wavefunctions are calculated by Coulombic wave and hydrogenic approximation, respectively. However, it is difficult to choose a suitable effective charge Z_{eff}. Usually, the effective charge Z_{eff} is taken in the following simple form [146, 147],

$$\begin{aligned} Z_{eff} &= \frac{1}{2}(Z_C + Z_I) \quad for \quad Z_C \geq Z_I \geq \frac{Z_C}{2}, \\ Z_{eff} &= \sqrt{Z_C Z_I} \quad for \quad \frac{Z_C}{2} \geq Z_I \geq 1, \end{aligned} \tag{4.8}$$

where Z_C is the nuclear core charge and Z_I is the degree of ionization before capture.

In fact, the screening effect depends on the quantum number (n, l) of captured electron, resulted from the incident electron energy k^2 in the ion rest frame. As k^2 increases, the projectile electron starts to penetrate more into the core shells. On the other hand, the structure of target ion has a crucial influence on the effective charge Z_{eff}, due to ion charge Z_I, nuclear charge Z_C and the distribution of the bound electrons.

Later, after extensive comparison between the RR cross sections calculated with the wavefunctions (both in bound and continuum state) obtained from Hartree-Fock method and from the pure Coulomb approximation, respectively, an improved empirical formula of the effective charge Z_{eff} is suggested by McLaughlin and Hahn [148, 149], as

$$Z_{eff} = \left(Z' - \frac{Z_C - Z_I}{2} \frac{\eta' - 1}{\eta' + 1 + 3l} \right) e^{-0.05(l-1)^2}, \tag{4.9}$$

where

$$Z' = \frac{Z_C + Z_I}{2}, \quad \eta' \equiv \frac{Z'}{k}, \tag{4.10}$$

for $n \geq n_0 + 1$, which is mildly k dependent, and for $n = n_0$ where n_0 is the highest occupied shell before capture. For capture into $n = n_p$, where the (n_p, l_p) shell is partially filled, the core penetration is strong, and Z_{eff} seems to be independent of k, as

$$Z_{eff} = 1.1 \times Z'. \tag{4.11}$$

4.2.2 Relativistic theory

The cross sections given in nonrelativistic treatment are not valid for high photon and hence electron binding energies, because these approximation for total and sometimes even for differential cross sections carry farther than one should expect. The exact evaluation of the relativistic photoelectric or, inversely, the RR cross section requires a partial-wave expansion of the Coulomb-Dirac wave functions for the bound and for the continuum states modified for the finite nuclear size. This means that closed-form expressions can no longer be derived, and one has to resort to numerical methods. Detailed formulations exist since a long time which can be found in [150, 151, 152]. Since existing tabulations [153, 154] are not always sufficient in connection to RR cross sections, independent computer codes have been developed and successfully applied in our data analysis. An outline of the formulation is presented in Appendix A.2, assuming unpolarized photons and a polarization-insensitive detector for the emitted electrons. In the calculations, all multipoles of the electron-photon interaction under inclusion of retardation effects are taken into account.

While the direction of the photon is usually taken as the quantization axis, which provides a simple treatment of the photon wavefunction, what adopt here is the direction of emission of the electron as quantization axis. Each of these approaches are valid only if one performs a summation over the electron spin m_s. The choice here is base on the fact that the radiative recombination experiment was implemented at electron cooler devices where the direction of transverse electron beam defines the z axis. In this case, the notation of spin-flip and non-spin-flip is meaningful only, if the spin of the bound state as well as of the continuum electron is quantized along the direction of motion. Similarly, the notation of alignment or of population of magnetic sublevels in terms of RR into excited states followed by radiative decay (time reverse to two-step photoionization process) [121, 152] makes sense only, if angular momenta are quantized with respect to the electron beam direction.

4.3 Radiative recombination rate coefficients

At electron cooler devices, when an electron beam has some velocity distribution $f(\mathbf{v})$, introducing an integrated quantity namely the rate coefficient α_{nl} instead

of the radiative recombination cross section, defined for a fixed electron velocity, appears to be more reasonable. The relation between the cross section σ_{nl} and the rate coefficient α_{nl} is given by

$$\alpha_{nl} = \langle v\sigma_{nl}(\mathbf{v})\rangle = \int v\sigma_{nl}(\mathbf{v}) f(\mathbf{v}) d^3v. \tag{4.12}$$

For the velocity distribution, the cooler electron beam usually is described in terms of an anisotropic Maxwell-Boltzmann distribution (also called a normalized flattened distribution) characterized by effective longitudinal $kT_\parallel$ and transverse $kT_\perp$ beam temperatures [155, 156]:

$$f(\mathbf{v}) = \left(\frac{m_e}{2\pi}\right)^{3/2} \frac{1}{kT_\perp (kT_\parallel)^{1/2}} \exp\left[-\left(\frac{m_e v_\perp^2}{2kT_\perp} + \frac{m_e v_\parallel^2}{2kT_\parallel}\right)\right]. \tag{4.13}$$

Quite generally, the effective electron beam temperatures in the projectile frame are characterized by the convolution of the electron and ion beam velocity distributions in the form of $(kT_{e\parallel}, kT_{e\perp})$ and $(kT_{i\parallel}, kT_{i\perp})$, respectively, they are given by

$$\begin{aligned} kT_\parallel &= kT_{e\parallel} + \frac{m_e}{M} kT_{i\parallel} \\ kT_\perp &= kT_{e\perp} + \frac{m_e}{M} kT_{i\perp}, \end{aligned} \tag{4.14}$$

where k is the Boltzmann constant, M and m_e are the ion and electron masses, respectively.

4.3.1 Analytical calculations

In a treatment given by Bethe and Salpeter [76] the dependence of the angular integrated total cross section on the quantum number n was obtained in the form, as

$$\sigma_n^{RR} = 2.10 \times 10^{-22} \frac{E_{1s}^2}{n(E_{1s} + n^2 E_e) E_e} \; [cm^2], \tag{4.15}$$

where E_e is the kinetic energy of the free electron, and E_{1s} is the binding energy of $1s$ state in H-like systems. This formula shows an important feature of radiative recombination, as the cross section varies with $1/n$ for $E_{1s} \gg n^2 E_e$, it gives $\sim 30\%$ into $1s$ state, $\sim 13\%$ into $n = 2$, and $\sim 8\%$ into $n = 3$ etc. Using these relations and the relations given by Spitzer [157], Bell and Bell [139] derived the following approximate analytical formula for the radiative recombination rate coefficient with a flattened velocity distribution (kT_e measured in eV):

$$\alpha^{RR} = \frac{3.02 Z^2}{\sqrt{kT_e}} \left[\ln \frac{11.32 Z}{\sqrt{kT_e}} + 0.14 \left(\frac{\sqrt{kT_e}}{Z^2}\right)^{1/3}\right] [cm^3/s], \tag{4.16}$$

which is valid as long as the relative kinetic energy between electrons and projectiles is comparable to kT_e. One could expect that radiative recombination is the main loss process during electron cooling.

To get an analytical formula of rate coefficients for state selective (n, l) states in the low-energy limit, Pajek and Schuch [155] calculated the asymptotic expressions for the dipole matrix elements when $E_e \ll E_{nl}$, where E_{nl} is the binding energy of the (n, l) state, showing that the radiative recombination cross section scale as $1/E_e$, and gives a simple analytical result for a fixed arbitrary (n, l) state:

$$\sigma_{nl}^{RR}(E_e) \approx \frac{E_{nl}}{E_e}\sigma(n, l), \tag{4.17}$$

where the reduced radiative recombination cross section $\sigma(n, l)$, in nonrelativistic dipole approximation, is given by [158]

$$\sigma(n, l) = \frac{\pi^2}{\alpha^3}a_0^2[(l + 1)c_{l+1}^2(n, l) + lc_{l-1}^2(n, l)]. \tag{4.18}$$

The radiative recombination rate coefficient can further be derived by the integration over an anisotropic electron-velocity distribution following Eq. 4.12, as [155]

$$\alpha_{nl}^{RR} = \frac{2}{\sqrt{\pi}}\alpha c Z^2 \frac{Ry}{(kT_\perp)^{1/2}}G(t)\sigma(n, l)/n^2. \tag{4.19}$$

Here $\alpha \approx 1/137$ is the fine structure constant, c is the speed of light and Ry denotes the Rydberg constant in unit of energy. The recombination rates scale with the ion atomic number as Z^2 and with the transverse electron beam temperature $kT_\perp$ as $1/(kT_\perp)^{1/2}$, while the longitudinal temperature $kT_\parallel$ enters only via the slowly varying function $G(t) = [(t + 1)/t]\arctan\sqrt{t}$ with the electron beam asymmetry parameter $t = (kT_\perp - kT_\parallel)/kT_\parallel$. However, one may question the quantitative condition for a validity of the low-energy approximation ($E_e \ll E_{nl}$), estimating how small the ratio E_e/E_{nl} should be to have an allowed accuracy of the analytical results.

For $n \gg 1$ the rate for RR into a fixed n-state α_n^{RR} can be expressed in a simpler form by using the low-energy expansion of the Kramers [142] semiclassical cross section:

$$\alpha_n^{RR} = \frac{64\sqrt{\pi}}{3\sqrt{3}}\alpha^4 a_0^2 c Z^2 \frac{Ry}{(kT_\perp)^{1/2}}G(t)g(n)/n, \tag{4.20}$$

where, practically, the Gaunt factor [158, 159] $g(n) \approx 1$ for high Rydberg states and a_0 denotes the Bohr radius.

For ions with core electrons, the recombination rates can only very roughly be determined from these formulas. One is neglecting the atomic structure and continuum electron exchange forces which are present when the ion has some electrons. It can be said that these forces are small but if the relative energy of the ions and the

electrons are tiny, like in an electron cooler, these effects may increase the "bare nucleus" direct radiative recombination rate for certain energies. Finally, I would like to emphasize that radiative recombination enhancement effects were well demonstrated experimentally for bare ions [160] up to U^{92+} [161], and also for many-electron ions [13, 162] at relative electron energies below the transverse electron beam temperature $kT_{\perp}$, by detecting the charge exchanged ions after the electron cooler using a dedicated particle counter.

4.3.2 Rigorous relativistic calculations

In the current study, a different calculation approach is used which exploits recursion relations shown in Eqs. A.16 - A.20 to evaluate the dipole matrix elements for radiative recombination cross sections in Eq. A.15, then the (n, l) rate coefficients for a flattened velocity distribution are performed via the integration according to Eq. 4.12. In contrast with the other methods, which exploit further approximations to calculate both the cross section and the integrals involved in the RR rate coefficient expression, here the exact calculations for the cross sections in the case of nonrelativistic energies were carried out using the Stobbe approach without any other approximation [144, 163]. The comparison with the fully relativistic results obtained by Ichihara and Eichler [153] showed that the dipole approximation proves to be appreciable in the low-energy regime, even for high nuclear charges as $Z = 92$. In such cases there are remaining differences which appear mainly in the case of the j-sensitive cross sections for small angular momentum quantum number l and in the case of angular distributions (see e.g. Ref. [8] and references therein).

For electron cooling conditions, as an example, retaining low relative energy of $E_{rel} = 2.6$ meV and choosing a high nuclear charge $Z = 82$, Sizeable differences in the j-sensitive cross section within 30% in particular for s-states can be obtained, see Fig. 4.4. The statistical weights considered for the Stobbe's calculations of n, l, j-sensitive cross sections are responsible for this discrepancies. This means that even for $n = 8$, relativistic effects in Pb^{82+} survive or, possibly, retardation effects (high powers in kr of photon field) play a role, owing to tighter binding. The pronounced deviation of the Stobbe theory from the rigorous treatment indicates the importance of introducing relativistic corrections, if one would like to apply nonrelativistic theory for RR rate calculations for each low-lying bound states, i.e. states with principle quantum number $n \leq 10$.

The exact evaluation of the relativistic photoelectric cross sections requires a partial-wave expansion of the Coulomb-Dirac continuum function. This means that closed-form expressions can no longer be derived, and one has to resort to numerical methods. The numerical evaluation of the RR cross sections into strongly bound projectile states were performed in a fully relativistic manner following the detailed

formulations in Appendix A.2. The accuracy of the calculation is mainly determined by the number of expanded partial waves, $\nu = 2\kappa_{max}$, with κ_{max} being the maximum quantum number for the Dirac angular momentum. For the expansion, a too small choice of κ_{max} may lead to truncation errors, whereas a too large value, on the other hand, may lead to explosion of numerical errors due to rapid oscillations of the radial part of the continuum wave function. In our calculations, all multipoles of the electron-photon interaction under inclusion of retardation effects are taken into account.

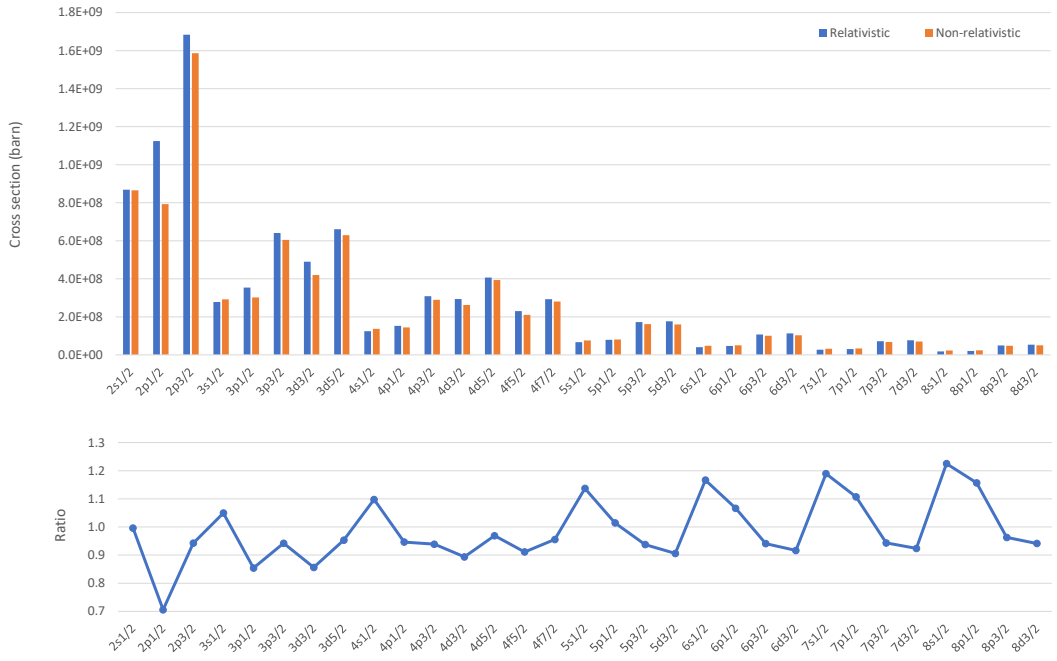

Figure 4.4: The RR cross sections as predicted by the exact treatment in comparison with the Stobbe approximation for the subshells of Pb^{82+} up to $n = 8$ at relative electron-ion energy of 2.6 meV. In the lower figure the deviation of both approaches is depicted.

For completeness, considering the cross sections for radiative recombination and electron velocity distribution at the cooler devices, the rate coefficient can be written in the form of

$$\begin{aligned}\alpha_{nl}^{RR} = &\int_0^{\infty}\int_0^{2\pi}\int_{-\pi/2}^{\pi/2} v\sigma_{nl}^{RR}(\mathbf{v})\left(\frac{m_e}{2\pi}\right)^{3/2} \\ &\times \frac{1}{kT_{\perp}(kT_{\parallel})^{1/2}}\exp\left[-\left(\frac{m_e\cos\phi^2}{2kT_{\perp}}+\frac{m_e\sin\phi^2}{2kT_{\parallel}}\right)\right] v^2\cos\phi dv d\psi d\phi.\end{aligned} \tag{4.21}$$

By using the following formula in connection with Gauss error function erf(z)

$$\int_{-1}^{1}\exp(-ax^2)dx = \sqrt{\frac{\pi}{a}}\mathrm{erf}(\sqrt{a}) \tag{4.22}$$

and several substitutions, the triple integral in Eq. 4.20 is reduced to a simple

integral, as

$$\alpha_{nl}^{RR} = \int_0^\infty \frac{c\alpha}{\sqrt{\pi}} \sigma_{nl}^{RR}(E_e) \frac{E_e^2}{kT_\perp Ry} \sqrt{\frac{Ry}{kT_\parallel}} \exp\left(\frac{E_e}{kT_\perp}\right) \times \sqrt{\frac{\pi kT_\parallel kT_\perp}{(kT_\perp - kT_\parallel)E_e}} \mathrm{erf}\left(\sqrt{\frac{(kT_\perp - kT_\parallel)E_e}{kT_\parallel kT_\perp}}\right) dE_e \tag{4.23}$$

with Ry the Rydberg unit of energy, and 1Ry $\approx 13.6\ eV$.

For the realistic experimental conditions, the electron beam temperature of $kT_\perp = 2.6$ meV and $kT_\parallel = 52\ \mu$eV was achieved at the electron cooler of CRYRING@ESR [164], where bare or few-electron ions could recombine with free electrons of continuum states. Figure 4.5 depicts the state selective total rate coefficients for radiative recombination into Pb^{82+} at the electron cooling temperature as a function of principal and angular momentum quantum number (n, l). As can be seen that the main contribution to the rate coefficients is given by the small l states, as is to be expected. However, due to the small relative velocity between projectiles and electrons, the contribution from high Rydberg states might have a significant contribution to the total rate coefficient.

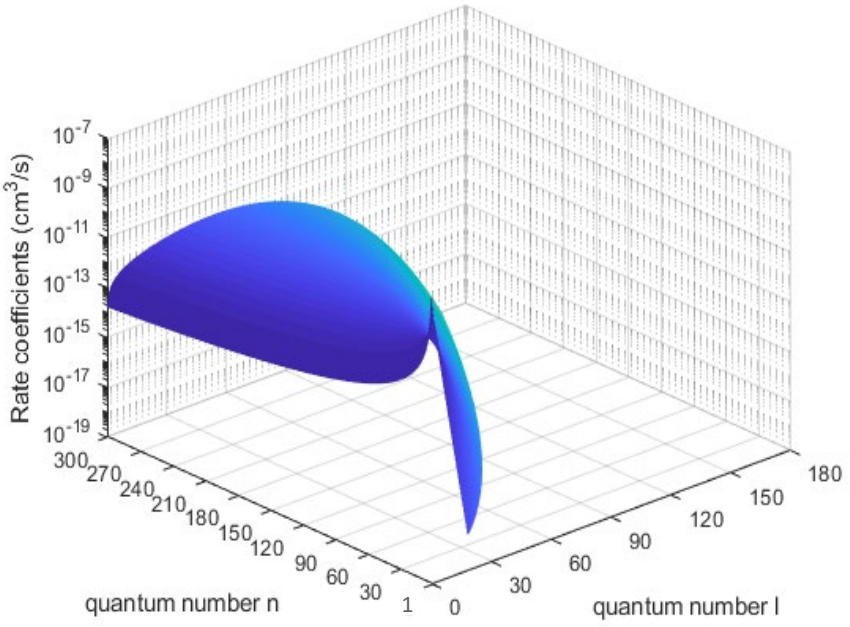

Figure 4.5: State selective (n, l) rate coefficients calculated for radiative recombination into bare lead ions for flattened electron velocity distribution with $kT_\perp = 2.6$ meV and $kT_\parallel = 52\ \mu$eV at the CRYRING@ESR cooler device. Here, n up to $n = 300$ and l up to $l = 180$ are displayed on the axis.

Fig. 4.6 varies the principle quantum number n from $n = 10$ to $n = 300$ to show the changes of magnitude in total rate coefficient. As can be seen that the n-RR contribution to the total rate coefficient increases rapidly until $n = 50$, because in radiative recombination much higher n-states contribute to the recombination

rates, which scale as $1/n$, as it is revealed in the figure that the occupation of K-shell population decrease from 32% (corresponding to $n = 10$) to 14% when the magnitude reaches saturation at $n = 300$. Thus, the recombination into these high levels is crucial for the study of characteristic projectile x-rays stemming from the radiative cascade of the electrons to the low-lying subshells.

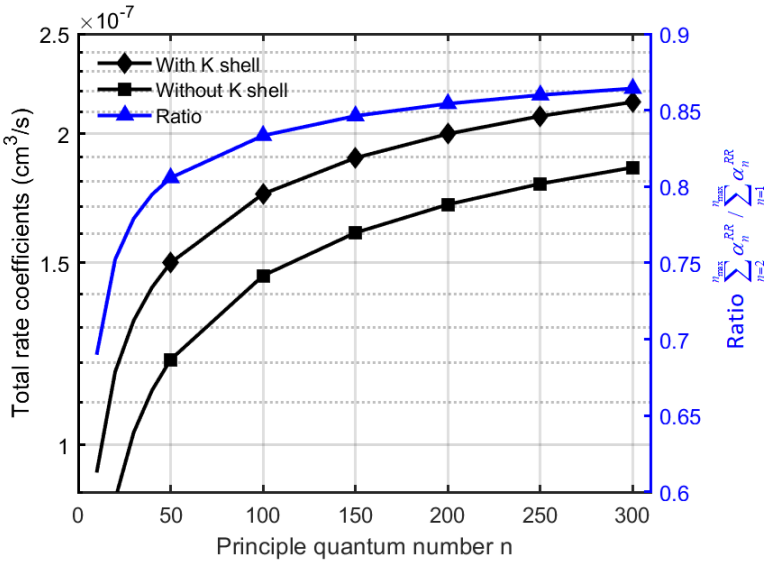

Figure 4.6: The total rate coefficient calculated for radiative recombination into bare lead ions is displayed as a function of the principle quantum number n. The ratio $\sum_{n=2}^{n_{max}} \alpha_n^{RR} / \sum_{n=1}^{n_{max}} \alpha_n^{RR}$ reveals that the rate coefficient is sensitive to the population distribution of high Rydberg states.

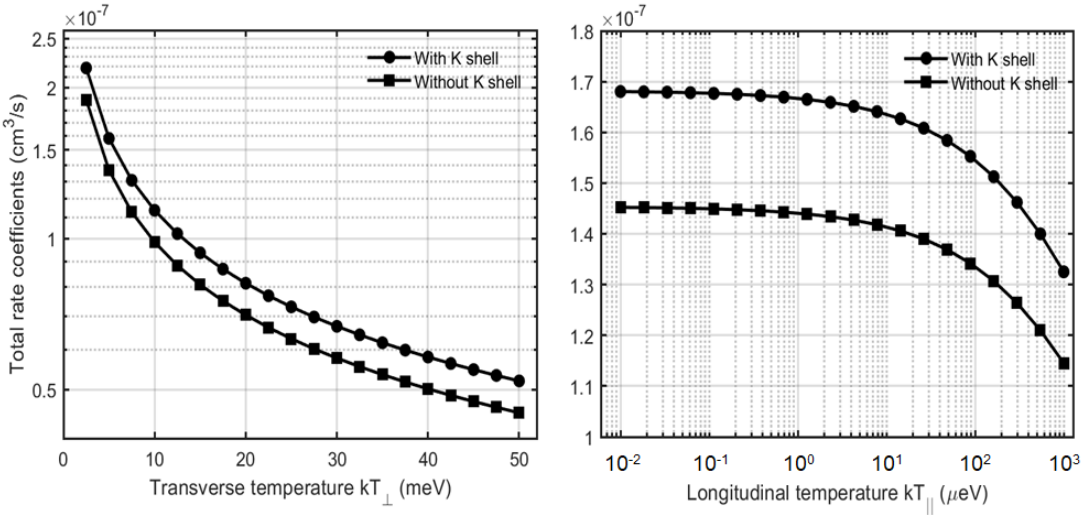

Figure 4.7: The radiative recombination rate coefficient is plotted [left] as a function of the transverse temperature $kT_\perp$ with a fixed longitudinal temperature $kT_\parallel = 50$ μeV, and [right] as a function of the longitudinal temperature $kT_\parallel$ with a fixed transverse temperature $kT_\perp = 5$ meV for nuclear charge $Z = 82$. Here, n up to $n = 300$ is included in the calculations.

From this point of view, it would be interesting to investigate the dependence

of rate coefficients on the longitudinal $kT_{\parallel}$ and transverse $kT_{\perp}$ electron beam temperatures, respectively for electron-ion merged-beam experiments at electron cooler devices. The contributions from $\sum_{n=1}^{n_{max}} \alpha_n^{RR}$ and $\sum_{n=2}^{n_{max}} \alpha_n^{RR}$ to the total rate coefficient are depicted in Fig. 4.7, and both cases show similar decreasing behavior of rate coefficient that scales as $1/E_e$ [155]. In the low-energy regime, the main quantum number $n = n_{max} = 300$ is included in the calculations, It was found that no more than 15% of projectile x-rays are from K-shell free electron capture. In practice, one may expect the characteristic x-ray radiations stemming from the cascade feeding from high levels would be registered at the low-energy part of the spectrum (e.g. Balmer spectrum), which is typical for the experiments in the storage ring utilizing an electron cooler as a target of free electrons. Furthermore, it is worth mentioning that the smaller is $T_{\parallel}$ with respect to the transverse temperature $T_{\perp}$, the influence of the longitudinal temperature on the total rate coefficients is tiny, i.e. the latter seems to be constant as a function of the longitudinal temperature $T_{\parallel}$ for $T_{\perp}/T_{\parallel} > 10^4$.

4.4 Angular distributions

Experimentally, the differential RR cross section can only be measured at forward or backward angles corresponding to the photon emission angle of 90°, based on the fact that at electron cooler devices the transverse temperature $kT_{\perp}$ of the electron beam is much larger than the longitudinal one $kT_{\parallel}$, thus, the collision axis is defined as the one perpendicular to the ion beam axis. For high-Z projectiles with a velocity large compared to the velocity $v_T = (\alpha Z_T/n_T)c$ of electrons bound in the n_T-shell of a light target atom, these electrons can be considered as quasi-free to a very good approximation [8]. It is then justified to ignore their momentum distribution with respect to the target nucleus and to identify RR with REC (radiative electron capture).

Under realistic conditions of REC experiment, the initial electron velocity is inverted in the projectile frame as compared to photoionization process, the angular distribution of the REC photons is directed backwards in the projectile frame. It is the relativistic transformation of the photon distribution from the moving system to the observer in the laboratory system which shifts the distribution forwards. In a first approximation it completely counterbalances the strong backward directed angular distribution in the projectile frame. Hence, for REC, at least into s-levels of the projectile, one expects a preferred photon emission perpendicular to the projectile direction [165]. The difference in the photon angular distribution between REC in the projectile frame and REC in the laboratory system is demonstrated in Fig. 4.8 for the case of 310 MeV/u U^{92+} ions assuming pure electric interaction. This corresponds to an electron impact leading to an emission of a 301.7 keV photon

(compare with the time reversed process in Fig. 4.1).

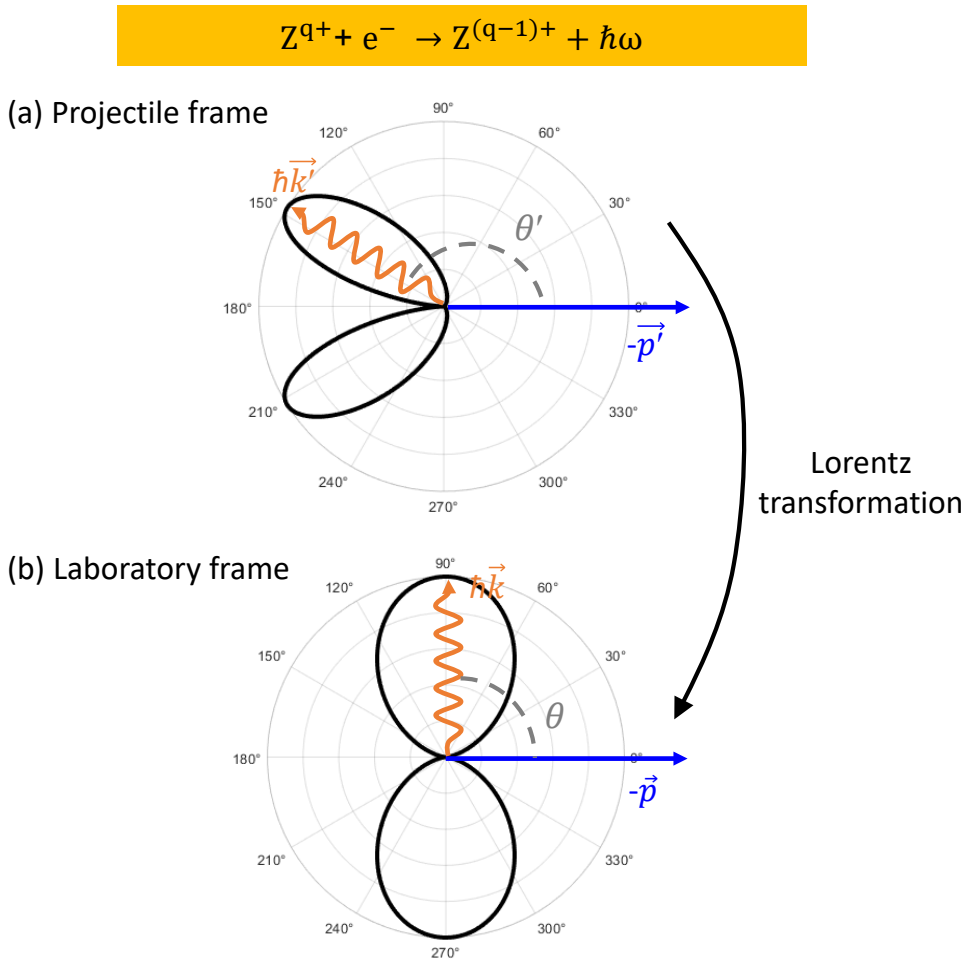

Figure 4.8: Photon angular distribution for REC into U^{92+} at 310 MeV/u calculated by assuming only electric interaction (top: projectile frame; bottom: lab. frame).

As depicted in the figure, the advantage of using the REC process for investigating PI arises from the combination of the following transformations one has to apply:

(a) The time reversal ($\mathbf{p}' \rightarrow -\mathbf{p}'$) which describes REC as time reversal of PI in the projectile frame. In this case, the angle θ' refers to the direction of the ion beam moving toward to the electrons, which is the direction opposite to the electron motion. This amounts to replacing θ'_{ph} by $\pi - \theta'$, alternatively, $\cos\theta'_{ph}$ is replaced by $-\cos\theta'$, where θ'_{ph} is the angle between the electron momentum $\mathbf{p}'$ and the photon momentum $\mathbf{k}'$. Thus, the state-to-state cross section for radiative recombination takes the form [166]

$$\frac{d\sigma^{RR}(\theta')}{d\Omega'} = \left(\frac{\hbar\omega'}{m_e c^2}\right)^2 \frac{1}{\beta^2\gamma^2} \frac{d\sigma^{ph}(\pi - \theta')}{d\Omega'}. \tag{4.24}$$

(b) The transformation of emitted photon frequency, relativistic angle and solid angle from the projectile frame (primed quantities) to the laboratory system (un-

primed quantities) are given by [8]

$$\begin{aligned} \omega' &= \gamma\omega(1-\beta\cos\theta) \\ \cos\theta' &= \frac{\cos\theta-\beta}{1-\beta\cos\theta} \end{aligned} \tag{4.25}$$

hence

$$\frac{d\Omega'}{d\Omega} = \frac{1}{\gamma^2(1-\beta\cos\theta)^2}. \tag{4.26}$$

Finally, the angular distribution as a function of the angle θ in the laboratory frame of the electron is mediated by the Lorentz transformation

$$\frac{d\sigma^{RR}(\theta)}{d\Omega} = \frac{d\sigma^{RR}(\theta')}{d\Omega'}\frac{d\Omega'}{d\Omega}. \tag{4.27}$$

4.4.1 REC into the K-shell

Taking into account the retardation contained in the photon plane wave $e^{-i\mathbf{kr}}$ one could expect the following angular distribution in the projectile frame [167] (Fig. 4.8, top), as

$$\frac{d\sigma^{RR}(\theta')}{d\Omega'} \propto \frac{\sin^2\theta'}{(1+\beta\cos\theta')^4}. \tag{4.28}$$

Applying now the given transformation of all quantities into the laboratory system one finds the simple angular differential cross section dependence [165] (Fig. 4.8, bottom), that is

$$\frac{d\sigma^{RR}(\theta)}{d\Omega} \propto \sin^2\theta. \tag{4.29}$$

The polar angle dependent differential cross section shown in Fig. 4.8 corresponds exactly to that of the completely nonrelativistic dipole approach which results from neglecting the photon momentum ($\mathbf{kr} \ll 1$) as well as the fast electron velocity ($v \ll c$) [168]. This peculiar cancellation between the effects of the retardation, i.e. of higher multipoles (leading to the deviation from a $\sin^2\theta$ distribution) and the Lorentz transformation to the laboratory system, which occurs within the nonrelativistic approach applied for capture into the K-shell, was originally predicted by Spindler *et al.* [165]. In fact, these predictions were verified by Anholt *et al.* [169] experimentally for 197 MeV/u bare Xe^{54+} projectiles on Be atoms. All the experimental data fall onto the curve as predicted by the nonrelativistic dipole approximation based on Stobbe's treatment of the photoionization process, assuming nonrelativistic hydrogen-like wavefunctions for the $1s$ ground state. This good agreement found between the nonrelativistic dipole approximation and the correct relativistic description, for relatively light atomic systems and not too high energies, appears to be a general feature of all photon-electron interaction processes [170]. It can be explained in terms of an approximate cancellation among relativistic, retar-

dation, and multipole effects [171] which, however, only occurs for bound s-states and for total cross sections [172, 173].

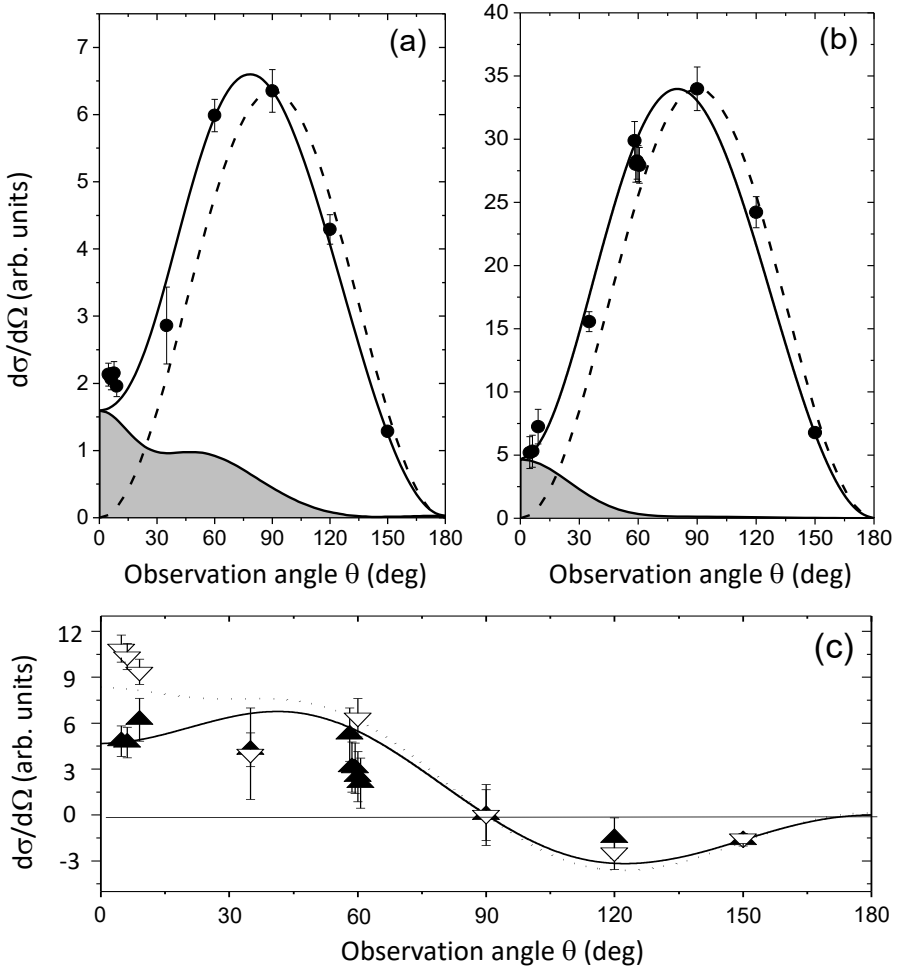

Figure 4.9: Top part: Experimental K-REC angular distribution [(a) 309.7 MeV/u [174]; (b) 88 MeV/u [175]] in comparison with complete relativistic calculations (solid lines) and the $\sin^2\theta$ distribution of the nonrelativistic theory (dashed lines). Bottom part:(c) Deviations from the $\sin^2\theta$ distribution [176]. Solid triangles: 88 MeV/u $U^{92+} \rightarrow N_2$; open triangles: 309.7 MeV/u $U^{92+} \rightarrow N_2$; solid and dashed lines: corresponding relativistic predictions.

For heavier systems and even higher energies and also for states with angular momentum $l \geq 0$ this cancellation is no longer valid [166, 167] as will be discussed in relativistic treatment. In Fig. 4.9 the angular distributions for K-REC into 309.7 MeV/u and 88 MeV/u bare uranium projectiles are plotted in the laboratory frame [174, 175]. The magnetic transitions, corresponding to a spin-flip of the electron during capture, contribute significantly in the forward directions. The shaded area shows the spin-flip contributions to the angular distribution. The nonrelativistic approach is given by the dashed line for comparison. Furthermore, the investigation of the beam-energy dependence of this effect was of additional interest. For this purpose, the deviations of the experimental data from the $\sin^2\theta$ distribution is illustrated in more detail at the bottom part of Fig. 4.9 where the difference $\Delta d\sigma/d\Omega$ is

plotted as a function of the observation angle. For comparison, the corresponding variances are given for the results of mediate collision energy at 88 MeV/u (solid triangles) and higher energy at 309.7 MeV/u (open triangles), respectively, while the solid and dashed curves refers to the corresponding complete relativistic theory. As can be observed in the figure, the data sets for both energies are indistinguishable within the error bars, except close to 0°. For angles larger than 60° the same holds true for the corresponding fully relativistic descriptions where only small energy dependent variations are observed.

In general, for the energy regime under consideration here, the deviations from the nonrelativistic approach appear to be a large amount energy insensitive, and are caused by the relativistic wavefunctions of the high-Z system. Only the spin-flip transitions appear to be strongly velocity dependent which are mediated by the magnetic field produced by the moving projectile (compare region close to 0° in Fig. 4.9). However, the strong variation of the angular distribution as a function of energy turns out to be rather unimportant at low energy regime even for nuclear charge up to $Z = 92$. In Fig. 4.10 the calculated differential cross sections for K-shell radiative recombination into bare uranium projectiles at relative electron-ion energy from 1 meV to 10 eV, which has to be compared with the ground-state ionization potential in H-like uranium of about 132 keV, are given as a function of the observation angle θ in the laboratory frame, and the distribution is normalized to the value at $\theta = 90°$. Here, indeed the occurrence of spin-flip transitions appears to be a tiny effect where almost no energy dependent variations are observed in terms of the general shape of K-RR emission pattern.

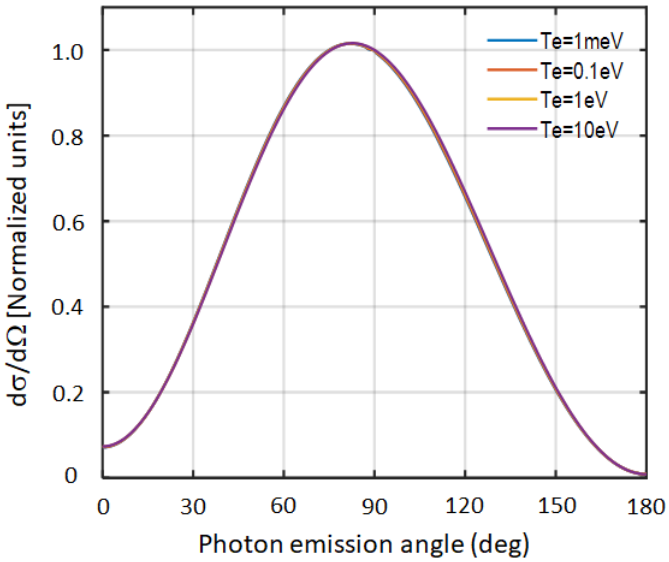

Figure 4.10: Angular distribution for RR into the K-shell of bare uranium as a function of the observation angle in the laboratory frame at various electron-ion relative energies. The differential cross sections of theoretical calculated data are normalized to the value at $\theta = 90°$.

4.4.2 REC into the L-shell sublevels

The photon angular distribution of the two fine-structure components ($j = 1/2$ and $j = 3/2$) for REC into the L-shell was investigated in detail at the heavy ion synchrotron SIS18 where 89 MeV/u He-like uranium projectiles colliding with carbon target atoms [172, 177]. This experiment represents the first subshell resolved L-REC photon angular distribution study and in particular the first investigation of the photon angular distribution for capture into a pure p-state as shown in Fig. 4.11. The data for the $j = 1/2$ level shows a considerable bending of the angular distribution into the forward direction, whereas the distribution for capture into the $j = 3/2$ state exhibits a slight enhancement at backward angles. This confirms in particular the prediction of the relativistic theory that the Lorentz transformation to the laboratory system is not sufficient to cancel for the $2p_{3/2}$ distribution the bending towards backward angles caused by retardation effect. Also, the $2s_{1/2}$ distribution deviates markedly from a $\sin^2\theta$ form. This distribution determines essentially the radiation pattern for capture into the $j = 1/2$ states at forward angles, and the distribution for the $2p_{1/2}$ level follows closely the form for REC into $2p_{3/2}$ state. The most remarkable aspect of the calculated distribution for the $2s_{1/2}$ state is that it predicts non-vanishing values at 180° and in particular at 0° observation angle. As has been pointed out in Refs. [151, 178], angular momentum conservation requires that cross sections in the forward or backward directions can only be attributed to spin-flip transitions which are not considered in a nonrelativistic theory.

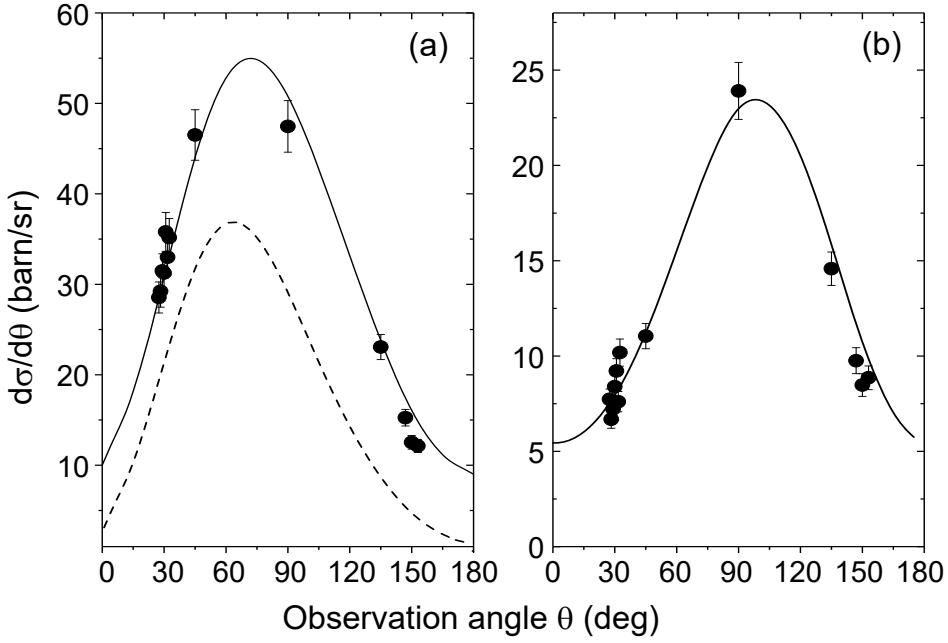

Figure 4.11: Experimental angular distribution of L-REC radiation for REC into (a) $j = 1/2$ and (b) $j = 3/2$ state observed in $U^{90+} \rightarrow C$ collisions at 89 MeV/u [177]. The solid lines give the results of exact relativistic calculations. In addition, the theoretical results for $2s_{1/2}$ [dashed line in (a)] is presented.

For RR processes in the merged-beam experiments using storage ring electron cooler devices, the projectiles collide with electron beam at transverse direction accompanied by the emission of photons at the directions of 4π. In the particular case of the RR process occurring in the electron cooler, the calculated RR rate coefficients at 90° are used to compare our results with the experimental data registered by the two x-ray detectors mounted at 0° and 180° along the ion-beam axis. Here, it is important to stress that the shape of the RR angular distribution remains essentially unchanged for the whole low-collision energy range defined by the temperatures of the electron beam in the electron cooler. For illustration, Fig. 4.12 shows the angular differential cross sections for RR into the L-shell sublevels of initially bare uranium ions, where electron-ion relative energies from 1 meV to 10 eV are displayed.

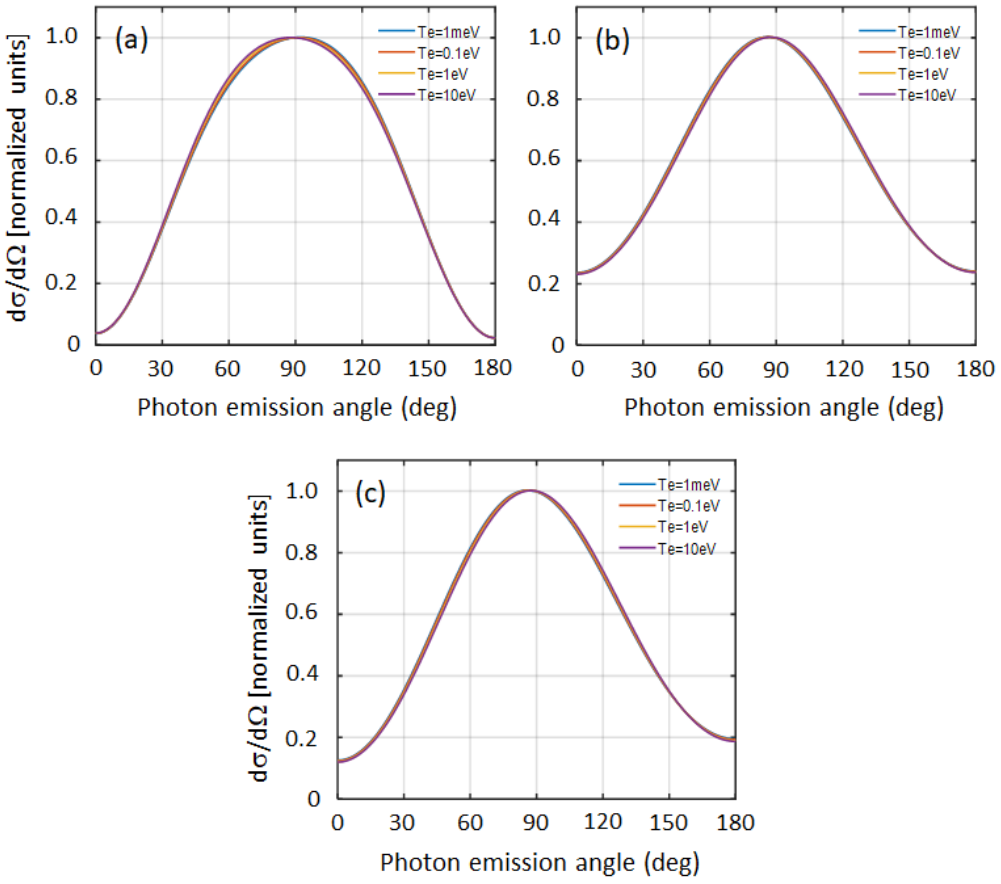

Figure 4.12: Angular distribution for RR into the L-shell sublevels of bare uranium as a function of the observation angle θ_{lab} at various electron-ion relative energies. (a): capture into $2s_{1/2}$; (b): capture into $2p_{1/2}$; (c): capture into $2p_{3/2}$. All calculated data are normalized to the value at $\theta_{lab} = 90°$.

4.4.3 De-excitation x-rays from REC

For electron capture into an excited state of the projectile, this state may decay by x-ray emission. In theory the angular distribution of these characteristic x-rays

with respect to the beam axis was studied extensively in Refs. [179, 180]. For the particular case of the $2p_{3/2}$ decays by $E1 + M2$ transition (see Fig. 3.5) to the ground state, investigations were performed with bare uranium projectiles at the gas-jet target of the ESR storage ring [121, 181], and the anisotropic emission in the emitter frame is simply given by [122]

$$W(\theta) \propto 1 + \beta_{20}(1 - \frac{3}{2}\sin^2\theta), \tag{4.30}$$

where θ denotes the angle between the direction of the emitted photon and the beam direction, and β_{20} gives the coefficient of the alignment which is related to the population cross section $\sigma(j, m_j)$ for the magnetic levels [152]

$$\beta_{20} = \frac{1}{2} \cdot \frac{\sigma(3/2, \pm 3/2) - \sigma(3/2, \pm 1/2)}{\sigma(3/2, \pm 3/2) + \sigma(3/2, \pm 1/2)}. \tag{4.31}$$

Consequently, by measuring the Lyα_1 emission at a few observation angles, the alignment of the $2p_{3/2}$ state and the relative population of the magnetic sublevels can be experimentally determined.

Based on expression Eq. 4.30, the theoretical and observed angular distributions were compared in detail as shown in Fig. 4.13 and a remarkable difference was found [179, 121]. The deviation was surprising also in the sense that REC is otherwise one of the best studied processes for high-Z, hydrogen-like ions for which an excellent agreement between theory and experiment is typically found. However, viewing the used rigorous relativistic calculations in more detail one finds that it is assumed that the level of interest, namely the $2p_{3/2}$ state, decays solely by an electric dipole transition. Whereas this assumption is for sure an excellent approach for the low-Z regime, at high-Z however, the magnetic quadrupole decay $M2$ may contribute in addition and may affect considerably the emission characteristics of the decay photons (angular distribution [182] and polarization [183]). As a result, the alignment coefficient parameter β_{20} must now be replaced by the product $\beta_{20} \cdot f(E1, M2)$ where $f(E1, M2)$ is the structure function which takes into account the $E1 - M2$ interference effect. This structure function is given by [180]

$$f(E1, M2) \propto 1 + 2\sqrt{3}\frac{\langle \| M2 \| \rangle}{\langle \| E1 \rangle \|}, \tag{4.32}$$

where $\langle \| E1 \| \rangle$ and $\langle \| M2 \| \rangle$ are the reduced matrix elements for the electric and the magnetic bound-bound multipole transitions, respectively [152].

For high-Z ions the ratio of the transiton amplitudes is of the order of ~ 0.1, leading to a 1% contribution of the $M2$ component to the total decay rate. Indeed, even for hydrogen-like uranium ($Z = 92$) the $M2$ transition rate contributes less than 1% to the total decay rate. Up to now this rather small contribution was the main justification why the $M2$ component of the radiation field has not been

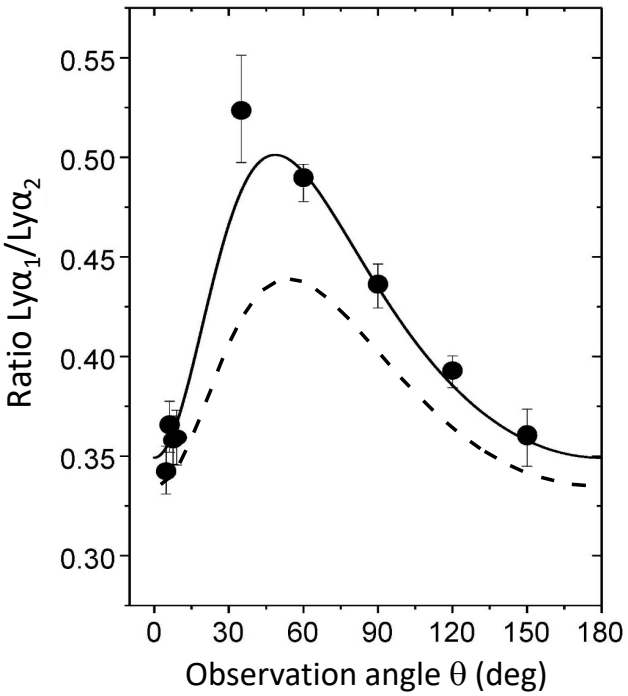

Figure 4.13: Measured angular distribution of the Lyman-α_1 radiation following the REC into initially bare uranium projectiles with a beam energy of 309 MeV/u [122]. Here, the Lyman-α_2 is isotropic in the projectile frame and used for normalization. The solid line refers to the least-squares adjustment of Eq. (4.30) to the experimental data, taking into account the correct relativistic angle and solid angle transformation. The solid line refers to the least-squares adjustment of Eq. 4.30 to the experimental data, considering the correct relativistic angle and solid angle transformation. The dashed line displays the theoretical results under the consideration of only electric dipole component, i. e. $\langle \| M2 \| \rangle \approx 0$ is taken to be negligible.

incorporated in computations on the $2p_{3/2}$ decay of hydrogen-like ions or similar ground state transitions in the high-Z regime. Figure 4.14 shows the structure function 4.32 for hydrogen-like ions as a function of the nuclear charge Z. Since the function $f(E1, M2)$ basically depends on the ratio $\langle \| M2 \| \rangle / \langle \| E1 \| \rangle$ of the reduced matrix elements, its scaling follows roughly a Z^2 dependence. For H-like uranium, this dimensionless function is as large as 1.28 [180]. As a consequence the interference leads to a non-negligible effect of a few percent even for medium-Z ions.

From the measured alignment in Refs. [121, 122] the $2p_{3/2}$ level follows that about 75% of the capture events populate the $|m_j| = 1/2$ sublevels of the $2p_{3/2}$ state. By subtracting the cascade contribution, it was possible to deduce that direct radiative capture into the $2p_{3/2}$ state populates the $|m_j| = 1/2$ magnetic sublevels by more than 90%. As a result, a significant alignment with negative anisotropy parameter β_{20} will contribute considerably the angular distribution for the decay photons. In the case of electron cooler devices, where radiative recombination at collision energies of a few meV prevails, recombination into high Rydberg states and following radiative cascades will contribute significantly to the intensity of the characteristic

radiation (see also Fig. 4.5 and Fig. 4.6). This will substantially attenuate any potential initial alignment of excited states produced via RR which finally populate the states of the L and M shells via radiative cascades. To be more specific, for case of the $2p_{3/2}$ state the population of magnetic sublevels will benefit from the cascade feeding of higher levels up to Rydberg state, and hence $\sigma(3/2, 3/2) \approx \sigma(3/2, 1/2)$. Therefore, in contrast to the prompt RR radiation, an isotropic emission pattern is expected in the projectile frame for the subsequent characteristic projectile transitions of the observed Lyman, Balmer, and Paschen series, which will be incorporated into the spectrum modeling as discussed in Chapter 5.

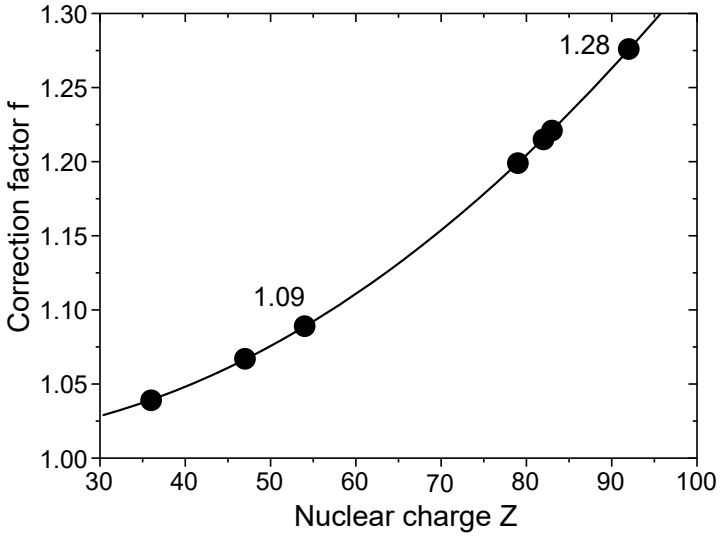

Figure 4.14: Structure factor $f(E1, M2)$ as calculated for the decay of the $2p_{3/2}$ state in hydrogen-like ions as a function of the nuclear charge Z. The dependence as a function of the nuclear charge Z is roughly reproduced by a Z^2 dependence [184].

Chapter 5

X-ray spectroscopy study for hydrogen-like lead ions at the electron cooler of CRYRING@ESR

In this chapter I will report on the first commissioning run experiment in May 2020, carried out at the electron cooler of CRYRING@ESR storage ring complex by utilizing the deceleration technique, to study the x-ray emission associated with radiative recombination of bare lead ions with free cooler electrons at zero relative electron-ion velocity (on average). For the experimental setup, two standard high-purity, planar germanium x-ray detectors were placed at exact 0° and 180° viewports, which makes the experiment insensitive to an uncertainty in the observation angle. For the x-ray emission pattern, experimental and theoretical studies are presented to investigate in detail the prevailing cascade decay dynamics and provide exhaustive insight into the final state population of the recombination process itself. From the observed characteristic projectile x-rays a significant contribution from radiative deexcitation cascades is deduced.

5.1 General considerations and experiment

The coupling of the ESR and the CRYRING@ESR storage ring complex [6, 185] serves as the platform for the experiment, since the CRYRING here can be used to perform experiments with cooled bare heavy ions, while the ESR prepares the next ion bunch. In the experiment, fully stripped Pb ions from UNILAC/SIS accelerator complex were injected into the ESR at a specific energy of 400 MeV/u. Usually, many beam pulses were stacked and accumulated in the ring, eventually $6 \sim 8 \times 10^7$ Pb^{82+} ions can be stored by this technique. However, this number is still below the

upper limit of particles which can be installed in principle. The basic restriction is due to the space charge potential of the stored ion beams and limit the number of stored ions.

The stored ions can be very efficiently cooled by Coulomb interaction with the cold co-moving electrons [32], then decelerated down to 10 MeV/u, electron cooling and storing takes place. Thereafter, the ions were injected into CRYRING. At CRYRING electron cooling was applied again to guarantee a well-defined constant beam velocity which was generally of the order of $\Delta\beta/\beta \sim 10^{-5}$. For this purpose electron currents of typically 10 to 20 mA were applied. Moreover, the electron cooling provides a small beam size with a typical diameter of 2 mm, a reduced relative momentum spread $\Delta p/p \sim 10^{-5}$, as well as an emittance of the ion beam of less than 0.1π mm mrad. Here, it is important to note that both the transverse emittance and the relative momentum spread of the stored beam depend on the number of stored ions and the applied cooler current [186].

The experimental setup for the measurement of x-ray radiation at the electron cooler device is shown in Fig. 5.1. At the electron cooler dedicated vacuum separation chambers were used [187]. For the forward (0° with respect to the ion beam axis) and backward (180° with respect to the ion beam axis) direction, the detectors were installed behind a 100 μm thick beryllium window mounted on a CF 100 flansh to allow for the transition of low-energy x-rays while maintaining the ring vacuum of typically 10^{-11} mbar. The detector geometry itself was precisely determined by laser assisted trigonometry. The x-ray detection was accomplished by two high-purity, planar germanium x-ray detectors, which were mounted 3.5 m at 0° and 3.3 m at 180° with regard to the midpoint of roughly 1.2 m long straight electron cooler section. The detector at 0° had a crystal diameter of 16 mm (crystal thickness 10 mm) and was equipped with an x-ray collimator (10 mm thick, made out of brass and reducing the effective detector area to 79 mm^2). This results in a solid angle coverage of $\Delta\Omega/\Omega$ which varies along the cooler section from about 6.3×10^{-7} to 1.3×10^{-6}, respectively. At 180° the detector used had a diameter of 49.7 mm (crystal thickness 21 mm) and was equipped with an x-ray collimator (10 mm thick, made out of brass and reducing the effective detector area to 962 mm^2). As a consequence, there $\Delta\Omega/\Omega$ varies along the cooler section ranging from 1.0×10^{-5} to 4.9×10^{-6}, respectively. In addition, due to the relativistic solid angle transformation [166], the effective solid angle at 0° observation angle for photons being emitted in the rest frame of the ions is enhanced relative to the one at 180° by a factor of 1.8. In order to suppress the dominant background, stemming from x-ray emission by the electron beam (bremsstrahlung inside the upper part of the electron cooler) and the natural background, an ion detector based on secondary electron detection (channel electron multiplier) [188] was successfully operated downstream to the cooler (ion detector for down-charged Pb^{81+} ions). The coincidences between

both the registration of x-rays from the interaction region of the electron cooler and the down-charged ions allowed for the unambiguous identification of those x-rays associated with radiative recombination events.

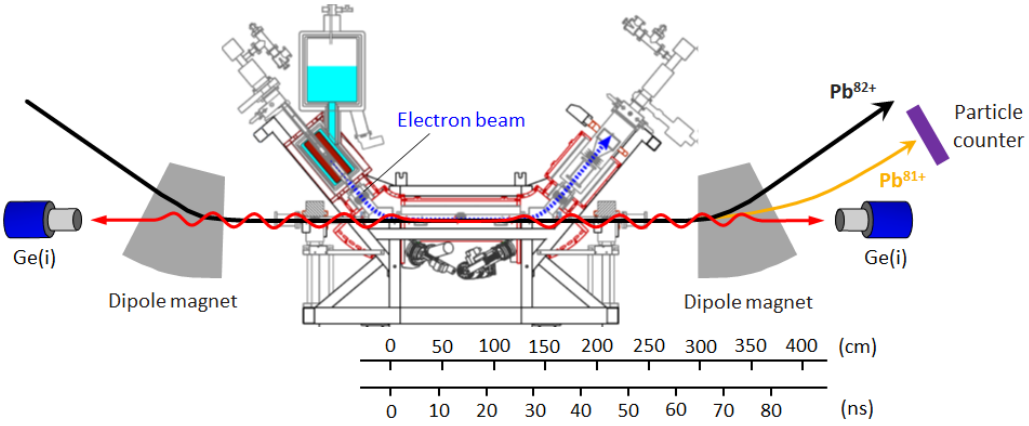

Figure 5.1: Experimental setup at the CRYRING@ESR electron cooler. The electron-ion beam interaction region is viewed by 0° and 180° Ge(i) x-ray detectors. X-rays are measured in coincidence with down-charged Pb^{81+} projectiles detected by the particle counter installed behind the electron cooler. A length scale and a time scale, valid for a beam velocity of $\beta = v/c \approx 0.146$ (10 MeV/u), are shown at the bottom. Note, the time of flight of the ions passing the cooler section is close to 30 ns whereas the time of flight of ions from the entrance of the cooler section up to the end of the straight section amounts to 70 ns.

In the present experimental situation where recombination of bare lead ions with free electrons at zero relative electron-ion velocity, high Rydberg states of the ions are expected to be populated [15, 16, 17, 18]. The ions in these highly excited levels might be re-ionized on their way to the particle detector when exposed to electromagnetic field of the next dipole magnet of CRYRING@ESR. The highest n_{dip} state that survives field ionization, defined by the dipole magnets setting at the storage ring [189], is usually estimated by the formula [156, 190]

$$n_{dip} = \left(6.2 \times 10^{10} q^3 / v_i B\right)^{1/4}. \tag{5.1}$$

Where q is the charge state, v_i the ion beam velocity, and B the magnetic field strength in the unit of tesla. In this experiment, the n_{dip} is estimated to be 165 corresponding to the magnetic rigidity value of 1.17 Tm of the dipole magnet. One also note that the rather sophisticated and detailed studies on the re-ionization of high excited states in magnetic fields have been reported [191, 192, 193], pointing out the relevance of Rydberg states with even higher main quantum number n than the one defined in Eq. 5.1, but with low orbital quantum number l, which are not field ionized and thus could still contribute to the observed rate in the particle detector. Indeed even in our current experiment related cascade transitions could be possible during fight time of ions to the dipole magnet. However, as discussed

before these states are not significantly populated via RR (e.g. see Fig. 4.5 in Sec. 4.3.2) and will be neglected in the following.

Among possible recombination mechanisms of radiative recombination and three-body recombination for bare projectiles, three-body recombination processes in the cooler lead to population of states with binding energies comparable to the electron beam temperature [140, 194] of a few meV. For H-like lead ions, this corresponds to Rydberg state with $n \approx 4000$. Since this value is far beyond n_{dip} and the corresponding radiative lifetime is orders of magnitude larger than the flight time of ions from the center of cooling section to the dipole magnet, the three-body recombination processes will hardly contribute to the observed x-ray intensities [15].

Even though in this very first beam time with bare, decelerated lead ions in CRYRING@ESR only a low intensity of 2×10^5 ions per injection was possible, a few days of continuous operation were sufficient to accumulate meaningful spectral information when combining the signals in both x-ray detectors with the particle detector. Here, the experimental study benefited from the deceleration technique [195] established, for decelerated ions the bremsstrahlung intensity caused by the cooler electrons was strongly reduced due to the comparably small cooler voltage of about 5.5 kV and current of 12 mA. Consequently, very clean conditions for x-ray spectroscopy were present at the cooler section. In this chapter, the transverse temperature of the electron beam used in the CRYRING@ESR electron cooler is $kT_\perp = 2.59$ meV (in energy units), which corresponds to the cathode temperature. For the longitudinal electron motion, $kT_\parallel = 51.8$ μeV is inferred from the analysis of resonance shapes in dielectronic-recombination (DR) measurements with lithium-like Ne^{7+} ions [164]. Moreover, the investigations at the CRYRING@ESR electron cooler profit from the 0° and 180° geometry of x-ray detector setup, which leads to the almost eliminated Doppler broadening, and makes the experiment insensitive to an uncertainty in the observation angle. The result is depicted in Fig. 5.2 where the coincident x-ray spectra are plotted as observed for initially bare lead ions at an energy of 10 MeV/u , the x-ray energies in Pb^{81+} spectra were precisely measured with the Ge(i) detectors at 0° and 180° exploiting closely spaced γ-lines of known energies from standard radioactive calibration sources of ^{241}Am, ^{133}Ba, and ^{57}Co, regularly placed in front of the x-ray detectors during the beam time.

In contrast to the ESR where the x-ray detectors view the cooler section via thin stainless steel foils at observation angles of close to 0.5° and 179.5° with respect to the ion beam axis [18, 19], the detectors at the CRYRING@ESR can be placed exactly at 0° and 180° observation geometry. In Fig. 5.2, the low bremsstrahlung intensity together with high transmission of photons due to 100 μm thick beryllium windows installed allowed us for the first time to observe Balmer and Paschen series, located at the low-energy part of the spectra. Most importantly, distinctive tails of Lyman-α transition lines observed at the ESR [18, 22, 196], caused by delayed

cascade feeding of the L-shell sublevels, were consequently not present in the case of the CRYRING@ESR electron cooler. All these proof of the favorable conditions enable planned state-selective x-ray spectroscopy study.

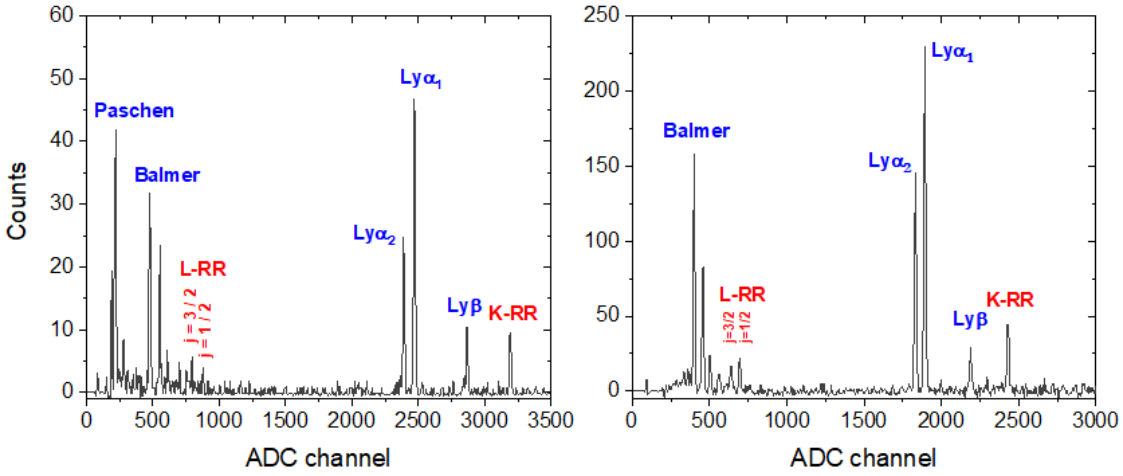

Figure 5.2: X-ray spectra of H-like Pb^{81+} measured by two Ge(i) detectors in coincidence with 10 MeV/u Pb^{82+} projectiles capturing free electrons. The spectra were taken at the CRYRING electron cooler at observation angles of 0° (left) and 180° (right), respectively.

5.2 The experimental challenges

It has proven very useful to start with a bare ion to which a single electron is added in a recombination process in the electron cooler or in a single electron capture event in the gas-jet target. The subsequently emitted x-rays are measured in coincidence with those ions that have lost one unit of charge during the interaction with the target and which are deflected out of the main ion stream in the following dipole magnet of the storage ring. For an accurate determination of the photon energy in the projectile frame of reference, the Doppler effect remains as one of the most serious difficulties in which an accurate knowledge of both the ion velocity and the observation angles are required. At an ion beam velocity of 10 MeV/u there is a factor of 1.3 variation in the laboratory x-ray energy going from forward ($\theta = 0°$) to backward ($\theta = 180°$) observation.

5.2.1 Doppler effect

It turns out that a large fraction (exceeding 50%) of the stored inventory of bare ions in the storage ring can be converted into x-rays useful for spectroscopy study. Here, The radiation emitted by ions moving with relativistic velocities is affected by the Doppler effect which introduces a difference in the transition energies between the emitter and observer frames (Doppler Shift) and between transitions observed at

different angles (Doppler Broadening). Therefore photon energies measured in the laboratory system have to be corrected for the relativistic Doppler shift according to the Lorentz transformation

$$E_{proj} = E_{lab} \cdot \gamma \cdot (1 - \beta \cdot \cos\theta_{lab}) \,, \tag{5.2}$$

where E_{proj} and E_{lab} denote the x-ray energy in the projectile and laboratory frames of reference respectively and β and γ are the usual relativistic parameters whereas θ_{lab} is the observation angle relative to the ion-beam direction.

In upper part of Fig. 5.3 the ratio E_{lab}/E_{proj} is plotted as a function of observation angle θ_{lab} for the ion beam energies of 10 MeV/u and 68 MeV/u, respectively. For x-ray detectors placed at 0° and 180° observation angles relative to the ion beam axis, the measurement of photon energies is insensitive to misalignment of the observation angles, i.e. the uncertainties introduced by angular uncertainties vanish at 0° and 180°, hence independent of ion beam velocity as indicated in the figure.

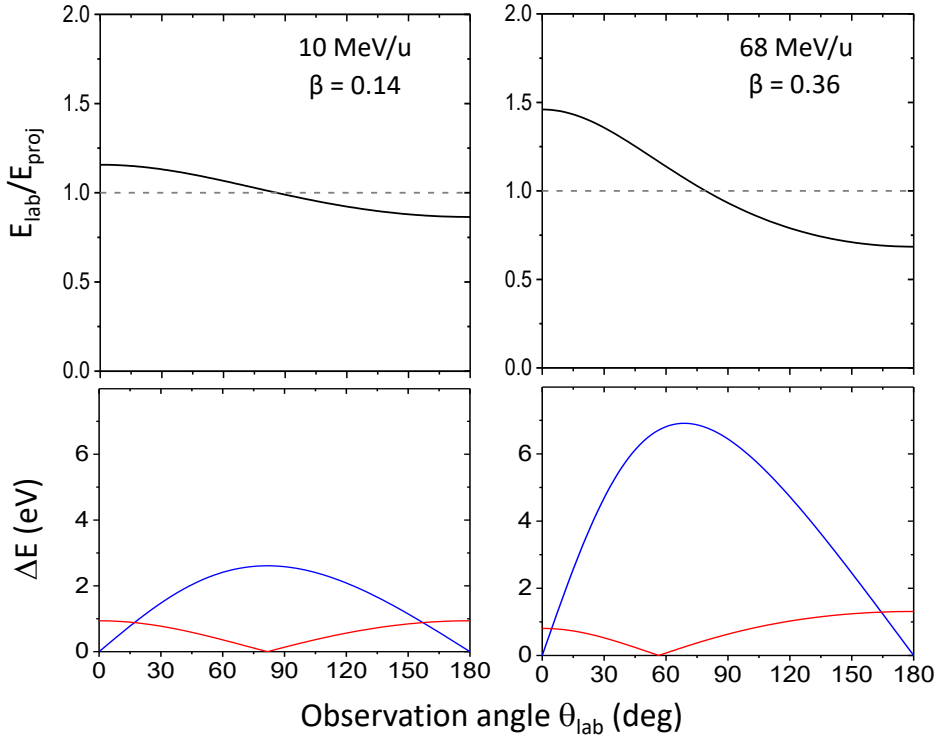

Figure 5.3: Upper part: Relativistic transformation of the transition energy from the projectile frame, moving with a reduced velocity of $\beta \approx 0.14$ at 10 MeV/u and $\beta \approx 0.36$ at 68 MeV/u respectively, to the laboratory frame as a function of the observation angle. Lower part: Doppler broadening for the transition energy in the projectile frame as calculated from Eq. 5.3. Blue curves represent the uncertainty from $\Delta\theta_{lab} = 0.01°$, and red curves show the uncertainty from $\Delta\beta = 9 \times 10^{-6}$.

Although the brilliant, monochromatic beams of the CRYRING@ESR storage ring complex provide unique experimental conditions for x-ray spectroscopy of prompt RR radiations together with subsequent projectile x-rays, the main problem encoun-

tered is still the uncertainty introduced by the Doppler corrections, i.e. the Doppler shift and the Doppler Broadening. The final uncertainty of the x-ray energy in the projectile frame is determined by the uncertainties in the absolute value of β and of the observation angle θ_{lab}. The influence of the latter uncertainties on the final result, however, depend critically on the beam velocity and the observation angle chosen. This can easily be seen from the first order estimation of these uncertainties by differentiation of Eq. 5.2, as

$$\left(\frac{\Delta E}{E}\right)^2 = \left(\frac{\beta \cdot \sin\theta_{lab}}{1-\beta\cdot\cos\theta_{lab}}\Delta\theta_{lab}\right)^2 + \left(\gamma^2\frac{\cos\theta_{lab}-\beta}{1-\beta\cdot\cos\theta_{lab}}\Delta\beta\right)^2 + \left(\frac{\Delta E_{lab}}{E_{lab}}\right)^2. \quad (5.3)$$

The term containing $\Delta\theta_{lab}$ and $\Delta\beta$, respectively, are strongly dependent on the observation angle and are much reduced with decelerated ions, as shown in the lower part of Fig. 5.3.

For completeness it is important to note that $\Delta\theta_{lab}$ and $\Delta\beta$ can also be interpreted as width. In Eq. 5.3, due to the $\sin\theta_{lab}$ term, the uncertainty in $\Delta\theta_{lab}$ does not affect the final result at observation angles of 0° and 180°. Here, however, the error due to $\Delta\beta$ is largest. Conversely, for side-on observation near $\cos\theta_{lab} = \beta$ velocity uncertainties become unimportant but angular uncertainties are crucial. In practice a velocity-sensitive measurement near zero degree was realized at the electron cooler and an angular-sensitive geometry was realized at the gas-jet target. In this way absolute observation angles are either not critical or they are spectroscopically determined by using several detectors viewing the same x-ray source simultaneously.

5.2.2 Electron capture experiment at the electron cooler versus at the gas-jet target

Both the gas-jet target and the electron cooler can be applied for an intense production of prompt RR radiation in combination with subsequent characteristic projectile x-rays of the circulating high-Z ions. For a storage ring employing electron cooling it might be the most important loss mechanism. However, each ion which looses a unit of charge will emit one or more photons useful for precision spectroscopy. The situation is explained in detail in literature (see [8] and references therein). The cooling electrons are situated just at near zero energy as guaranteed by the drag force between electrons and ions [32] balancing the mean ion and electron velocity in the laboratory system. The very narrow energy distribution due to the low electron temperature of < 0.5 eV [22, 23] is small compared to the experimental uncertainties.

The strongest transition in the recombination process is the one into the $1s_{1/2}$ ground state where the photon energy is just the $1s_{1/2}$ ground-state binding energy. The prominent lines observed can be attributed to the direct transition of cooling

electrons into the K shell of the projectile and to the characteristic $nl \rightarrow 1s$ transitions. The latter are also induced by capture into higher shells and subsequent cascade transitions. For the RR process at electron cooler devices, the rate coefficient α_{nl} decreases approximately with the principal quantum number as $1/n$ [142] for inner shells. For calculating the cascade contribution, one has to sum over all the (n, l) states up to a maximum n_{dip} beyond which the electrons become reionized by transverse magnetic fields in the cooler [15].

At the gas-jet target, capture of bound target electrons into the fast moving, bare projectiles populates also excited levels of H-like ions which will finally cause the emission of characteristic x-ray photons. Although radiative recombination (RR) and radiative electron capture (REC) lead directly to photon emission (time reversed photoelectric effect) where for REC the relative motion of the quasifree target electrons with respect to the projectile ions has to be added in the energy balance, i.e. photon emission carries the excess energy and momentum from neutral gas target. Thus the information provided by the x-ray energy of the two dominant recombination and capture processes can easily be demonstrated in the following formulas:

$$\begin{aligned} E_{x-ray} &= E_e + E_B \text{ (RR)} \\ E_{x-ray} &= E_e + E_B - E_T \text{ (REC)} \end{aligned} \tag{5.4}$$

where E_B and E_T denotes the final (ion) and initial (target) binding energy of the active electron, and E_e its relative kinetic energy towards the projectile ion.

For x-ray measurements at the electron target (see Fig. 5.1) one has to use observation angles of 0° or 180° due to the geometrical restrictions at the cooler section. As can be read from the graph in Fig. 5.3 at 0° and 180° $\Delta\theta$ contributes practically nothing to the error, whereas $\Delta\beta$ is maximal. Therefore, β has to be known with high precision. On the other hand, for the case of 358 MeV/u ions at the gas-jet target an observation angle around 48° $\Delta\beta$ contributes minimal and $\Delta\theta$ maximal to the uncertainty ΔE in Eq. 5.3. For this purpose, the redundant information from segmented solid state x-ray detectors [84, 197] were used to improve the accuracy of the x-ray energy determination, as illustrated by the experimental arrangement depicted in Fig. 5.4. Here, one of these 48° detectors is a conventional solid state detector equipped with an x-ray collimator in order to confine the angular acceptance, thus reducing the Doppler broadening. The other detector consists of seven equidistant, parallel segments each furnished with a separate readout. They deliver seven independent x-ray spectra. The resulting sum spectrum combines the advantage of the large solid angle with a narrow Doppler width of one segment.

In RR, the target electrons are assumed to be at rest. In this case, one has a well-defined photon energy for a given collision system at each observation angle. In other words, the photon spectrum at each angle is given by a delta-function. Any

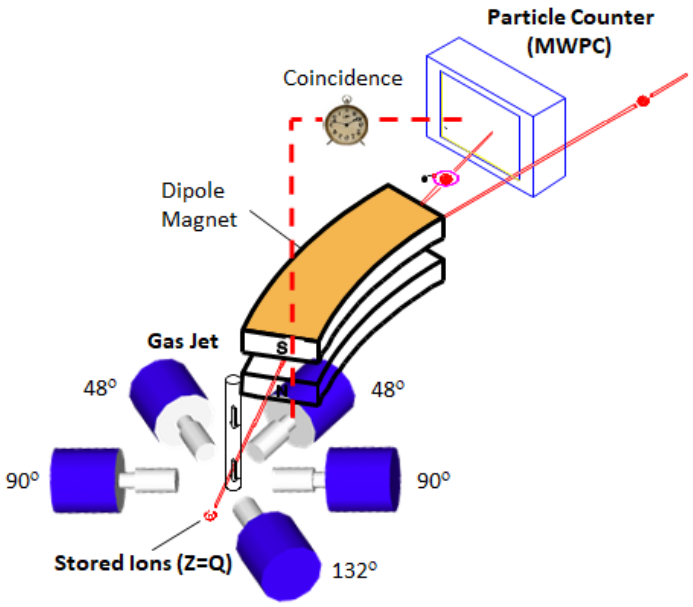

Figure 5.4: Experimental arrangement for the x-ray measurements at the gas-jet target (figure adapted from [198]). The spectroscopic information are registered by the high granularity Ge(i) detectors with several segments mounted at various observation angles [114].

momentum distribution will lead to a broadening of the photon spectrum. At the gas-jet target, the line width of the observed REC peaks increases about linearly with beam velocity. This increase is a combined result of an increase in Compton width proportional to the projectile momentum [199] and increasing Doppler width which is the dominant contribution for the large opening angles [114] in the setup used there. Certainly, distortion effects by the target charge number cannot be ignored in this case. Indeed, the shape of the photon spectrum in the projectile frame can be described by the well known formula [167, 200]

$$\hbar\omega = E_B - \gamma E_T + m_e c^2(\gamma - 1) - \gamma v q_Z, \tag{5.5}$$

where $m_e c^2(\gamma - 1) = E_e$ refers to the kinetic energy of the electron. In this equation, the effect of the Compton profile enters via the longitudinal target electron momentum q_Z. Since in this formula the target electron momentum is multiplied with the collision velocity v, a reduced REC line broadening due the Compton profile results for low beam energies.

5.2.3 Potential of deceleration capabilities

At the gas-jet target for low collision energy, REC is no longer the predominant capture mechanism. Here, Coulomb or non-radiative electron capture (NRC) (for details, see Ref. [201]) contributes largely to the charge exchange. While REC dominantly populates the $1s$ ground state of the projectile and, with decreasing

probability, higher projectile shells, NRC populates preferentially higher projectile states. The potential of the deceleration capabilities of the ESR, as an example, is demonstrated by the spectra of H-like uranium shown in Fig. 5.5 [114]. Compared to the high beam energies of 220 and 358 MeV/u, the x-ray spectra recorded for the decelerated ion beams of 49 and 68 MeV/u provide an abundant yield of various characteristic projectile transitions. Due to the larger NRC contributions at low projectile velocities (see Fig. 1 in Ref. [8]) the emission of characteristic x-rays following electron capture is a lot more efficient than at higher energies, where REC to the ground state prevails.

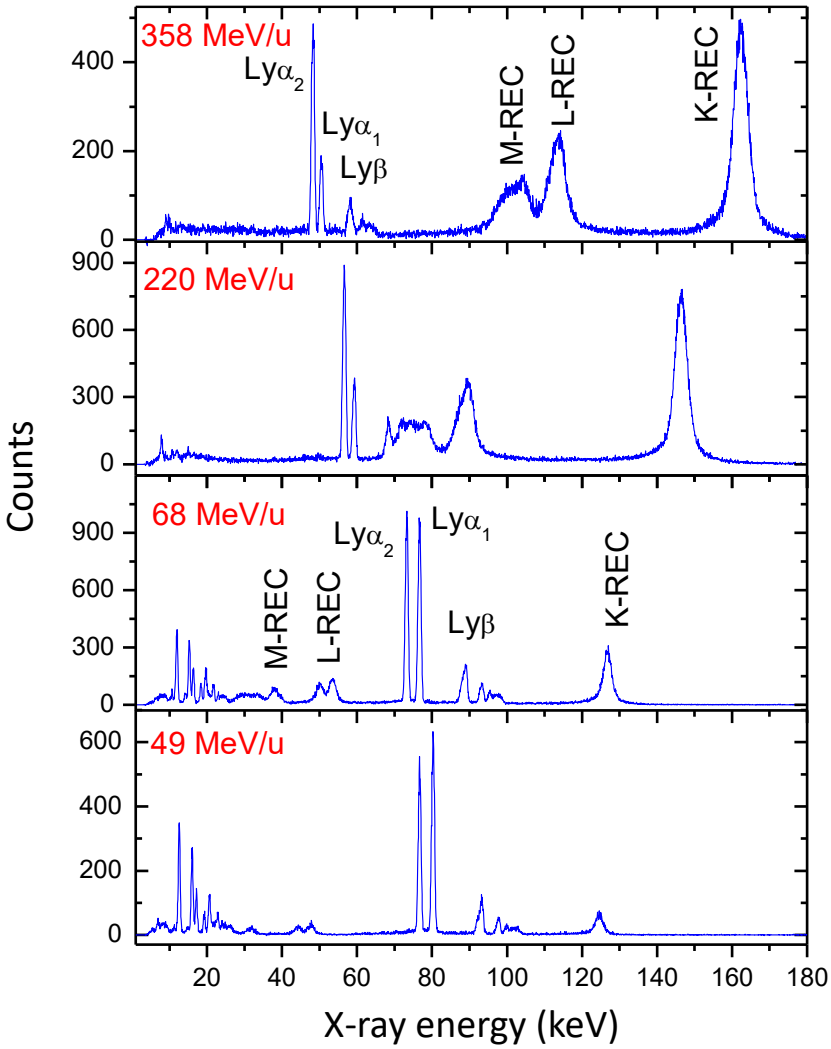

Figure 5.5: X-ray spectra registered in coincidence with the particle counter for 49, 68, 220 and 358 MeV/u U^{92+} interacting with N_2 targets in the laboratory frame [114]. The spectra were measured at the observation angle of 132°.

Again the relative low collision velocity leads to a strong reduction of the Doppler broadening as well as of the width of the REC lines which is caused by the Compton profile of the target electrons (see Eq. 5.5). As a result, the spectrum shows a well-resolved Balmer spectrum and also the direct capture into the L-shell sublevels

$j = 1/2$ and $j = 3/2$. This is in particular also true for the RR process whereby for decelerated ions the Bremsstrahlung intensity caused by the cooler electrons is strongly reduced due to the comparably small cooler voltage and electric current. Consequently, very clean conditions for x-ray spectroscopy are present at the cooler section which is already depicted in Fig. 5.2. Here in the electron cooler the cooling electrons and the ions are moving with approximately the same velocity resulting in collision energies close to 0 eV, the line width of the prompt RR transitions appears now comparable to the width of the characteristic projectile x-rays. Also, at such low relative energies, all uncertainties associated with Doppler corrections are strongly reduced compared to charge transfer in collisions of highly charged ions with neutral target atoms.

In RR process free electrons captured to the excited states of the projectiles will decay in the end to the ground state by the emission of characteristic x-ray lines. Figure 5.6 illustrates the de-excitation scheme for highly excited states up to $n = 100$, for instance, as produced by RR at low collision velocities that benefits from the established deceleration technique. States having a high principal quantum number n but a low angular momentum l will decay directly to the L-shell via fast electric dipole transitions. States having not only a high n but also a high l will decay step by step to lower lying levels until a transition into the K-shell occurs. For more details about the substate differentiation for the various shells, the spectrum simulation for a state-selective investigation of RR at electron cooling conditions is in comparison with the observed characteristic Lyman, Balmer and even Paschen radiations, as discussed in Sec. 5.4.

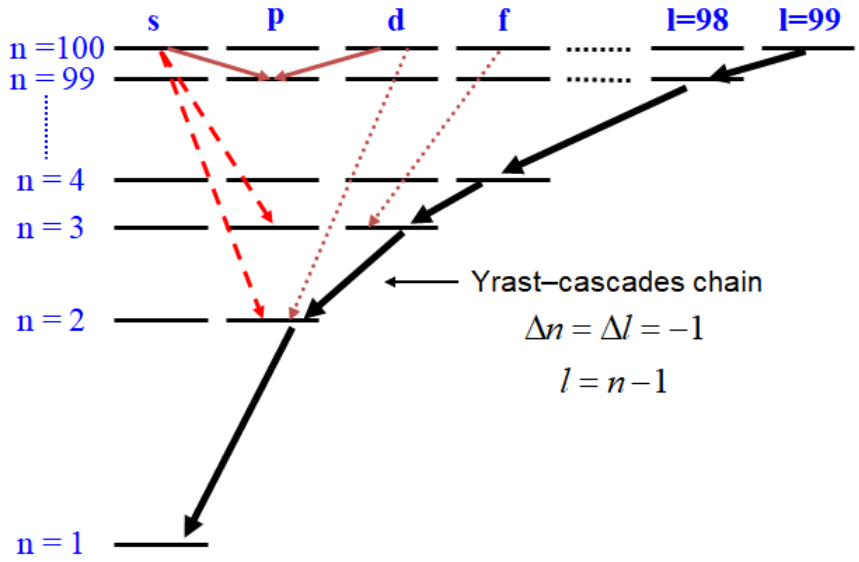

Figure 5.6: A schematic picture of the de-excitation cascade into the L-shell. Highly excited states with low angular momentum can decay via direct transitions. Due to the selection rule $\Delta l = -1$ states having high angular momentum will decay mainly via the so-called Yrast-cascades chain from state $n \rightarrow n-1 \rightarrow n-2$, etc.

5.3 X-ray spectra

In the experiment, bare lead projectiles were stored in the CRYRING@ESR storage ring at GSI at specific energies near 10 MeV/u and x-rays emitted from the 1.2-m-long cooling section were measured in delayed coincidence with particles that have lost one unit of charge by capture of a cooling electron. The x-rays were measured with intrinsic Ge(i) germanium detectors located 3.5 m along the midpoint of the cooler section in exact 0° and 180° geometry where angular uncertainties are not critical. Here, the interpretation and identification of such a radiative recombination x-ray spectrum via accurate modelling gives direct information on the energy levels and final state population of the resulting hydrogen-like system. Thus, the necessity of absolute measurements of x-rays yields by intrinsic germanium detectors has created the demand for determining the relative detection efficiency. Also, due to the favorable experimental conditions at the ring, i.e. observation of x-rays at exact 0° and 180°, well defined velocity of stored ions, and tuning the projectile velocity so that the x-rays appear close to calibration lines from γ-ray sources, the spectra energies of which have been determined on a absolute scale with high accuracy.

5.3.1 Calibration of the energy scale of x-ray spectra

The desired property of the solid state semiconductor detectors is that the channel number of photopeak is approximately proportional to the energy of the x-rays. The scaling factor is controlled by the amplified gain. If one assume an exact linear relationship between channel number and energy, we have

$$E = aC, \tag{5.6}$$

where E is the energy of the x-rays and C is the channel number of the center of the photopeak. The constant a is a scaling factor with units of energy/(channel number). To determine the scaling factor a, one need a source that produces a gamma particle with a known energy. By measuring the channel number of this gamma, the constant a can be determined. Once a is known, the energies of unknown x-rays can be determined from the channel number of the photopeak C.

In practice, one usually use more than one standard source for the energy calibration of the detector. The channel numbers of three or four gamma particles of known energies are measured. Then a best fit line, through these standard data points, is used as a calibration line. The calibration line might not pass through the origin, since the detector system would have an offset.

Using Gaussian curve fitting, one is able to measure the channel number of the center of the photopeak, C_0, really precisely. Using our 4100 channel detector system, high purity germanium, C_0 can be measured to within 0.01 channel number.

With this accuracy, deviations from the simple linear relation between E and C can be observed. One could choose a quadratic fitting function $E = aC + bC^2 + c$ or a higher order polynomial fit. However, the gain of the amplifier used in the laboratory can vary in time. After turning on the amplifier and power supply, one should wait for the electronics to "warm up". The drift in amplifier gain is often related to the quality of the amplifier/power supply system, hence is important for accurate energy determination. Adopting Gaussian curve fitting, one can observe the center of the photopeaks drift in time.

For the purpose of accuracy, it is the experience that the best approach is to use a linear fitting form and to adjust for the drift in the amplifier gain. To compensate for amplifier drift, one can use the calibration sources before and after a measurement. By taking an appropriate average of the center of the calibration photopeak, one can improve the accuracy of the energy determination significantly.

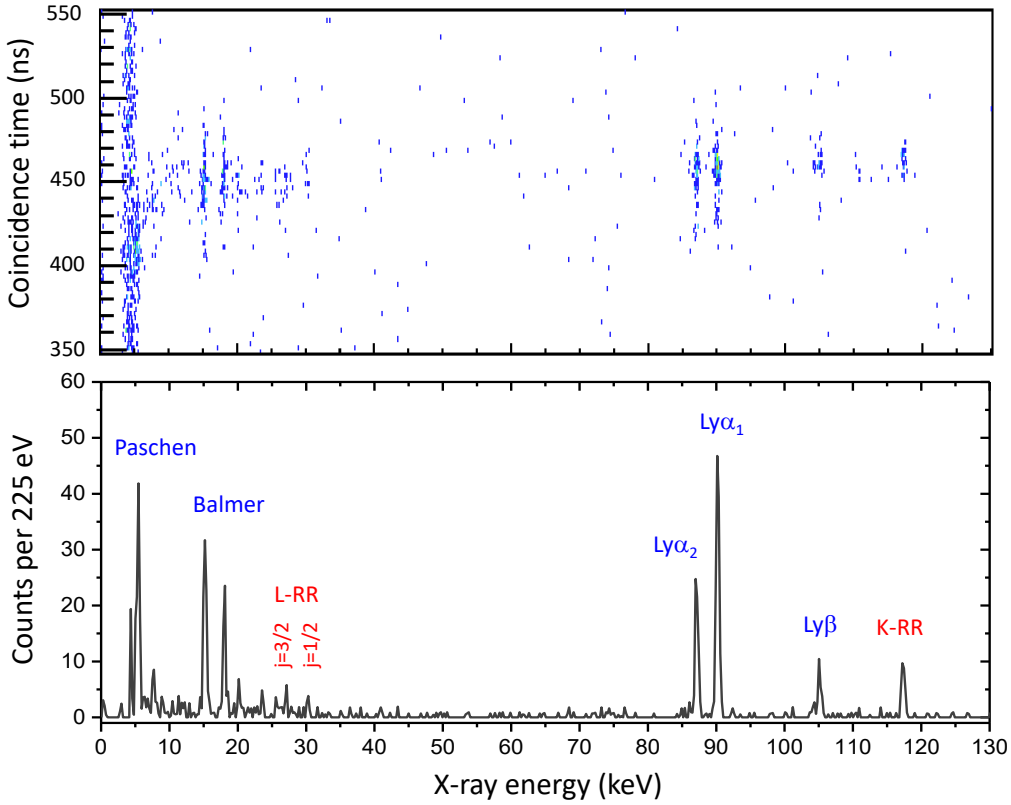

Figure 5.7: Top part: two dimensional scatter plot of the observed x-ray emission versus the coincidence time (without background subtraction applied). Bottom part: x-ray spectroscopy in the low energy region registered in coincidence with the particle counter at the observation angle of 0°. The energies of x-rays are determined from the ADC channel number in the laboratory frame.

Despite their overall non-linearity between channel number and energy, high purity Ge(i) detectors can be used to obtain energy differences with high precision. In the current experiment, x-ray energies were precisely measured relative to closely spaced γ-ray lines, the energies of which have previously been determined on an

absolute scale with high accuracy [71]. Only small energy differences were involved by Doppler tuning the interesting lines to overlap with suitable γ-ray lines originating from ^{241}Am, ^{133}Ba and ^{57}Co isotopes. As the influences from Doppler broadening and electron temperature are both small, the lines from prompt RR radiation and characteristic x-rays in H-like lead have almost the same width, determined by detector intrinsic resolution, as the calibration lines. The lines were fitted with Gaussian profiles for determination of the line positions. As a result, the x-ray energies in Pb^{81+} spectra registered by the two Ge(i) detectors at both 0°and 180° observation angles were determined. The resulting two dimensional presentation of the coincidence time versus the photon emission together with x-ray spectra measured at observation angles of 0° and 180° are displayed in Fig. 5.7 and Fig. 5.8.

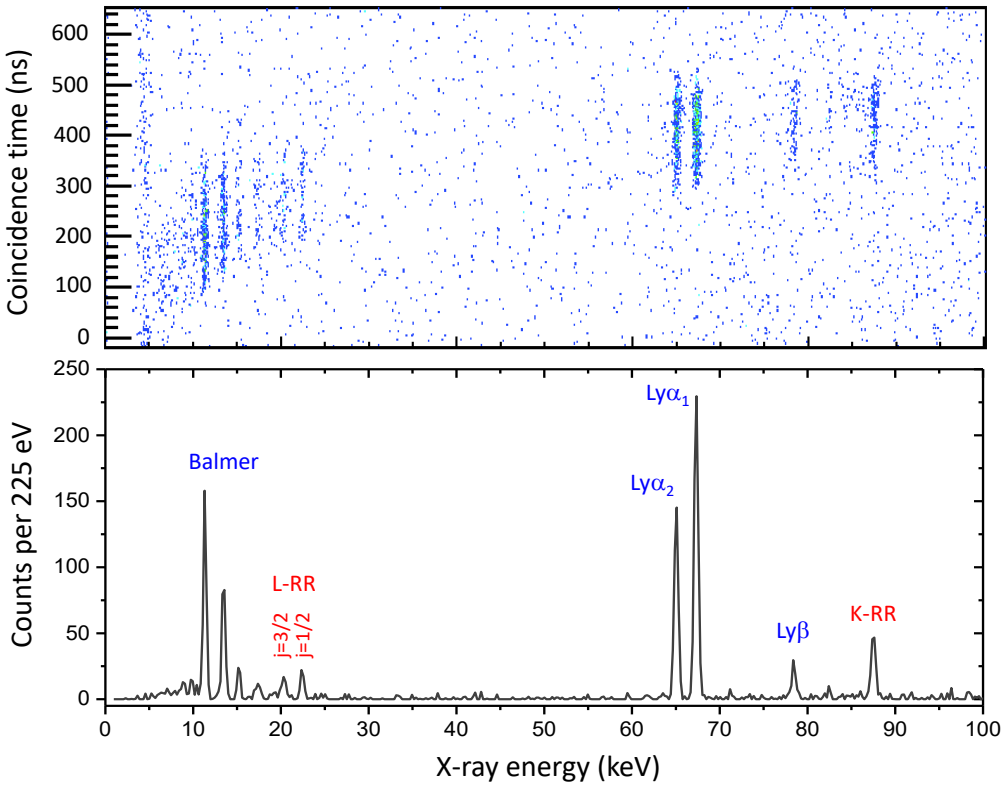

Figure 5.8: Top part: two dimensional scatter plot of the observed x-ray emission versus the coincidence time (without background subtraction applied). Bottom part: x-ray spectroscopy in the high energy region registered in coincidence with the particle counter at the observation angle of 180°. The energies of x-rays are determined from the ADC channel number in the laboratory frame.

5.3.2 Radiative cascade calculations

The x-ray spectra from H-like lead contain physical information such as a dominant decay pass and time-dependent populations in each upper state, thus the analysis of radiative cascade decay processes from a highly excited atomic system is important

to explain the observed x-ray spectroscopy for the current ion-electron recombination experiment, the situation is explained by the level scheme sketched in the upper part of Fig. 5.9. The population for excited states as a result of decay transitions can be obtained by solving a coupled rate equation and be used not only to construct a feature of spectra observed but also to make a cascade decay model for the system under consideration. If accurate rates for all transitions related to the decay streams as well as the initial population for the system under consideration are known, the time dependent population can be well estimated for all levels.

The population $N_k(t)$ at time t for the k state in each decay step can be obtained by solving a coupled rate equation written as [202]

$$\frac{dN_k(t)}{dt} = -\alpha_k N_k(t) + \sum_{m(>k)} \Gamma_{m\to k} N_m(t), \tag{5.7}$$

where α_k is a decay constant (the inverse of the lifetime) for the k state and $\Gamma_{m\to k}$ is a transition rate for the transition from an upper m state to a lower k state. α_k is a sum of transition rates for all transitions from the k state under consideration to lower l states given by

$$\alpha_k = \sum_{l(<k)} \Gamma_{k\to l}. \tag{5.8}$$

Performing an integration of Eq. 5.7 and exchanging the orders of integration and summation, one may find the occupation of the sublevels of any arbitrary state. One also note that the recursion formula can be successively iterated to yield a finite series of nested sums and integrals. If there are no upper feeding states then the sum is zero, resulting in a vanishing integral and one obtains $N_k(t) = N_k(t = 0)e^{-\alpha_k t}$, which is the usual exponential decay law. The transition rates and energy levels have been calculated in the same way as described in Sec. 3.4. Further on to many-electron atomic systems, the FAC (Flexible Atomic Code) utilizes the modified multi-configuration Dirac-Hartree-Fock-Slater (DHFS) method for speed, multi-utility, and collisional-radiative modelling [136]. Therefore, it is possible to calculate the energy levels and transition rates between arbitrary states for all atoms or ions in any desired charge state.

For direct electron capture into bare lead projectiles, we consider rigorous relativistic calculations for inner shells up to $n = 10$ and the non-relativistic dipole-approximation for states up to $n = 165$ (see Sec. 4.2). In practice, however, one may expect that, apart from the direct recombination, the feeding transitions from the high-lying levels will also contribute to the population of the ionic substates. Detailed experimental studies of this phenomenon have been facilitated at the ESR storage ring exploiting both internal gas target [121] and the electron cooler [18].

The cascade contributions depend on the total number of excited sublevels which

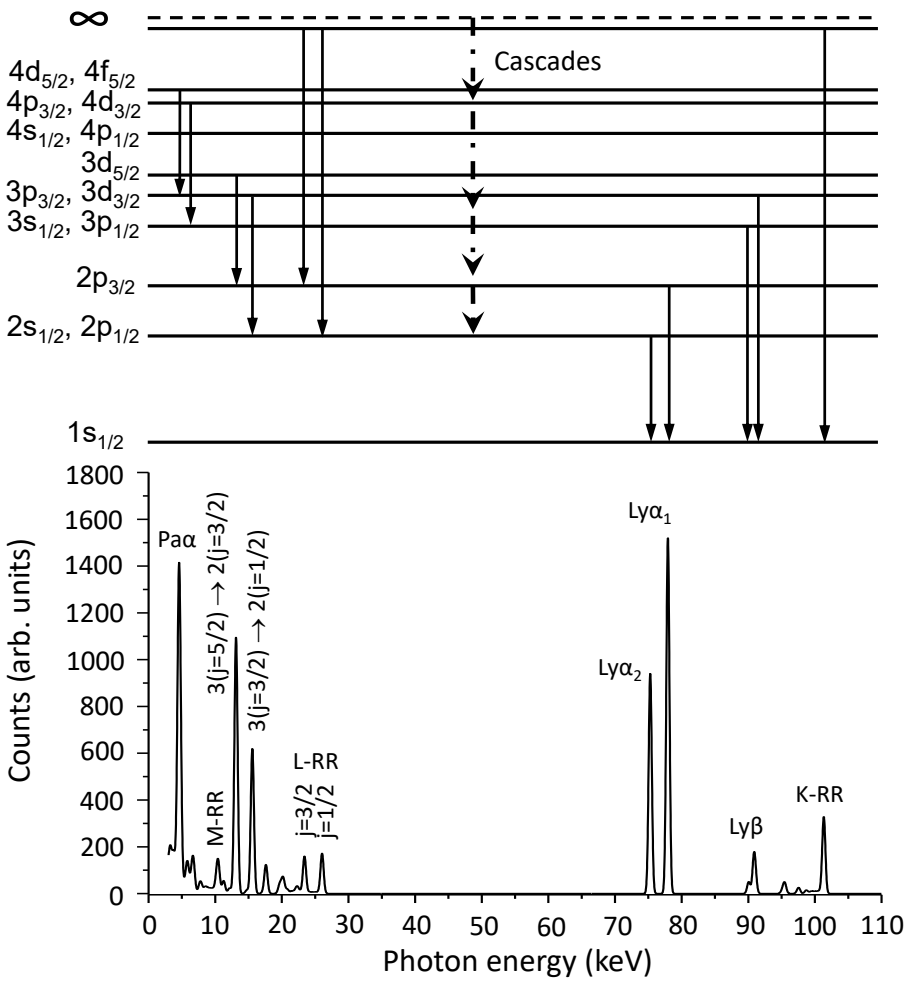

Figure 5.9: Level scheme and the simulated x-ray spectrum of cascade feeding in hydrogen-like Pb ions. Here, the initial population of each excited state is formed by free electron capture of 10 MeV/u Pb^{82+} ions at an electron cooler with relative electron-ion collision energy of 2.59 meV. The spectral line profiles are approximated by a Gaussian function assuming an experimental resolution of 550 eV. In the figure, all possible transition types associated with RR radiations together with characteristic projectile x-rays are shown.

are considered in the realistic experimental conditions. For the one conducted at high collision energies, where the recombination cross sections show a $1/n^3$ dependence, including states up to $n \approx 20$ could already achieve good agreement between experimental data and theoretical predictions [121]. However, for present experiment performed at the electron cooler of CRYRING@ESR with collision energies close to 0 eV, it is evident that cascade contribution from high-Rydberg states prevails. At such low energies the recombination rate scales with $\sim 1/n$ for inner shells [203], for high Rydberg states with the binding energies $E_{nl} < kT_{\perp}$ the scaling law for RR at high relative energies is restored again ($\alpha_{nl} \sim 1/n^3$) [121]. Correspondingly, there are very significant contributions from high (n, l) levels regarding the production of characteristic projectile x-rays resulting via radiative cascades from these high Rydberg levels [16, 18].

Based on the calculation of the initial population distribution via RR for all atomic levels (see Sec. 4.3) in combination with feeding transitions based upon time dependent rate equations, a program dedicated to radiative decay cascades was developed. As we note that 100 states have already made 996815 different transitions whereas the total angular momenta is dominated by spin-orbit coupling, a fast computer code for high Rydberg state calculating nonrelativistic electric dipole transitions was exploited in hydrogenic systems of H-like lead. To reveal the radiative decay dynamics in the intensity of characteristic x-ray lines, a time discrete simulation, with an arbitrary selected step width, was add to the computer program, which is suitable when excited states up to $n = 165$ have to be considered in current experiment. At the bottom part of Fig. 5.9, the result of a time integrated x-ray spectrum is depicted by taking into account our experimental observation time of about 70 ns (see Fig. 5.1). The energy range of this theoretical spectrum covers all transitions in a wide range of x-ray energies (from 3 to 105 keV), spanning fine-structure resolved Lyman, Balmer and Paschen x-ray lines along with the RR transitions into the K-, L- and M-shell of the Pb^{82+} ions.

5.4 Experimental results and comparison with theory

As discussed in the previous section, radiative recombination into highly excited states of the projectile will result in decay cascades, mainly by electric dipole transitions, and is likely to end up in one of the intermediate states considered here. While the cascade photons between highly excited levels are usually not detected, the decay photons involving K-, L-, and M-shells are measured by the Ge(i) detectors (see Fig. 5.2). To compare with theoretical spectrum modelling, the measured x-ray spectra are corrected for the energy dependent detection efficiencies of each individual x-ray detector. For this purpose the germanium detector response function is simulated with the well-established Monte Carlo EGS5 code [204]. For the specific detectors applied this method has been proven to provide reliable results in particular for the case of relative (not absolute) detector efficiencies (see e.g. [205]).

The following concentrates on the discussion of the observed prompt RR transitions as well as of the characteristic x-ray lines in comparison with the simulation based on the theoretical modelling described in Sec. 5.3.2. In the spectra the very small line broadening of the RR lines due to the temperature of the electron beam is negligible compared to the intrinsic resolution of the detectors. The strongest line associated with the direct RR refers to recombination into the $1s_{1/2}$ ground state (K-RR) and the intensity of other recombination transitions observed drop off as the recombination rates scale approximately as $1/n$ [142, 203] for the inner shells.

The L-RR populates the excited L-shell levels in Pb^{81+}, and hence contributes to the initial line intensity of the Ly$\alpha_{1,2}$ transition. Likewise, the M-RR contributes to the Balmer series and the Lyβ transition.

Figure 5.10 shows the part of the x-ray spectra containing the Lyman transitions along with the K-RR radiation (laboratory frame; thin gray lines), recorded at the two observation angles of 0° and 180° in comparison with the results of the spectra simulation (thick red lines). Here, the Doppler shift of the photon energies as well as corrections taking into account the angular distribution of RR radiation (for details, see Sec. 4.4) are applied. To compare with the registered x-ray spectra,

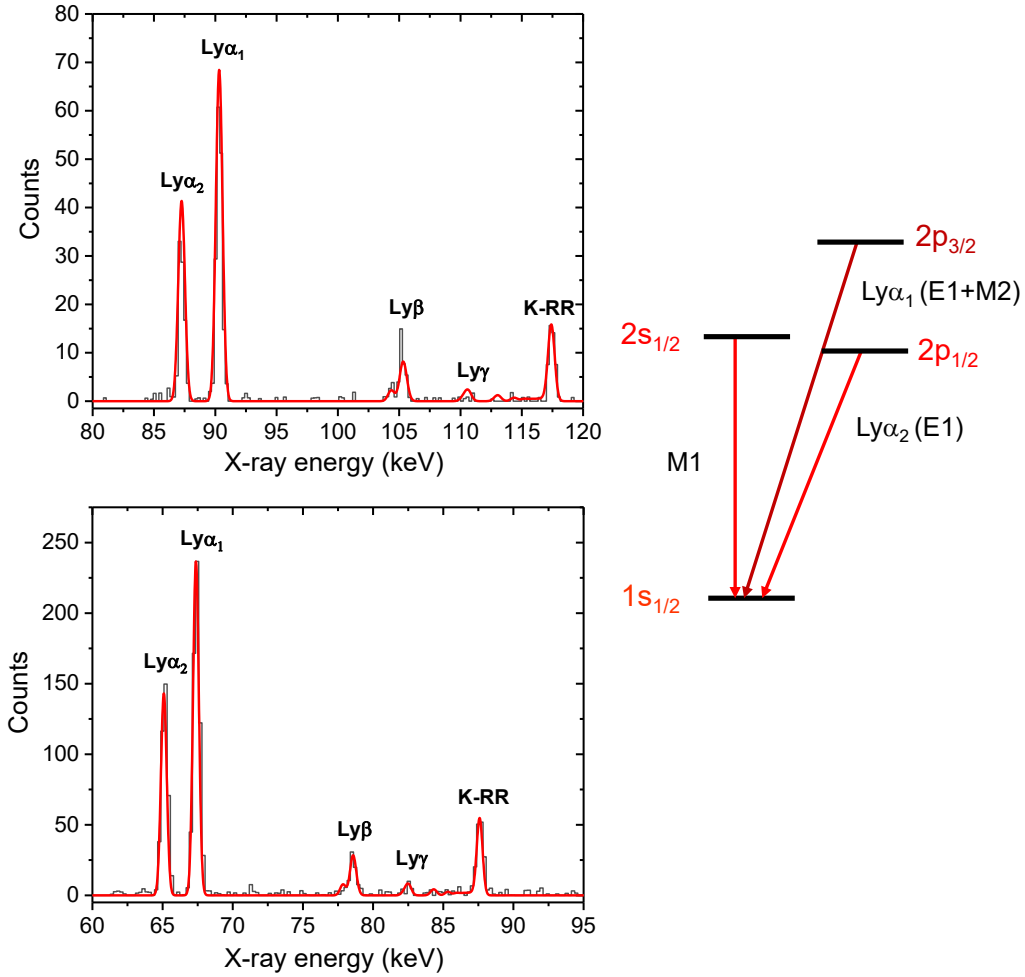

Figure 5.10: The Lyman series and the K-RR measured at 0° (top part) and 180° (bottom part) relative to the ion beam axis (thin gray lines). The thick red lines display results of the simulation (for details see text). The intensity of the K-RR line is used for normalization. In the level diagram all possible transition types between the states with $n = 1, 2$ in H-like lead are shown.

the simulated spectral line profiles are approximated by a Gaussian function with a FWHM of 550 eV accounting for the intrinsic resolution of the Ge(i) detectors used. The prompt K-RR line intensity appears at an x-ray energy of 101 keV in the projectile frame and is used to normalize the simulated Lyman spectrum.

For the Lyα_2 $2p_{1/2} \rightarrow 1s_{1/2}$ transition there is a line blend due to the $2s_{1/2} \rightarrow 1s_{1/2}$ $M1$ decay which is energetically separated from the former by the $n = 2$ Lamb shift of 39 eV [98] which cannot be resolved in our spectra due the intrinsic detector resolution. Moreover, one note that for Pb^{81+} the $M1$ decay rate amounts to $\Gamma_{M1} = 5.32 \times 10^{13}$ s^{-1} whereas the one for the competing two-photon decay channel to $\Gamma_{2E1} = 2.03 \times 10^{12}$ s^{-1} [120]. Due to the dominance of the $M1$ decay for the $2s_{1/2}$ state, in the following the two-photon decay is neglected. Based on the dedicated spectrum simulation, the $M1$ $2s_{1/2} \rightarrow 1s_{1/2}$ ground state transition is estimated to contribute by about 15% to the observed Lyα_2 intensity. Overall, a very good agreement between the experimental and the simulated spectra can be stated for both observation angles.

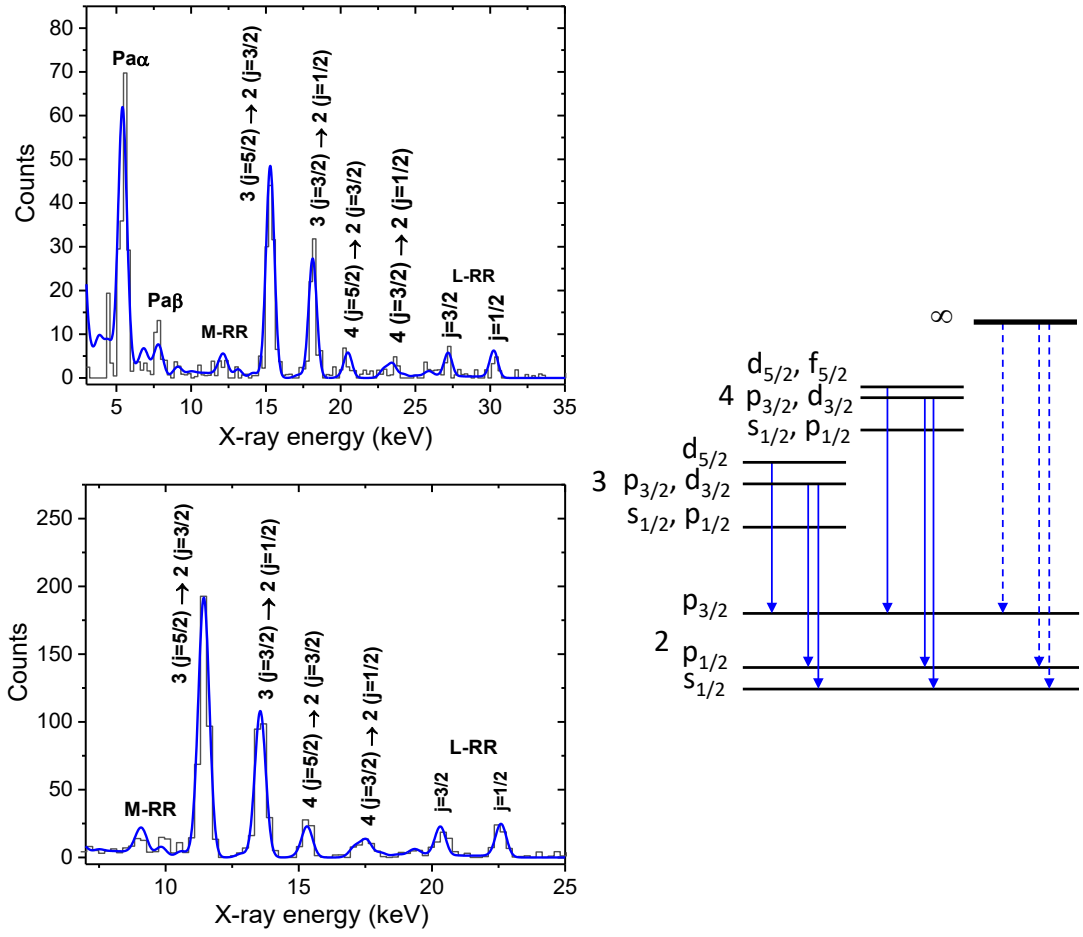

Figure 5.11: X-ray spectra associated with prompt L-RR and M-RR radiation together with characteristic Balmer and Paschen transitions measured by two Ge(i) detectors placed at 0° (top part) and 180° (bottom part) with respect to the ion beam axis (thin gray lines). The thick blue lines give the results of the cascade simulation. Two intense Balmer transitions are Baα_1: 3 ($j = 5/2$) $\rightarrow$ 2 ($j = 3/2$) and Baα_2: 3 ($j = 3/2$) $\rightarrow$ 2 ($j = 1/2$). In the level diagram the Balmer transitions relevant for our measurement are shown.

Complementary information on the Lyman spectrum is provided by the Balmer and Paschen series. Fig. 5.11 compares the experimentally recorded low-energy

x-ray spectra (thin gray lines), consisting of the prompt L-RR and M-RR x-ray transitions together with the characteristic Balmer and Paschen series at 0° and 180° with the theoretical model based on cascade calculations (thick blue lines). Again, for comparison with the experimental data, the line intensity of K-RR population is used to normalize the simulated spectra. In addition, the most prominent Balmer lines in the spectra are marked by arrows in the level diagram, explaining the origin of various characteristic x-ray lines. Here, I would like to stress that due to the Doppler blue-shift in combination with the high transmission of low-energy photons through the beryllium view port at 0°, Paschen radiation from Pb^{81+} is observed for the very first time with a relative intensity comparable to the overall line intensities of the Balmer spectrum. However, due to the narrow line spacing, the experimental resolution does not allow us to resolve the individual transitions contributing to the observed Paschen-α line whereas in the case of the Balmer series, a multitude of transitions, basically due to the fine-structure splitting of the $n = 2$ and $n = 3$ states, are clearly visible in both x-ray detectors. Only small discrepancies are observed in the region of Paschen lines. These are most likely the result of a low-energy asymmetry of peak profiles that arises from missing resolution of the detector, and are partially due to the spectrum absorption effects in the beryllium window that are not regarded thoroughly at the low-energy part. Furthermore, the well resolved $L\text{-RR}_{j=3/2}$ and $L\text{-RR}_{j=1/2}$ x-ray lines mark at the same time the series limit for transitions decaying from high n levels directly into the $2s_{1/2}$, $2p_{1/2}$ and $2p_{3/2}$ levels, respectively.

In contrast to the Balmer series measured at high collision energies where RR favors capture into s-states resulting in $s \rightarrow p$ transitions [121] (e.g. the $3s_{1/2} \rightarrow 2p_{3/2}$), the dominant transitions observed in the current experiment stem from atomic levels with angular momenta $l \geq 1$. This distinct difference is again attributed to the role of the RR population mechanism in which electron capture at low relative energies populates preferentially n states with $l \approx n/3$ [155]. Moreover, for comparing with the observed x-ray line emission, the initial (n, l) population distribution is the starting point for cascade calculations based on the specific decay rates for the individual levels to be considered. For the inner shells ($n < 10$), these cascades lead to a preferred population of high angular momentum states with $l = n - 1$, resulting in subsequent Yrast transitions with $l \rightarrow l - 1$ [20]. Indeed, the corresponding theoretical x-ray line spectra seem to describe the experimental findings very well (see Fig. 5.10 and Fig. 5.11).

In this experiment, both the prompt RR transitions as well as characteristic Lyman, Balmer, and even Paschen series were produced to a large extent via RR into high Rydberg states and subsequent cascades, the spectra provide a possibility to study the time development of the mentioned cascade process. The calculated time development of the characteristic line emission is depicted in Fig. 5.12. In

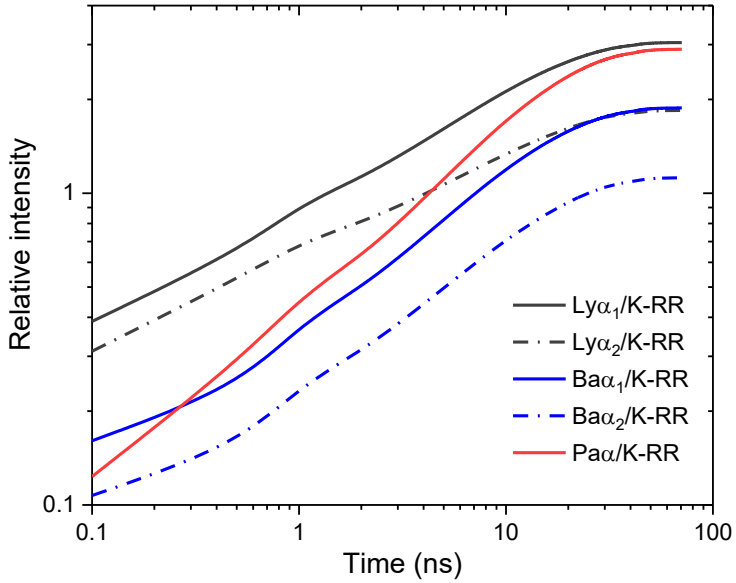

Figure 5.12: Cascade calculations of the characteristic line intensities as a function of flight time of charge exchanged Pb^{81+} ions at 10 MeV/u at the electron cooler of the CRYRING@ESR storage ring. All line intensities are normalized to the K-RR population (gray solid line: Lyα_1/K-RR; gray dash-dotted line: Lyα_2/K-RR; blue solid line: Baα_1/K-RR; blue dash-dotted line: Baα_2/K-RR; red solid line: Paα/K-RR). Calculations are performed for recombination into excited projectile states up to $n = 165$.

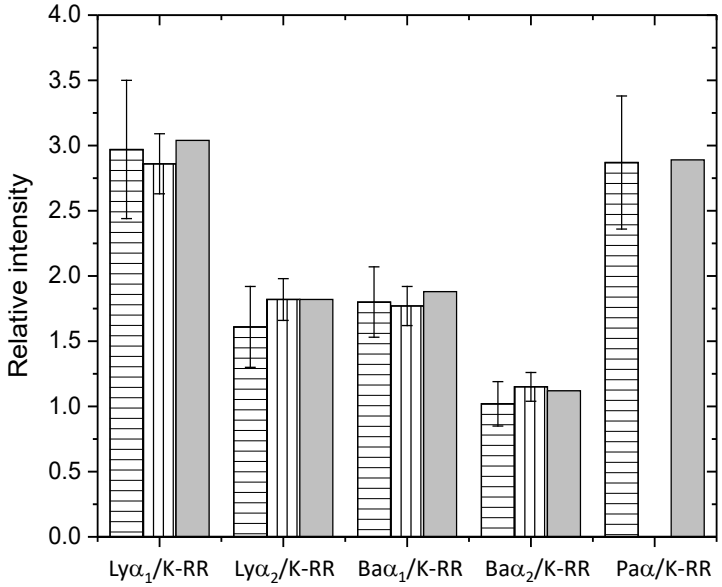

Figure 5.13: Experimental results in comparison with the time-dependent theoretical model (gray columns) for characteristic line intensities normalized to the one of K-RR population. White columns with horizontal strips show experimental data at 0°, white columns with vertical strips show experimental data at 180°.

the figure, the characteristic line intensities are normalized to the prompt K-RR intensity. As can be seen, the initial characteristic line intensities induced by direct RR into L-, and M-shells ($t = 0$) are enhanced by up to a factor of 10 following

deexcitation cascades within $\Delta t \approx 40$ ns, which is comparable to the time-of-flight of the ions from the end of cooler section to the dipole magnet in front of the 0° x-ray detector (see Fig. 5.1). In general, one can state that within this time period, to be compared to the time-of-flight of the ions inside the cooler section of about 30 ns, the vast majority of electrons having recombined into excited states of the ion reach the ground state. Within the statistical accuracy, the time integrated line intensities for both x-ray detectors appear to be in excellent agreement with the results from cascade calculations, as shown in Fig. 5.13. These findings are generally consistent with those from earlier studies conducted at the ESR electron cooler [15, 16, 17, 18].

Based on the comparison with the observed Lyman-α line intensities (see Fig. 5.13), one could conclude that there is a very significant contribution to the Lyman-α emission arising from recombination into highly excited states and subsequent cascades. At a high nuclear charge of the Pb nucleus, transitions from L-, M- and N-shell to the ground state of Pb^{81+} ions are fast, even the $M1$ magnetic dipole transitions have to be considered as prompt. For instance, the $E1$ and $M1$ transition rates of corresponding Lyman-α transitions are of the order of 2×10^{16} and 5×10^{13} s^{-1} respectively [118, 120]. To be more specific, the L-RR populating the excited L-shell sublevels in Pb^{81+} should represent the initial line intensities of Lyman-$\alpha_{1,2}$ transitions as prompt contributions. Likewise, the population of M-RR contributes to the initial Balmer series and Lyman-β line via fast decay at the time interval of $\Delta t \lesssim 10^{-13}$ s. The results are exhibited by the shaded areas in Fig. 5.14 whereby the unshaded areas are identified as the delayed cascade feeding to the observed characteristic projectile x-rays. To demonstrate this scheme, and to gain further insight, Table 5.1 presents the contributions from highly excited states and subsequent feeding transitions to the formation of pronounced Lyman-α_1 and Lyman-α_2 lines observed in current experiment, as the transitions into different j-states of the L-shell are clearly resolved. Here, it is important to stress that the theory is consistent with the experimental data at 0° and 180° observation geometry. As already been pointed out in Refs. [18, 22] that the delayed x-ray emission occurring outside the electron cooler section is in particular sensitive to the observation angle at 0°, while at 180° it is strongly suppressed due to the substantially reduced solid angle (see also Fig. 5.1).

Table 5.1: Contribution from feeding cascades finally populating the L-shell sublevels to the intensities of Lyman-α_1 and Lyman-α_2 lines. Uncertainties shown here are due to counting statistics whereas systematic uncertainties are neglected.

Characteristic x-rays	0 deg	180 deg	Theory
Lyα_1	93.6% ± 1.99%	94.0% ± 0.94%	93.9%
Lyα_2	86.4% ± 4.26%	87.4% ± 1.69%	86.8%

A further important aspect of our study is to investigate in detail the prevail-

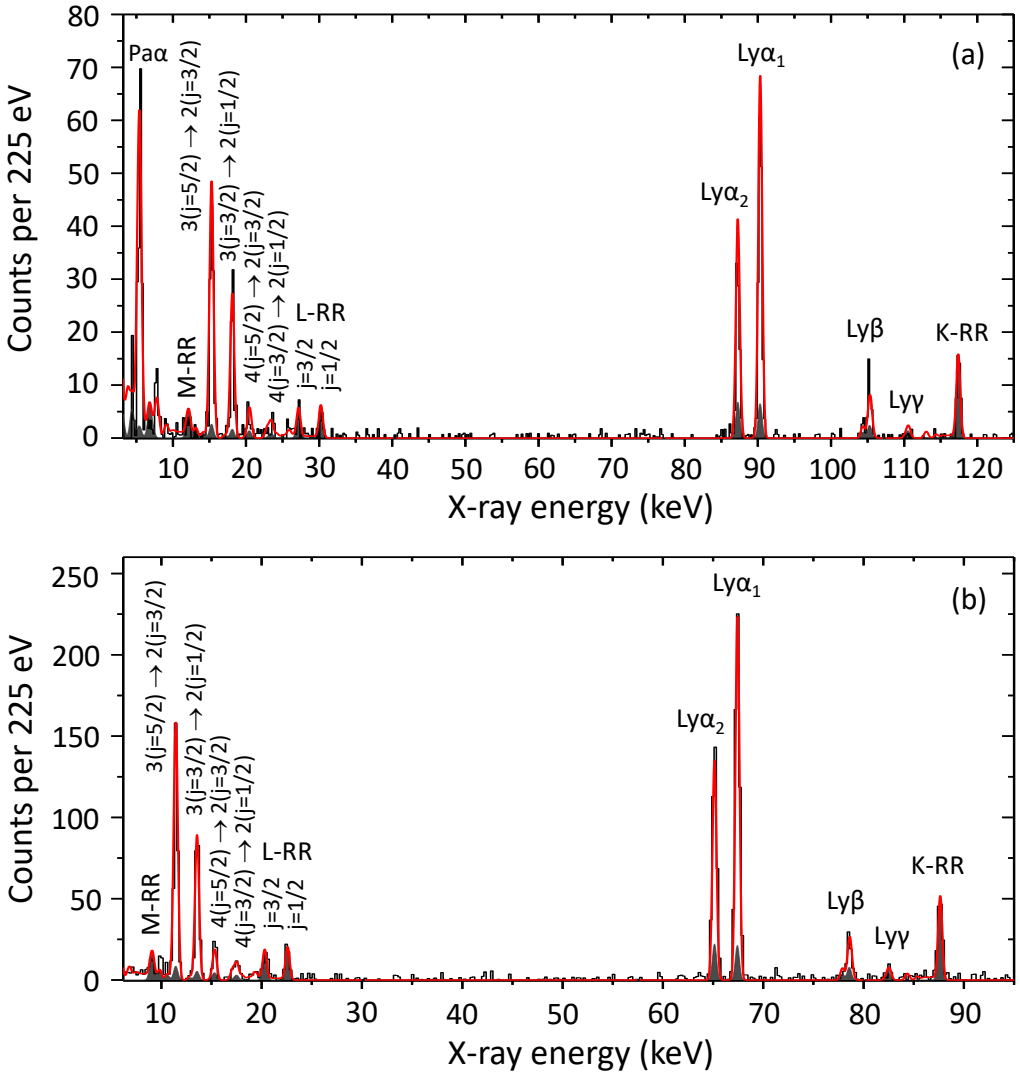

Figure 5.14: X-ray spectra measured (black lines) at observation angles of (a) 0° and (b) 180° by two Ge(i) detectors in coincidence with the particle counter for 10 MeV/u Pb^{82+} ions interacting with free electron target at the electron cooler of CRYRING@ESR. The red lines give the result of time integrated spectra based on a cascade calculation using the theoretical RR cross sections, convoluted with the experimental response function described by an anisotropic Maxwell-Boltzmann distribution $f(\mathbf{v})$ (see Sec. 4.3). The shaded areas represent the contribution from prompt transitions assuming within the time interval of $\Delta t \lesssim 10^{-13}$ s.

ing cascade decay dynamics of the observed characteristic projectile x-rays at the CRYRING@ESR electron cooler. As to the superior timing characteristics exhibited for 0° x-ray detector, Fig. 5.15 (a) depicts a two dimensional scatter plot of the coincidence time (time difference between photon and particle detection) versus the observed x-ray emission as registered at an observation angle of 0°. Also, due to the low ion beam velocity of $\beta \approx 0.146$ and the experimental time resolution of about 20 ns, photon events which occurred inside the cooler section can be distinguished from these where the emission took place just in front of the 0° x-ray detector. It is evident to note that such photon events stemming from the prompt emission inside

the cooler section are distributed over a time interval of about $\Delta t_1 \approx 30$ ns, whereas the delayed characteristic projectile x-rays span over the whole observation time of about $\Delta t_1 + \Delta t_2 \approx 70$ ns (note, the delayed emission is here at earlier times). In addition, the 2D spectrum refers to all x-ray events registered without any background subtraction applied, thus random events caused by bremsstrahlung arising from a fraction of the electron beam hitting materials in the cooler can be identified as a continuous, broad band at an energy close to 5 keV. To demonstrate the time evolution of radiative cascades to the formation of characteristic Lyman and Balmer series, Fig. 5.15 (b)-(d) show the time integrated characteristic line intensity ratios as a function of time-of-flight of Pb^{81+} ions from the entrance of the cooler section to the dipole magnet in front of the 0° x-ray detector (amount to about 70 ns and see Fig. 5.1). One may note that at $t \lesssim 0.1$ ns the relative populations of Lyman-$\alpha_{1,2}$

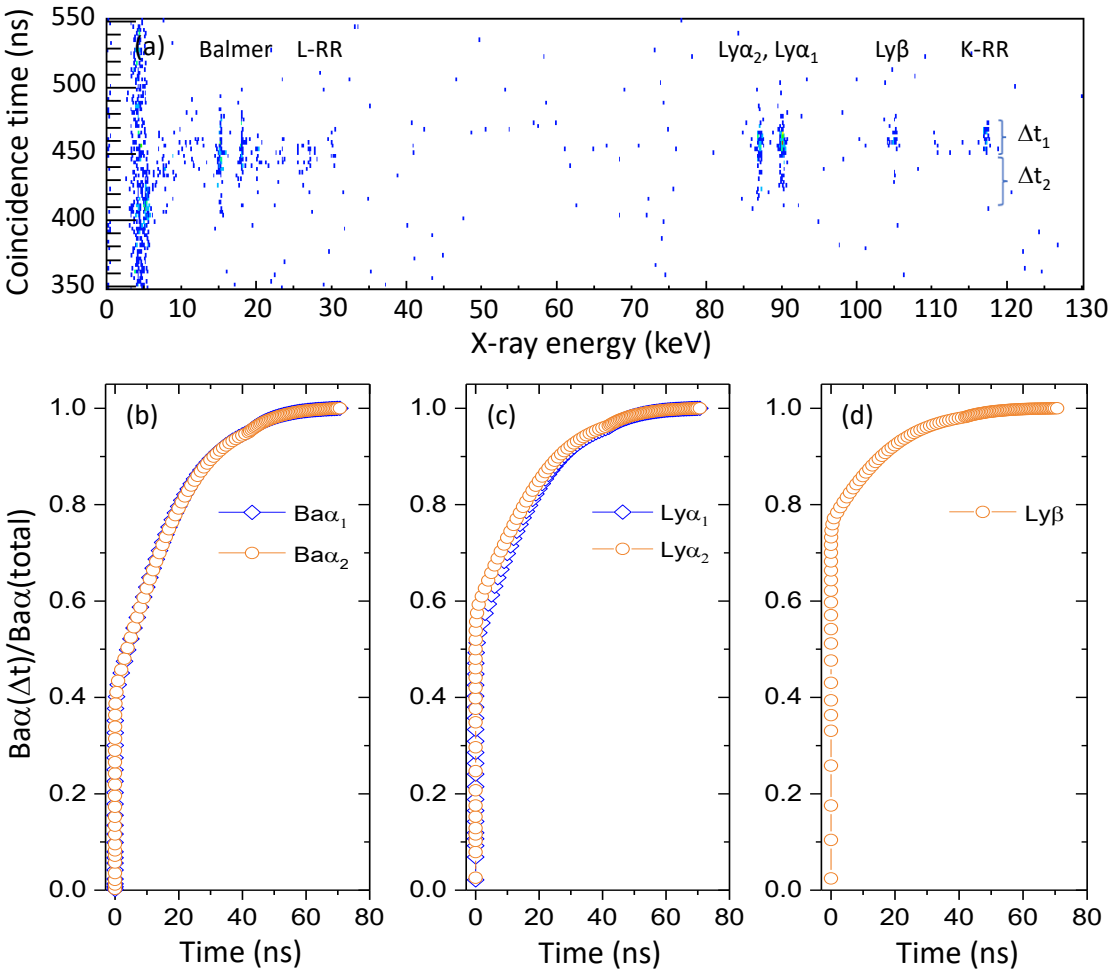

Figure 5.15: (a) Two dimensional scatter plot of the observed x-ray emission versus the coincidence time as registered at an observation angle of 0°. The latter refers to the time difference between photon (start) and particle (stop) detection in relative time scale. $\Delta t_1 \approx 30$ ns refers to the cooler section, whereas $\Delta t_2 \approx 40$ ns to the region outside the electron cooler. (b)-(d) The time integrated characteristic line intensity ratios as a function of time-of-flight of Pb^{81+} ions from the entrance of the cooler section to the dipole magnet in front of the 0° x-ray detector.

and Balmer-$\alpha_{1,2}$ by direct feedings from low inner shells are rather small compared to the one of Lyman-β. However, owing to the feeding transitions from higher-lying levels, the intensities of Lyman-$\alpha_{1,2}$ and Balmer-$\alpha_{1,2}$ increase rapidly and reach 90% of the corresponding total rate coefficient within $\Delta t \approx 27$ ns and $\Delta t \approx 30$ ns respectively, which are comparable to the time-of-flight of the ions inside the cooler section of about 30 ns. For Lyman-β it is even fast and within time period of $\Delta t \approx 17$ ns. Both reach a saturation after about 50 ns and basically all electrons that contribute from high Rydberg levels decay to the ground state.

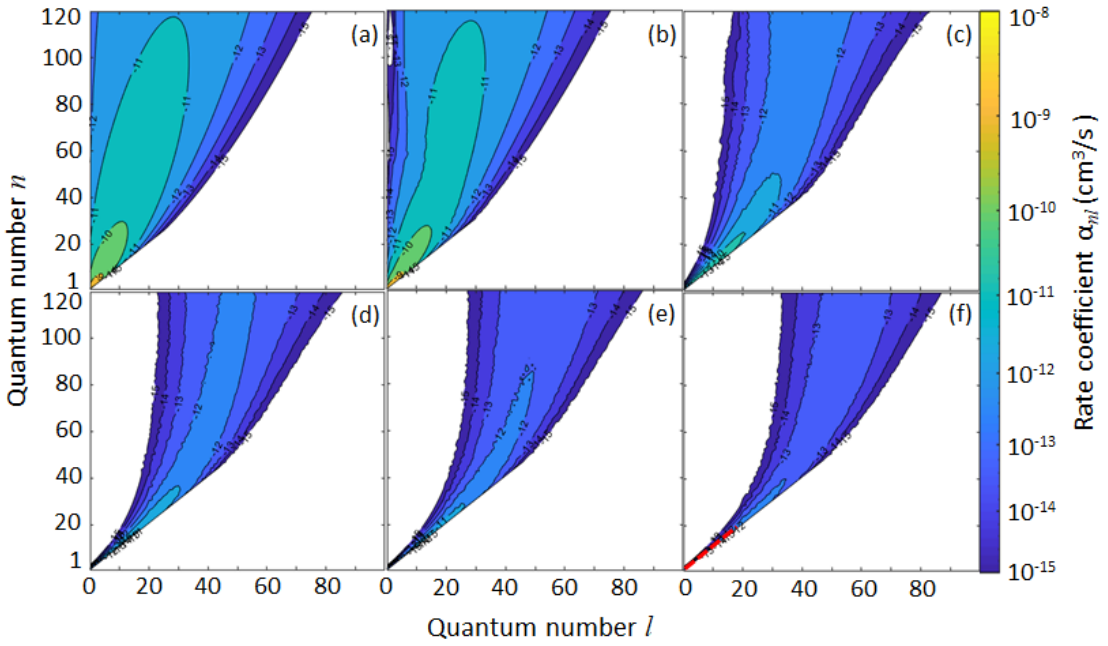

Figure 5.16: The (n, l)-population rate coefficient distributions at various time nodes of (a) $t = 0$ ns, (b) $t = 0.1$ ns, (c) $t = 10$ ns, (d) $t = 30$ ns, (e) $t = 45$ ns and (f) $t = 70$ ns. In (f) for inner shells of $n \leq 20$, the $l = n - 1$ levels (indicated by red dotted line) are preferentially populated followed by radiative cascades. Here, n up to $n = 120$ and l up to $l = 80$ are shown on the axis, the negative numbers marked in figures are the integer powers of the number 10.

In order to elucidate in more detail the RR population mechanism that leads through feeding cascades to Balmer ($n = 3, 4... \rightarrow n = 2$) as well as to Lyman transitions ($n = 2, 3, 4... \rightarrow n = 1$) at relative low collision energies, Fig. 5.16 depicts the calculated (n, l)-population rate coefficient distributions at different times. Figure 5.16 (a) represents the initial state-selective rate coefficients ($t = 0$ ns) for RR into all atomic levels of Pb^{82+} at the electron cooler of CRYRING@ESR as a function of the principle and angular quantum number (n, l). As can be seen that for the electron binding energy of (n, l) state $E_{nl} \gg kT_{\perp}$, RR populates preferentially n states with $l \approx n/3$ [155]. Moreover, based on the time-dependent cascade calculations, one may found that states with a high principle quantum number n but a low angular momentum quantum number l will decay directly to the inner shells via fast electric dipole transitions, thus the populations in these high levels shrink

drastically at a later time as shown in Fig. 5.16 (b)-(f). However, states having not only a high n but a high l will decay step by step ($l \rightarrow l \pm 1$ transition) to lower lying levels until a transition into the ground state occurs. Within our experimental observation time of about 70 ns, these feeding cascades from high Rydberg states lead to a final preferred population of high angular momentum states with $l = n-1$ in inner shells (states of $n \leq 20$ marked by the red dotted line in Fig. 5.16 (f)), resulting in subsequent Yrast transitions with $l \rightarrow l-1$ [20], hence the formation of intense Lyman-$\alpha_{1,2}$ and Balmer-$\alpha_{1,2}$ lines as observed in our experiment (see Fig. 5.14). This could also explain the low intensity of recorded Lyman-β line arising mainly from two components ($3p_{1/2} \rightarrow 1s_{1/2}$ and $3p_{3/2} \rightarrow 1s_{1/2}$ transitions), where most populated $3d_{5/2,3/2}$ levels contribute to the formation of Balmer-$\alpha_{1,2}$ spectra. Again, it can be well reflected in Fig. 5.15 (d) that the slowly radiative cascade processes from high Rydberg states contribute only about 10% to the total rate coefficient of Lyman-β lines from $t = 18$ ns to $t = 70$ ns.

Chapter 6

Application of radiative cascade simulation program: repopulation of excited states in U^{90+} ions

High-Z helium-like ions represent the simplest multi-electron systems ideally suited for the study of the interplay between the effects of electron-electron correlations, relativistic and QED in strong fields. However, in contrast to hydrogen-like and lithium-like ions, rare experimental information is available about the excited states in the high-Z domain of helium sequence. To date, for helium-like uranium ions, basically no precise experimental data for the atomic structure are available.

During the spring beam time of 2021, we carried out a first of x-ray spectroscopy experiment addressing helium-like uranium at the CRYRING@ESR storage ring at GSI Darmstadt by using highly-granular, novel high-resolution microcalorimeters. For this purpose, the same experimental geometry at the electron cooler section was utilized, which has already been successfully demonstrated in the former experiment for hydrogen-like lead ions. A detailed discussion of the experiment and experimental results will be given elsewhere [206, 207].

6.1 Experiment and x-ray spectra

The experiment was performed at the new experimental heavy-ion storage ring CRYRING@ESR in the framework of the SPARC collaboration [1] [208]. A sketch of the experimental setup at the electron cooler is displayed in Fig. 6.1. Typically about 10^6 H-like uranium ions with an decelerated beam energy of 10.3 MeV/u were eventually transferred from the ESR and stored in the CRYRING@SER. In CRYRING@SER the beam was continuously electron-cooled at a voltage of 5634.5 V and an electron current of 30.5 mA, forming a beam with a diameter of 2-3 mm

[1] Stored Particles Atomic Research Collaboration

with relative momentum spread of $\Delta p/p \sim 10^{-5}$. The x-rays produced by direct electron capture into bound states of U^{91+} ions or following cascade decay were detected by two Metallic Magnetic Calorimeters (maXs-100) (for details, the reader is referred to section 2.4.2), which were mounted 4.0 m at 0° and 3.7 m at 180° with regard to the midpoint of electron cooler section along the ion beam axis. Here, the maXs-100 x-ray detectors were mounted in front of two dedicated vacuum separation chambers [21] which were equipped with 100 μm thick beryllium x-ray windows, allowing for the transmission of low-energy x-rays (down to about 5 keV) [71]. The geometry of detector arrangement at observation angles of 0° and 180° was precisely determined by laser-assisted, computer-controlled trigonometry, where Doppler broadening and possible uncertainties of the observation angles are basically not affecting the observed x-ray spectra [113, 196].

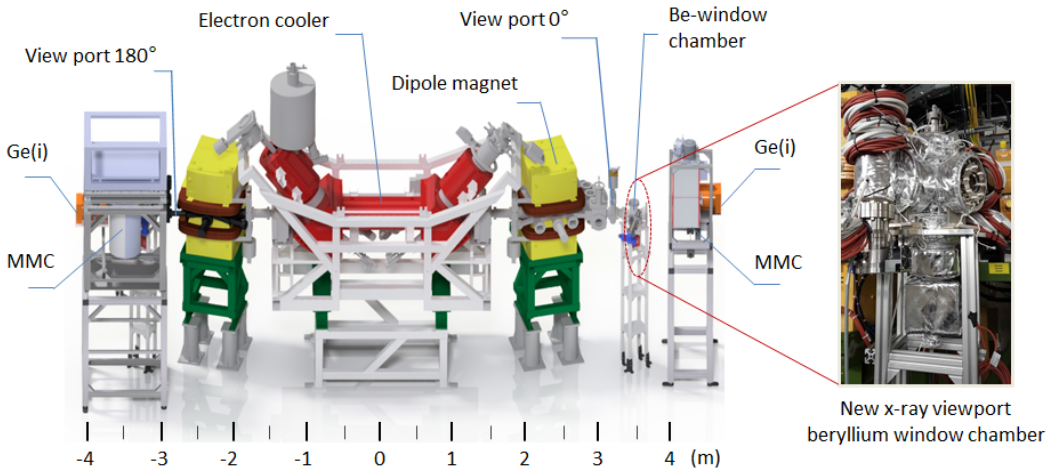

Figure 6.1: CAD plot of experimental setup at the electron cooler of the CRYRING@ESR storage ring. At 0° and 180° observation geometry, i.e. the extended size of the electron cooler section, dedicated vacuum separation chambers are used. The chamber at 180° is depicted on the right side of the figure. The x-ray detection was accomplished by two low-temperature calorimetric detectors (MMC). In addition, two high-purity, planar germanium x-ray detectors were also mounted as a pretest of the data acquisition system.

During the accumulation of spectra, x-rays emitted from the cooler region were measured in coincidence with down-charged U^{90+} ions registered by a channel electron multiplier based ion detector [49, 188], located downstream to the first dipole magnet behind the electron cooler. Here, to gain proper control over possible electronic drifts of the maXs-100 detector, a lead-shielded box with a movable source holder was used, which enables a continuous calibration that is synchronized with the accelerator cycle of the CRYRING@ESR [21]. Fig. 6.2 displays a calibrated sample x-ray spectrum at 0° as observed for initially hydrogen-like uranium ions recorded by one of the maXs-100 detectors. In the low energy part, the intensity pattern of the multitude of well-resolved Balmer transitions was used to deduce the

state-sensitive population rate coefficients. Here, the Balmer transition refers to the transitions from higher levels to $n = 2$ states of He-like uranium ions. Special emphasis is given to the achieved spectral resolution of better than 80 eV at x-ray energies close to 110 keV enabling for the first time to resolve the substructure of the $K\alpha_1$ and $K\alpha_2$ lines.

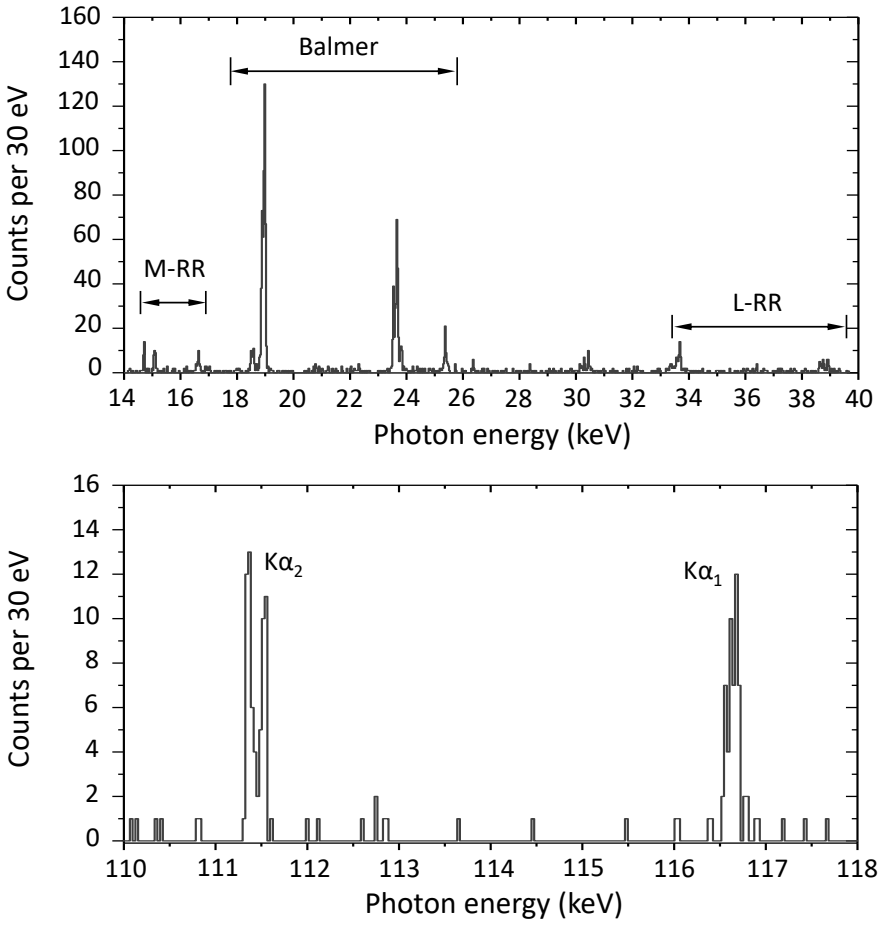

Figure 6.2: Sample preliminary x-ray projectile spectra (laboratory frame) produced by electron capture in U^{91+} on free electron target at an observation angle of 0° [206, 207]. Top: preliminary spectrum data, containing the Balmer series together with L-RR and M-RR transitions, in the low energy part. Bottom: preliminary spectral data of the $L \rightarrow K$ transitions in U^{90+} located in the high energy part.

6.2 Theoretical spectra generation and analysis

A comparison of the observed x-ray spectra with theory requires a precise spectra simulation technique where the complete level structure, transition rates, transition energies, as well as the theoretical (n, l, j) rate coefficients for electron capture have to be incorporated.

The RR processes for the fully stripped bare ions only involve one electron in hydrogen-like system, and the exact relativistic Dirac wave function of electron

was given in many literatures (see [8] and references therein). For multi-electron atoms, the bound electron wave function can be calculated by the Dirac-Fock-Slater method, and the continuum processes are treated in the distorted-wave approximation [136], thus the method used here is well suited to the RR processes for not only the hydrogen-like atoms but also the multi-electron atoms. For atomic structure calculations, relativistic effects are fully taken into account using the Dirac Coulomb Hamiltonian, also here the first order QED effects (self energy and vacuum polarization) are considered.

In the merged-beam experiments, the captured electrons by the RR processes can populate on the high Rydberg states of U^{90+} ions up to $n > 100$, and the highest quantum number n is determined by the guiding magnetic field [190, 192]. In the present chapter, $n_{max} = 165$ is chosen same as Chapter 5. For $n \leq 20$, the RR cross section calculations are carried out within the framework of Dirac-Fock-Slater theory, in which the relativistic configuration interaction with independent particle basis wavefunctions is applied [136]. For $n > 20$, the RR cross section calculations are calculated using a set of recurrence relations proposed by Burgess [144, 163], considering an effective nuclear charge $Z_{eff} = Z - 1$ for hydrogen-like uranium. Being a nonrelativistic theory, the Burgess's approach does not give any $j-$sensitive population information. In order to get j-sensitive cross sections $\sigma^{RR}_{(n,l,j)}$, the cross sections for electron capture into the j subshells of U^{90+} are obtained by assuming a statistical distribution,

$$\sigma^{RR}_{(n,l,j)} = \frac{2j+1}{4(2l+1)}\sigma^{RR}_{(n,l)}. \tag{6.1}$$

With the calculated RR cross section, the state-selective rate coefficients can be obtained by a convolution of $\sigma^{RR}_{(n,l,j)}$ with a two-temperature Maxwellian distribution $f(\mathbf{v})$ in Eq. 4.13, which is consistent with the experiments conducted at the CRYRING storage ring [56, 156]. Given the state-selective RR rate coefficients with $kT_\perp = 3.54$ meV and $kT_\parallel = 63.69$ μeV up to $n_{max} = 165$ as the relative initial populations, the x-ray spectrum in the following cascade processes can be calculated according to the branching ratios consisting of the Einstein coefficients between each pair of states. For the bound states up to $n = 100$, the Einstein coefficients are obtained by FAC code [135, 136] using the modified multi-configuration Dirac-Hartree-Fock-Slater method, which includes the contributions of the electric dipole, electric quadrupole, magnetic dipole, and magnetic quadrupole transitions. For $n > 100$, the Einstein coefficients are calculated by a non-relativistic electric dipole approximation [137]. By generating databases for the decay rates and for the RR rates, the x-ray spectrum produced by the direct RR and the subsequent cascade processes are simulated.

Comparison of the simulated x-ray spectrum with the experimental measurement at 0° observation angle registered by one of the maXs-100 detectors in the low energy

part is shown in Fig. 6.3. For this purpose, the simulated spectral intensities are fitted to the experimental data by adjustment of the overall spectrum amplitude. In addition, the spectral line profiles are approximated by Gaussian functions with a FWHM of 75 eV. The calculated photon energies have been corrected by the Doppler shift, which are dependent on the angles θ between the emitted x-rays and the movement of U^{90+} ions, in the form of

$$E_{lab} = \frac{E_{proj}}{\gamma(1 - \beta\cos\theta)}, \tag{6.2}$$

where E_{proj} and E_{lab} are respectively the x-ray energies in the projectile and in the laboratory frame, β is the beam velocity in unit of light velocity and $\beta = v/c \approx 0.1469$ for ion beam energy of 10.3 MeV/u, and $\gamma = (1 - \beta^2)^{-1/2}$ is the relativistic Lorentz factor.

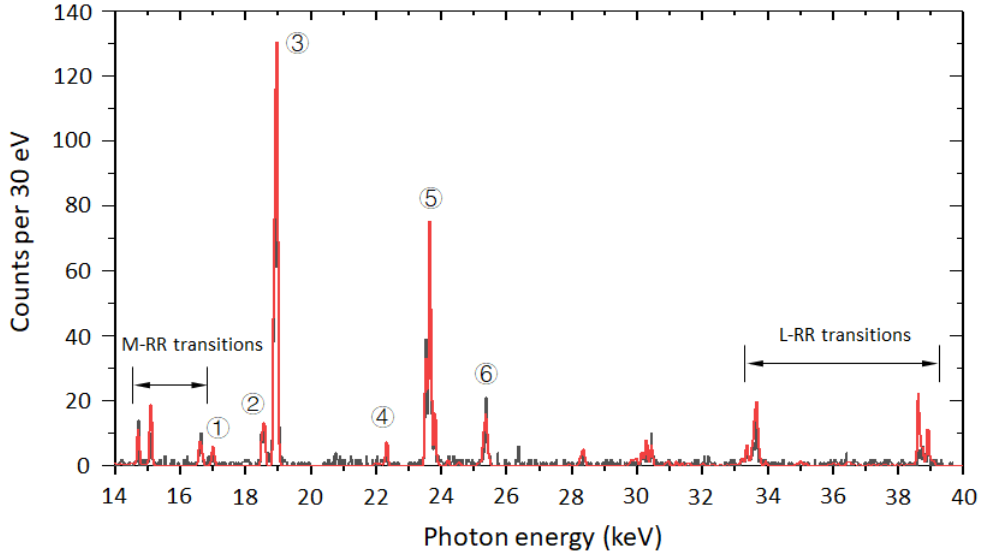

Figure 6.3: A preliminary coincident x-ray spectrum, registered at 0° observation angle from the electron-U^{91+} recombination processes at the electron cooler of CRYRING@ESR, is compared with our radiative cascade simulation program. The black line gives the result of experimental data [206, 207]. The red line displays the theoretical predictions of the direct RR and the following cascade processes.

It can be observed that the calculated photon energies with Doppler shift correction show a good agreement with the corresponding experimental values. In addition, the origin of the most prominent transition lines is explained in Table 6.1 (compare numbers given in Fig. 6.3 for the identification of Balmer transition lines). Since the photon intensities in the direct RR processes are proportional to the recombination rate coefficients, the corresponding x-ray spectrum from the direct L-RR and M-RR processes can be obtained straightforwardly by the relative values of state-selective recombination rate coefficients. These relative values of rate coefficients also constitute the initial populations in the sequential cascade processes,

Table 6.1: The most prominent Balmer transitions appearing in Fig. 6.3. The numbers quoted in the first row refer to numbers given in the figure for line identification.

1	$[1s_{1/2}3d_{3/2}]J=1 \rightarrow [1s_{1/2}3p_{3/2}]J=1$
	$[1s_{1/2}3d_{3/2}]J=2 \rightarrow [1s_{1/2}3p_{3/2}]J=2$
2	$[1s_{1/2}3d_{5/2}]J=2 \rightarrow [1s_{1/2}3p_{3/2}]J=1$
3	$[1s_{1/2}3d_{5/2}]J=3 \rightarrow [1s_{1/2}3p_{3/2}]J=2$
	$[1s_{1/2}3d_{5/2}]J=2 \rightarrow [1s_{1/2}3p_{3/2}]J=2$
4	$[1s_{1/2}3p_{1/2}]J=0 \rightarrow [1s_{1/2}2s_{1/2}]J=1$
5	$[1s_{1/2}3d_{3/2}]J=1 \rightarrow [1s_{1/2}2p_{1/2}]J=0$
	$[1s_{1/2}3d_{3/2}]J=2 \rightarrow [1s_{1/2}2p_{1/2}]J=1$
	$[1s_{1/2}3d_{3/2}]J=1 \rightarrow [1s_{1/2}2p_{1/2}]J=1$
	$[1s_{1/2}3p_{3/2}]J=2 \rightarrow [1s_{1/2}2s_{1/2}]J=1$
6	$[1s_{1/2}4d_{5/2}]J=2 \rightarrow [1s_{1/2}2p_{3/2}]J=1$
	$[1s_{1/2}4d_{5/2}]J=3 \rightarrow [1s_{1/2}2p_{3/2}]J=2$

whereby the x-ray spectrum from the cascade processes can be calculated by the branching ratios decaying into different final states. In the case of the Balmer series, a multitude of transitions, basically due to the fine-structure splitting of the $n=2$ and $n=3$ states, are clearly visible using maXs-100 detection system.

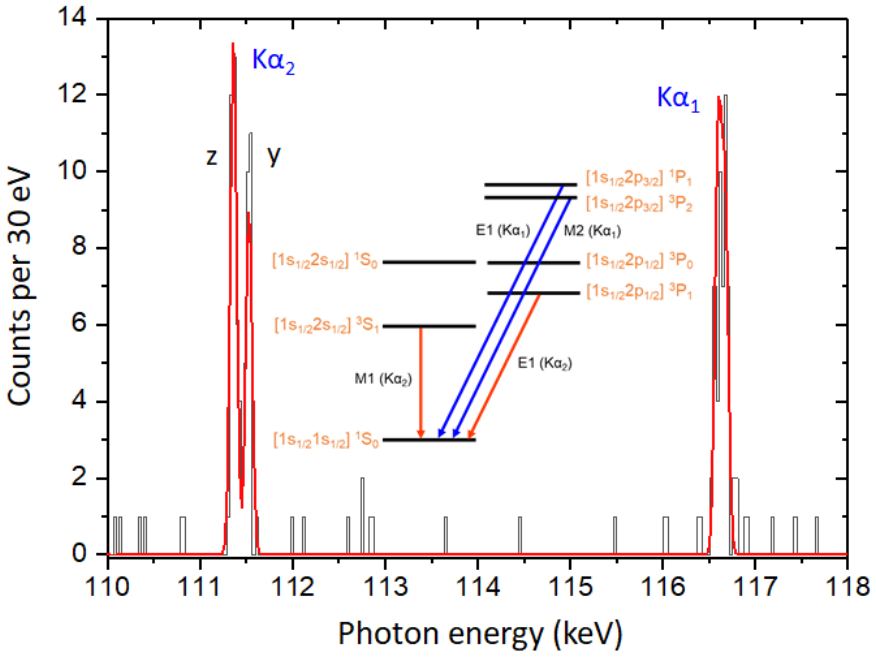

Figure 6.4: The preliminary coincident x-ray spectrum of the $L \rightarrow K$ transitions in 10.3 MeV/u U^{90+} ions registered by one of maXs-100 detectors at 0° observation angle with respect to the ion beam axis [206, 207]. The black line gives the result of experimental data, the red line displays the theoretical predictions using our radiative cascade simulation program. In the level diagram the $K\alpha_1$ and $K\alpha_2$ transitions relevant for our measurement are marked by arrows.

Most of the spectral peaks in Fig. 6.2 are produced by the cascade processes from high Rydberg states ($n \geq 3$), and the stronger ones correspond to the Balmer series. Here, It is important to stress that this specially tailed maXs-100 detector provides an acceptable quantum efficiency of about 50% for stopping x-ray photons at around 90 keV, and an absorption efficiency of 45% for such x-ray energy. Therefore, $L \rightarrow K$ transitions lines are also observable. Special emphasis is given to the spectral resolved energy splitting of z and y lines in $K\alpha_2$ as observed at 0° observation angle depicted in Fig. 6.4, where z and y lines denote $2\ ^3S_1 \rightarrow 1\ ^1S_0$ and $2\ ^3P_1 \rightarrow 1\ ^1S_0$ transitions, which is energetically separated from the former by 142.53 eV [145] as observed in the experiment. For presentation purposes the theoretical spectrum is normalized to the experimental one by adjusting to the $K\alpha_1$ line. We note that the intensity ratio $K\alpha_2/K\alpha_1 = 1.31 \pm 0.24$ obtained from the preliminary experimental data appears to be in good agreement with theoretical calculation of 1.19, which indicates that the theoretical approach applied is qualitatively in harmony with the measured spectrum and seems to prove that the versatile radiative cascade simulation program can be an important tool studying recombination processes.

Chapter 7

Summary

In this work I report on the first x-ray spectroscopic investigation of the process of radiative recombination (RR) for bare lead ions at the electron cooler of the CRYRING@ESR storage ring, which has recently been installed and commissioned at GSI/FAIR. The coupling of CRYRING, which was originally located at Marne Siegbahn laboratory in Stockholm with the experimental storage ring (ESR) of the GSI accelerator facility enabled us for the first time to store highly-charged heavy-ions in CRYRING@ESR and to study the x-ray radiation emitted due to their interaction with electrons from the ultra-cold electron cooler. This was achieved by the deceleration of Pb^{82+} ions in the ESR from the injection energy of 400 MeV/u to 10 MeV/u, followed by subsequent transfer, storage, and cooling at CRYRING@ESR. X-ray detection was accomplished by the installation and use of dedicated chambers for mounting of x-ray windows at the straight cooler section of the storage ring at observation angles of 0° and 180°, respectively. Moreover, the x-ray emission was recorded in coincidence with down-charged Pb^{81+} ions, thus allowing for very clean x-ray spectra without any contamination caused by background events uncorrelated to the stored ion beam.

A sophisticated, time-dependent modelling of the observed x-ray spectra enabled us to reproduce quantitatively the detailed spectral information for RR of cooler electrons with the bare lead ions. Beside the prompt recombination transitions for RR into the K-, L-, and M-shells, all characteristic x-ray emission features such as the observed Lyman, Balmer, and Paschen lines are found to be well described by the applied model.

These findings were made possible by the advantageous features of the x-ray spectroscopy setup at the CRYRING@ESR electron cooler, namely beryllium vacuum windows enabling a high transmission even for x-rays in region close to a few keV, along with the excellent, overall performance of CRYRING@ESR providing very well defined electron cooled Pb^{82+} beams at an energy of as low as 10 MeV/u. Furthermore, the precisely defined observation geometry enabled us to observe all

x-ray lines without any line distortion effects and basically without any Doppler broadening. The performance of CRYRING@ESR guaranteed for cooled ion beams by applying electron cooler currents of as low as 12 mA avoiding a high-level of potentially disturbing x-ray background. As a consequence, even the complete Balmer series as well as Paschen lines of a high-Z element could be observed for the very first time in a undistorted fashion at the cooler section of CRYRING@ESR. Based on these findings we conclude that RR at electron coolers can be utilized for detailed precision spectroscopy of heavy highly charged ions. As shown in the presented study, at such low relative beam collision energies, the relative (n, l) population rate coefficients are only slightly affected by a variation of the cooler temperature since radiative recombination at low relative energies will always favor high quantum states leading finally to an Yrast-Cascade chain as observed in the current experiment. In addition, one note that a large fraction of electrons transferred via RR into excited levels of the ions have reached the ground state within our experimental observation time of about 70 ns. Indeed, our experiment proves that the major contribution to the x-ray emission arises from RR into states with principal quantum numbers up to around $n = 100$.

Further on the first preliminary results of an experimental study of the radiative decay modes from high Rydberg states to the formation of sequential Balmer series and $L \rightarrow K$ transitions in U^{90+} ions have been presented. In this experiment, the state-selective population of the substructure in excited states via RR of initially hydrogen-like uranium was studied with high resolution. This was accomplished by the implementation of two highly-granular, novel high-resolution maXs-100 detectors, placed under 0° and 180° observation angles with respect to the ion beam direction [206, 207]. The preliminary data again prove the unique potential of the experimental method based on x-ray spectroscopy at the electron cooler of CRYRING@ESR and underline the importance of the rigorous cascade simulation program for the interpretation and modeling of the measured x-ray spectra.

Chapter 8

Outlook

In order to reach a sensitivity to higher Rydberg states, a substantial improvement of the statistical accuracy is required. In addition, one may aim at the measurement of absolute x-ray line intensities in contrast to intensity ratios as applied in the present study. In a series of works on the RR processes of various bare ions (D^+, He^{2+}, C^{6+}, N^{7+}, Ne^{10+}, Si^{14+}, Ar^{18+}, Cl^{19+}, Bi^{83+}, and U^{92+}) [11, 14, 161, 209, 210], the significant rate enhancement phenomenon is found between the measured rate coefficient α_{exp} and the theoretical prediction α_{RR} in the ultra-low relative energy range ($E_{rel} < 1$ meV). At $E_{rel} = 0$ eV, the resultant rate enhancement factor $\epsilon = \alpha_{exp}/\alpha_{RR}$ is observed to take values of 1.6 (He^{2+}) to 10 (Ar^{18+}) for bare ions. As

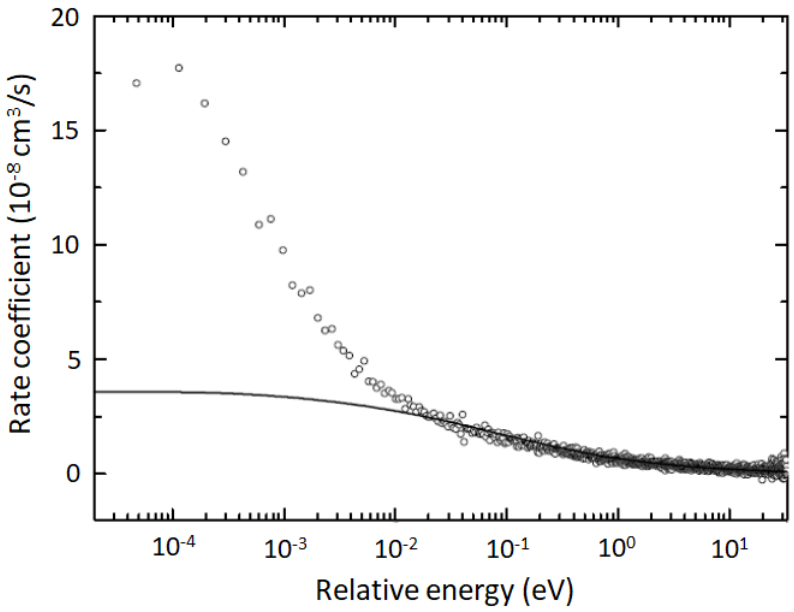

Figure 8.1: Absolute recombination rate coefficients of U^{92+} as a function of the relative energy between electron and ion [161]. The open circles represent the measurement, the solid line represents the corrected semi-classical calculations with $n_{max} = 130$, $kT_\perp = 120$ meV and $kT_\parallel = 0.1$ meV.

an example, Fig. 8.1 displays the absolute recombination rate coefficients of U^{92+} plotted against relative energy between the electron and the ion [161]. To explain

these surprising discrepancies, several theoretical models have been proposed, which range from the influence of three-body recombination and density enhancement due to plasma screening effects [211], to the effect of a magnetic field on the cross section by considering the chaotic dynamics caused by the magnetic field in the electron cooler [212] and the bound-state density model described by the Vlasov equation [160]. Future experiments conducted at the CRYRING@ESR may enhance dramatically the sensitivity reached and test the aforementioned models and explore the origin of rate enhancement observed up to now only for total RR rates. Here one may profit in particular by the strongly reduced electron beam temperature by up to two orders of magnitude (magnetic expansion at the CRYRING@ESR) as compared to the electron cooler of the ESR as depicted in Fig. 8.2.

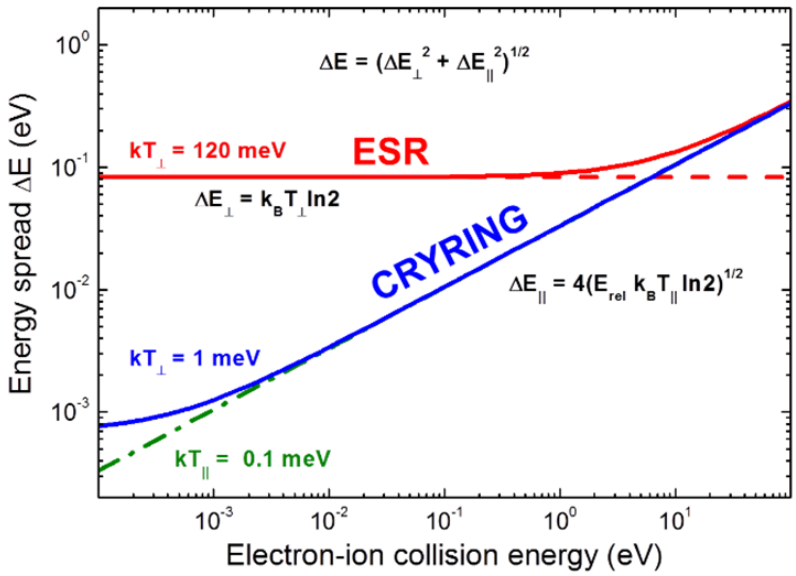

Figure 8.2: Improved energy spread in the electron cooler of the CRYRING@ESR as compared to that of the ESR.

In addition, the present study demonstrates the favorable experimental conditions for x-ray spectroscopy at the electron cooler of CRYRING@ESR for precision atomic-structure studies for high-Z one- and few-electron ions which may enable us in the near future to provide a critical test of bound state QED in strong fields close to the Schwinger limit. In the case of $1s$ Lamb shift in hydrogen-like U^{91+} ions of 464 eV, current experimental uncertainty of 4.6 eV is sensitive to the QED contributions of the first order in αZ [22]. However, to probe QED corrections which are beyond the one photon diagrams, the next generation of experiments, will be devoted to an achievement of 1 eV (2nd order QED corrections [98]) precision for the measurement of the ground state Lamb shift in hydrogen-like uranium. For this purpose, high-resolution and highly granular microcalorimeters have been developed and are currently getting prepared for such studies (see Sec. 2.4.2). The first test experiment performed at CRYRING@ESR using two maXs-100 detectors showed

very encouraging results for the ground state transitions in He-like uranium despite statistical problems. It should be emphasized here that this experiment made it possible for the first time to resolve the subcomponents of the $K\alpha_2$ ground-state transitions in a He-like ion with a nuclear charge beyond $Z = 54$, demonstrating the excellent resolution of the novel detectors (see Fig. 6.4 in Sec. 6.2). Based on these results, several breakthroughs can be expected in the near future from the experiments at CRYRING@ESR aiming at a critical test of QED in the bound state in strong fields near the Schwinger limit.

Appendix A

Formulation of radiative recombination cross sections

A.1 Nonrelativistic theory

The differential cross section for the absorption of a photon with the wave vector $\mathbf{k}$ ($k = \omega/c$) by an atom and removal of an electron with wave vector $\mathbf{k}_f = \mathbf{p}_f/\hbar$ into the continuum is defined as [213]

$$\frac{d\sigma^{ph}(\theta)}{d\Omega} = \frac{e^2}{2\pi m_e c}\frac{1}{\hbar^2}\frac{k_f}{\omega}\left|\int \psi_f^*(\mathbf{r})\mathbf{p}_{op}\cdot\hat{\mathbf{u}}_\lambda e^{i\mathbf{k}\cdot\mathbf{r}}\psi_i(\mathbf{r})d^3r\right|^2, \tag{A.1}$$

where the subscripts i and f indicate the initial state and the final state of the electron, respectively. $\hat{\mathbf{u}}_\lambda e^{i\mathbf{k}\cdot\mathbf{r}}$ is the photon wavefunction with the unit vector $\hat{\mathbf{u}}_\lambda$ for the polarization, and $\mathbf{p}_{op} = \frac{\hbar}{i}\bigtriangledown$ is the nonrelativistic current operator.

The interaction matrix element M_{fi} is given by

$$\begin{aligned} M_{fi} &= \left\langle \mathbf{p}m_s|\mathbf{p}_{op}\cdot\hat{\mathbf{u}}_\lambda e^{i\mathbf{k}\cdot\mathbf{r}}|j_i\mu_i\right\rangle \\ &= \int \psi_f^*(\mathbf{r})\mathbf{p}_{op}\cdot\hat{\mathbf{u}}_\lambda e^{i\mathbf{k}\cdot\mathbf{r}}\psi_i(\mathbf{r})d^3r, \end{aligned} \tag{A.2}$$

where $\mathbf{p}$ and m_s describe the asymptotic momentum and spin projection of the emitted electron, respectively, $\hat{\mathbf{u}}_\lambda$ is the unit polarization vector of the photon, and $|j_i\mu_i\rangle$ defines the initial bound state.

After collecting coefficients and averaging over photon polarizations, one derives the final result in the moving projectile system as [214]

$$\frac{d\sigma^{ph}(\theta)}{d\Omega} = 2\sqrt{2}\alpha^8 Z^5\left(\frac{m_e c^2}{\hbar\omega}\right)^{7/2} a_0^2\frac{\sin^2\theta}{(1-\beta\cos\theta)^4}, \tag{A.3}$$

where α is the fine-structure constant, a_0 is the Bohr radius, and β is the velocity of the emitted electron in units of speed of light.

It is clear to see that no electrons are emitted in the direction of $\mathbf{k}$. This is a direct consequence of angular momentum conservation, which forbids forward or backward emission because of the nonrelativistic absence of electron spin. The plane photon wave $e^{i\mathbf{k}\cdot\mathbf{r}}$ is said to represent the effect of retardation, i.e. the inclusion of all multipole orders. This is reflected in Eq. A.3 the denominator leads to a tilting of the angular distribution in the forward direction.

The omission of retardation effect represents the dipole approximation, i.e, replacing $e^{i\mathbf{k}\cdot\mathbf{r}} \to 1$. In this case, no angle enters into the denominator of Eq. A.3, and differential cross section is given by a pure $\sin^2\theta$ distribution. For unpolarized primary light one obtains

$$\frac{d\sigma^{ph}(\theta)}{d\Omega} \propto \sin^2\theta. \tag{A.4}$$

Cross sections for the K- and L-shell photoionization were given by Stobbe [138, 76] in closed-form expressions. For higher shells, one has to specify the bound-state wavefunction characterized by quantum numbers n, l, m in the case of H-like state in Coulomb electromagnetic fields, and the bound-state wavefunction can be expressed as [150]

$$\psi_i(\mathbf{r}) = \frac{1}{r} P_{nl}(r) Y_{lm}(\hat{\mathbf{r}}), \tag{A.5}$$

where $Y_{lm}(\hat{\mathbf{r}})$ are spherical harmonics.

For a Coulomb potential produced by the charge eZ, the final wavefunction describing an electron emitted with an asymptotic wave vector $\mathbf{k}_f$ and direction $\hat{\mathbf{k}}_f = \mathbf{k}_f/k_f$ is given by a partia$L$-wave expansion, as [150]

$$\psi_f(\mathbf{r}) = 4\pi \sum_{l=0}^{\infty} \sum_{m=-l}^{l} \frac{1}{r} \exp[i(l - \Delta_l)] F_{kl}(r) Y^*_{lm}(\hat{\mathbf{k}}_f) Y_{lm}(\hat{\mathbf{r}}), \tag{A.6}$$

where Δ_l is the Coulomb phase shift, and $\hat{\mathbf{r}} = \mathbf{r}/r$ and $\hat{\mathbf{k}}_f = \mathbf{k}_f/k_f$ are unit vectors denoting the angles.

The radial wave function P_{nl} and F_{kl} satisfy

$$\left[\frac{d^2}{dr^2} - \frac{l(l+1)}{r^2} + \frac{2Z}{r} + \begin{Bmatrix} -Z^2/n^2 \\ k^2 \end{Bmatrix}\right] \begin{Bmatrix} P_{nl}(r) \\ F_{kl}(r) \end{Bmatrix} = 0, \tag{A.7}$$

where P_{nl} is normalized as

$$\int_0^{\infty} P_{nl}(r) P_{n'l}(r) dr = \delta_{nn'} \tag{A.8}$$

and the continuum radial function is energy normalized as

$$\int_0^{\infty} F_{kl}(r) F_{k'l}(r) dr = \pi \delta(k^2 - k'^2), \tag{A.9}$$

so the asymptotic form, as $r \to \infty$, is

$$F_{kl}(r) \to \frac{1}{\sqrt{k}} \sin\left[kr - \frac{Z}{k}\ln(2kr) - \frac{l\pi}{2} + \Delta_l\right]. \tag{A.10}$$

The photoionization is the inverse of RR, with the same matrix elements. Its cross section for a hydrogenic ion is given by [163]

$$\sigma_{nl}^{ph}(k^2) = \left(\frac{4\pi\alpha a_0^2}{3}\right)\frac{n^2}{Z^2}\sum_{l'=l\pm1}\frac{l_>}{2l+1}\left(1+n^2\kappa^2\right)|g(n,l;\kappa,l')|^2. \tag{A.11}$$

with

$$g(n,l;\kappa,l') = \frac{Z^2}{n^2}\int_0^\infty P_{nl}(r) r F_{kl'}(r) dr. \tag{A.12}$$

Here, the electron kinetic energy k^2 in units of the hydrogen ionization potential is given by the energy conservation condition $\hbar\omega = (Z^2/n^2 + k^2)I_H$, where $(Z^2/n^2)I_H$ being the binding energy of the initial state in a hydrogenic atom, or an ion initialy in the state specified by the principle quantum number n and angular quantum number l. In Eq. A.11, the parameter $\kappa = k/Z$ is introduced, α is the fine-structure constant, a_0 is the Bohr radius, and $l_>$ is the greater of l and l'. Writing the scaled functions as

$$\begin{aligned} \rho &= Zr \\ \mathscr{P}_{nl}(\rho) &= Z^{-1/2}P_{nl}(r) \\ \mathscr{F}_{\kappa l}(\rho) &= Z^{-1/2}F_{kl}(r), \end{aligned} \tag{A.13}$$

the bound-free dipole matrix elements become Z independent

$$g(n,l;\kappa,l') = \frac{1}{n^2}\int_0^\infty \mathscr{P}_{nl}(\rho)\rho\mathscr{F}_{\kappa l}(\rho)d\rho. \tag{A.14}$$

By the principle of detailed balance, the relation of the cross section between photoionization and radiative recombination into a vacant shell, within a nonrelativistic treatment in the dipole approximation, is written as [153]

$$\sigma_{nl}^{RR}(k^2) = \frac{(\hbar\omega)^2}{k^2}\frac{1}{k^2 + 2m_e c^2}\sigma_{nl}^{ph}(k^2). \tag{A.15}$$

The computation task is then to evaluate the electric dipole matrix elements in Eq. A.11 and Eq. A.12. Burgess's procedure [163], which scales in the variable κ, adopted a set of simple recurrence relations allowing one to successively calculate all dipole matrix elements for a given n and a given k^2. One starts with the calculation for maximum angular momentum $l = n - 1$ and after that with the next lower $l = n - 2$. This yields the input data for recursively stepping down to all lower values of l.

The common quantity is

$$g(n,n-1;0,n)=\sqrt{\frac{\pi}{2(2n-1)!}}4(4n)^n e^{-2n}. \tag{A.16}$$

For finite values of κ, one obtains for the highest l

$$\begin{aligned}
&\underline{with\ l=n-1, l'=l+1}\\
&g(n,n-1;\kappa,n)=\sqrt{\frac{\prod_{s=1}^{n}(1+s^2k^2)}{1-e^{-2\pi/\kappa}}}\frac{e^{2n-2\kappa^{-1}arctan(n\kappa)}}{(1+n^2\kappa^2)^{n+2}}g(n,n-1;0,n),\\
&\underline{with\ l=n-1, l'=l-1}\\
&g(n,n-1;\kappa,n-2)=\frac{1}{2n}\sqrt{\frac{1+n^2\kappa^2}{1+(n-1)^2\kappa^2}}g(n,n-1;\kappa,n).
\end{aligned} \tag{A.17}$$

For the next lower value of l, one obtains

$$\begin{aligned}
&\underline{with\ l=n-2, l'=l+1}\\
&g(n,n-2;\kappa,n-1)=\frac{1}{2}\sqrt{(2n-1)(1+n^2\kappa^2)}g(n,n-1;\kappa,n),\\
&\underline{with\ l=n-2, l'=l-1}\\
&g(n,n-2;\kappa,n-3)=\frac{4+(n-1)(1+n^2\kappa^2)}{2n}\sqrt{\frac{2n-1}{1+(n-2)^2\kappa^2}}g(n,n-1;\kappa,n-2).
\end{aligned} \tag{A.18}$$

Eqs. A.16 - A.18 hence serve as the building blocks from which to step down to lower $l-$values with the aid of the following recurrence relations

$$\begin{aligned}
&2n\sqrt{[n^2-(l-1)^2][1+l^2\kappa^2]}g(n,l-2;\kappa,l-1)\\
&=[4n^2-4l^2+l(2l-1)(1+n^2\kappa^2)]g(n,l-1;\kappa,l)-2n\sqrt{[n^2-l^2][1+(l+1)^2\kappa^2]}g(n,l;\kappa,l+1),
\end{aligned} \tag{A.19}$$

and

$$\begin{aligned}
&2n\sqrt{[n^2-l^2][1+(l-1)^2\kappa^2]}g(n,l-1;\kappa,l-2)\\
&=[4n^2-4l^2+l(2l+1)(1+n^2\kappa^2)]g(n,l;\kappa,l-1)-2n\sqrt{[n^2-(l+1)^2][1+l^2\kappa^2]}g(n,l+1;\kappa,l).
\end{aligned} \tag{A.20}$$

With Eq. A.19 and Eq. A.20 one may proceed to $l=n-3$ and $l=n-4$, this process is then repeated until $l=0$ is reached. As a result, Eq. A.15 is easily evaluated for any transition $kl'\rightarrow nl$. Of course, nonexsiting matrix elements with $l\geq n$ are set equal to zero. The power of this method lies in the fact that no hypergeometric functions are to be evaluated, so that it is quite easy to design a computer program covering all cases of interest.

A.2 Relativistic theory

In analogy to Eq. A.2, the relativistic transition matrix element in this case is given by

$$\begin{aligned} M_{fi}^{exact} &= \left\langle \mathbf{p}m_s|\boldsymbol{\alpha}\cdot\hat{\mathbf{u}}_\lambda \mathrm{e}^{i\mathbf{k}\cdot\mathbf{r}}|\kappa_n\mu_n\right\rangle \\ &= \int \psi^*_{\mathbf{p},m_s}(\mathbf{r})\boldsymbol{\alpha}\cdot\hat{\mathbf{u}}_\lambda \mathrm{e}^{i\mathbf{k}\cdot\mathbf{r}}\psi_{j_n,\mu_n}(\mathbf{r})d^3r \\ &= M_{\mathbf{p},n}(m_s,\lambda,\mu_n), \end{aligned} \tag{A.21}$$

in which one assumes a single electron in the state $|\kappa_n\mu_n\rangle$ with the Dirac quantum number κ_n combining the angular momentum j_n with parity and the angular momentum projection μ_n. The quantity $\boldsymbol{\alpha}$ denotes the Dirac matrix and the exponential describes the photon wave function with wave vector $\mathbf{k}$. If the electron absorbs a photon with wave vector $\mathbf{k}$ and circular polarization $\lambda = \pm 1$, it may be emitted into a continuum state with momentum $\mathbf{p}$ and spin projection $m_s = \pm\frac{1}{2}$.

For a given photon energy $\hbar\omega$ and binding energy $|\varepsilon_n|$ of the electron in the bound initial state n, the kinetic energy T_e of the emitted electron is determined by the energy conservation condition $T_e = \hbar\omega - |\varepsilon_n| = (\gamma-1)m_ec^2$, where $\gamma = (1-v_e^2/c^2)^{-1/2}$ is the Lorentz factor of the electron moving with the speed v_e. The corresponding differential cross section for photon ionizing a single electron is given by [150]

$$\frac{d\sigma^{ph}(\theta)}{d\Omega} = \frac{\alpha m_e c^2}{4\hbar\omega}\frac{\lambda\!\!\!^{-2}_c}{2j_n+1}\sum_{\mu_n}\sum_{m_s=\pm1/2}\frac{1}{2}\sum_{\lambda=\pm1}\left|M_{\mathbf{p},n}(m_s,\lambda,\mu_n)\right|^2, \tag{A.22}$$

where $\lambda\!\!\!^{-}_c = \hbar/m_ec$ is the Compton wavelength of the electron and the quantity α denotes the fine-structure constant. Here, we have averaged over the $(2j_n+1)$ angular momentum projections μ_n in the bound state and have summed over the spin components $m_s = \pm\frac{1}{2}$ of the emitted electron. Furthermore, we have averaged over the circular polarization $\lambda = \pm 1$ of the incoming photon. Because of the summation over all other angular momentum projections μ_n, m_s, this is equivalent to taking one photon polarization, e.g., $\lambda = 1$ only.

Since for radiative recombination the direction of $\mathbf{p}$ is always fixed and well defined, it is meaningful to establish the partial cross section for photoionization from a specific magnetic substate μ_n,

$$\frac{d\sigma^{ph}_{\mu_n}(\theta)}{d\Omega} = \frac{\alpha m_e c^2}{4\hbar\omega}\lambda\!\!\!^{-2}_c\sum_{m_s=\pm1/2}\frac{1}{2}\sum_{\lambda=\pm1}\left|M_{\mathbf{p},n}(m_s,\lambda,\mu_n)\right|^2. \tag{A.23}$$

The total photoelectric cross section is obtained by integrating Eq. A.23 over the photon angles, it is given by

$$\sigma^{ph}_{\mu_n} = \frac{\alpha m_e c^2}{4\hbar\omega}\lambda\!\!\!^{-2}_c\sum_{m_s=\pm1/2}\frac{1}{2}\sum_{\lambda=\pm1}\int d\Omega_k\left|M_{\mathbf{p},n}(m_s,\lambda,\mu_n)\right|^2. \tag{A.24}$$

The total cross section can also be expressed by the diagonal matrix elements of the density matrix $P^{ph}_{\mu_n\mu_{n'}}$, as

$$\sigma^{ph}_{\mu_n} = \frac{\alpha m_e c^2}{4\hbar\omega}\lambda\!\!\!^{-2}_c P^{ph}_{\mu_n\mu_n}, \tag{A.25}$$

where the general density matrix for photoionization is defined as

$$P^{ph}_{\mu_n\mu_{n'}} = \frac{1}{2}\sum_{m_s=\pm1/2}\sum_{\lambda=\pm1}\int d\Omega_k \left\langle \mathbf{p}m_s|\boldsymbol{\alpha}\cdot\hat{\mathbf{u}}_\lambda e^{i\mathbf{k}\cdot\mathbf{r}}|\kappa_n\mu_n\right\rangle \left\langle \mathbf{p}m_s|\boldsymbol{\alpha}\cdot\hat{\mathbf{u}}_\lambda e^{i\mathbf{k}\cdot\mathbf{r}}|\kappa_n\mu'_n\right\rangle^*. \tag{A.26}$$

To further simplify the electron-photon transition matrix in Eq. A.21 for practical computations, we may need to decompose both the photon as well as continuum wavefunctions into partial waves. As pointed out in Refs. [152, 215], attention has to be paid in this case to the particular choice of the electron beam direction as the quantization axis, we shall start from a rotation of the photon field which is expressed in terms of the usual magnetic and electric multipole components as

$$\mathcal{A}^{(\lambda)}_{LM} = \mathbf{A}^{(m)}_{LM} + i\lambda\mathbf{A}^{(e)}_{LM}. \tag{A.27}$$

A rotation of the photon field is given by

$$\hat{\mathbf{u}}_\lambda e^{i\mathbf{k}\cdot\mathbf{r}} = \sqrt{2\pi}\sum_{L=1}^{\infty}\sum_{M=-L}^{L} i^L\sqrt{2L+1}\mathcal{A}^{(\lambda)}_{LM}D^L_{M\lambda}(\hat{\mathbf{k}}\to\hat{\mathbf{z}}), \tag{A.28}$$

where $D^L_{M\lambda}(\hat{\mathbf{k}}\to\hat{\mathbf{z}})$ denotes the Wigner rotation matrix [216]. The magnetic and electric multipole fields can be expressed, respectively, as [216]

$$\begin{aligned}
\mathbf{A}^{(m)}_{LM} &= j_L(kr)\mathbf{T}^M_{L,L},\\
\mathbf{A}^{(e)}_{LM} &= j_{L-1}(kr)\sqrt{\frac{L+1}{2L+1}}\mathbf{T}^M_{L,L-1} - j_{L+1}(kr)\sqrt{\frac{L}{2L+1}}\mathbf{T}^M_{L,L+1},
\end{aligned} \tag{A.29}$$

where $j_L(kr)$ is a spherical Bessel function and the vector spherical harmonics $\mathbf{T}^M_{L,L}$ are the spherical tensors of rank L, resulting from the coupling of the spherical unit vector $\boldsymbol{\xi}_m$, $m = 0, \pm1$ with the spherical harmonics Y_{lm}, that is

$$\mathbf{T}^M_{L,\Lambda} = \sum_m \langle \Lambda\ M-m\ 1\ m|L\ M\rangle\, Y_{\Lambda M-m}\boldsymbol{\xi}_m. \tag{A.30}$$

Here the symbol $< \cdots|\cdot >$ is the usual Clebsch-Gordan coefficient. Note that the parity of the magnetic and electric multipole fields $\mathbf{A}^{(m,e)}_{LM}$ is $(-1)^L$ and $(-1)^{L+1}$, respectively.

By making use of the Eq. A.29 and Eq. A.30 one can evaluate the reduced magnetic and electric multipole matrix elements as [217]

$$\begin{aligned}
\langle\kappa_a\|\,\boldsymbol{\alpha}\cdot\mathbf{A}^{(m)}_L\,\|\kappa_b\rangle &= \frac{1-(-1)^{l_a+l_b+L}}{2}\,\langle j_a\|\,\mathbf{C}^{(L)}\,\|j_b\rangle\,\bar{M}^{(m)}_{ab}(L),\\
\langle\kappa_a\|\,\boldsymbol{\alpha}\cdot\mathbf{A}^{(e)}_L\,\|\kappa_b\rangle &= \frac{1-(-1)^{l_a+l_b+L}}{2}\,\langle j_a\|\,\mathbf{C}^{(L)}\,\|j_b\rangle\,\bar{M}^{(e)}_{ab}(L).
\end{aligned} \tag{A.31}$$

where the irreducible tensor $\mathbf{C}^{(L)}$ can be written in terms of spherical harmonics as

$$\mathbf{C}^{(L)}(\theta,\phi) = \sqrt{\frac{4\pi}{2L+1}} Y_L(\theta,\phi). \tag{A.32}$$

One can evaluate the reduced matrix element of the irreducible tensor $\mathbf{C}^{(L)}$ by adopting the irreducible operator technique as

$$\langle j_a \| \, \mathbf{C}^{(L)} \, \| j_b \rangle = (-1)^L \sqrt{2j_a+1} \, \langle j_a \; 1/2 \; L \; 0 | j_b \; 1/2 \rangle \, . \tag{A.33}$$

The $\bar{M}^{(m,e)}_{ab}(L)$ involve only the radial integrals: explicitly, for magnetic type multipoles, it is achieved by

$$\bar{M}^{(m)}_{ab}(L) = \frac{-i}{\sqrt{4\pi}} \sqrt{\frac{2L+1}{L(L+1)}} (\kappa_a + \kappa_b) I^+_L(k;ab), \tag{A.34}$$

and for electric type multipoles, it is written in the velocity gauge as [217]

$$\begin{aligned} \bar{M}^{(e)}_{ab}(L) = {} & \frac{i}{\sqrt{4\pi}} \left(\sqrt{\frac{L}{(L+1)(2L+1)}} [(\kappa_a - \kappa_b) I^+_{L+1}(k;ab) + (L+1) I^-_{L+1}(k;ab)] \right) \\ & - \frac{i}{\sqrt{4\pi}} \left(\sqrt{\frac{L+1}{L(2L+1)}} [(\kappa_a - \kappa_b) I^+_{L-1}(k;ab) + L I^-_{L-1}(k;ab)] \right), \end{aligned} \tag{A.35}$$

where the radial integrals $I^\pm_\Lambda$ are expresses as

$$I^\pm_\Lambda(k;ab) = \int_0^\infty (P_a(r) Q_b(r) \pm P_b(r) Q_a(r)) j_\Lambda(kr) r^2 dr. \tag{A.36}$$

Here $P(r)$ and $Q(r)$ are the radial wave functions of the upper and lower components obtained from the stationary Dirac equation specified by the electron in bound-state or in continuum state [218, 219].

For a given initial bound state $|\kappa_n \mu_n\rangle$ and a specific partial wave $|\kappa m_s\rangle$, we can now calculate the exact relativistic magnetic and electric multipole matrix elements, respectively. That is

$$\langle \kappa m_s | \, \boldsymbol{\alpha} \cdot \mathbf{A}^{(m,e)}_{LM} \, | \kappa_n \mu_n \rangle = i \, \langle j_n \; \mu_n \; L \; M | j \; m_s \rangle \, \langle \kappa \| \, \boldsymbol{\alpha} \cdot \mathbf{A}^{(m,e)}_L \, \| \kappa_n \rangle \, . \tag{A.37}$$

From Eq. A.27, the general reduced multipole matrix element, to be used in later expressions, is

$$\langle \kappa \| \, \boldsymbol{\alpha} \cdot \boldsymbol{\mathcal{A}}^{(\lambda)}_L \, \| \kappa_n \rangle = \langle \kappa \| \, \boldsymbol{\alpha} \cdot \mathbf{A}^{(m)}_L \, \| \kappa_n \rangle + i\lambda \, \langle \kappa \| \, \boldsymbol{\alpha} \cdot \mathbf{A}^{(e)}_L \, \| \kappa_n \rangle \, . \tag{A.38}$$

Owing to the different parity of the multipole fields, either the first term or the second term will contribute in a matrix element between specified electronic states with well-defined parity.

In order to derive the general density matrix in Eq. A.26, we insert the multipole expansion given by Eq. A.27 and Eq. A.28 of the photon wave, and the expansion of Coulomb-Dirac continuum wavefunction for the free electron into partial waves $|\kappa m_s\rangle$ in the form [218]

$$|\mathbf{p}m_s\rangle = \sum_{\kappa} i^l e^{-i\Delta_\kappa} \sqrt{4\pi(2l+1)}\, \langle l\ 0\ 1/2\ m_s | j\ m_s\rangle\, |\kappa m_s\rangle\,, \tag{A.39}$$

where the summation runs over the Dirac quantum κ combining j and parity:

$$\kappa = \mp(j+1/2) \quad as \quad j = l \pm 1/2. \tag{A.40}$$

The quantity Δ_κ in Eq. A.39 is called the Coulomb phase shift [218, 8] which arises due to the $-Z/r$ nuclear potential of a point-like charge.

If one is interested in μ_n-dependent total cross sections whereby the RR photons are not observed, one has to integrate over the directions of incidence of the photon, From the relation [216]

$$\int D^{L'*}_{M'\lambda} D^{L}_{M\lambda} d\Omega_k = \frac{4\pi}{2L+1} \delta_{M'M} \delta_{L'L}, \tag{A.41}$$

it follows that with the choice of the electron direction as the z axis, the density matrix becomes diagonal in M and hence in $\mu_n = m_s - M$.

Finally, the density matrix for photoionization becomes

$$P^{ph}_{\mu_n\mu_{n'}} = \delta_{\mu_n\mu_{n'}} 16\pi^3 \sum_{\lambda} \sum_{m_s} \sum_{L,M} \left| \sum_{\kappa} i^{-l} e^{i\Delta_\kappa} \sqrt{2l+1}\, \langle l\ 0\ 1/2\ m_s | j\ m_s\rangle\, \langle \kappa m_s |\, \boldsymbol{\alpha} \cdot \mathcal{A}^{(\lambda)}_{LM}\, | \kappa_n \mu_n \rangle \right|^2 . \tag{A.42}$$

Owing to Eq. A.26 and Eq. A.42, the total cross section for photoionization of a specific substate μ_n is written as

$$\begin{aligned} \sigma^{ph}_{\mu_n} &= \frac{\alpha m_e c^2}{4\hbar\omega} \lambda\!\!\!^{-2}_c P^{ph}_{\mu_n\mu_n} \\ &= 16\pi^3 \frac{\alpha m_e c^2}{4\hbar\omega} \lambda\!\!\!^{-2}_c \sum_{\lambda} \sum_{m_s} \sum_{L,M} \left| \sum_{\kappa} i^{-l} e^{i\Delta_\kappa} \sqrt{2l+1}\, \langle l\ 0\ 1/2\ m_s | j\ m_s\rangle\, \langle \kappa m_s |\, \boldsymbol{\alpha} \cdot \mathcal{A}^{(\lambda)}_{LM}\, | \kappa_n \mu_n \rangle \right|^2 . \end{aligned} \tag{A.43}$$

By the principle of detailed balance, the relation of the cross section between photoionization and radiative recombination into a vacant shell with a specific magnetic substate μ_n, within a relativistic treatment in multipole decomposion of the photon wave and partial-wave expansion of the electronic continuum wavefunction, is written as [153]

$$\sigma^{RR}_{\mu_n} = \frac{(\hbar\omega)^2}{T_e} \frac{1}{T_e + 2m_e c^2} \sigma^{ph}_{\mu_n}. \tag{A.44}$$

The partial cross section for photoionization averaged over the initial substates μ_n is expressed by the diagonal elements of the density matrix, as

$$\frac{d\sigma^{ph}(\theta)}{d\Omega} = \frac{\alpha m_e c^2}{4\hbar\omega} \frac{\lambda\!\!\!^{-2}_c}{2j_n+1} \sum_{\mu_n} P^{ph}_{\mu_n\mu_n}(\hat{\mathbf{k}}) \tag{A.45}$$

in terms of the angle-dependent density matrix $P^{ph}_{\mu_n\mu_n}(\hat{\mathbf{k}})$ which is obtained from Eq. A.26 by discarding the integration over the photon direction.

By inserting the multipole expansion A.28 into Eq. A.21 and combining the Wigner rotation matrix $D^L_{M\lambda}(\hat{\mathbf{k}} \rightarrow \hat{\mathbf{z}})$ [216], we obtain the differential cross section as [152]

$$\begin{aligned}\frac{d\sigma^{ph}(\theta)}{d\Omega} = \frac{\alpha m_e c^2}{4\hbar\omega}\lambda\!\!\!^{-2}_c \frac{2\pi}{2j_n+1} \sum_{\mu_n,m_s}\sum_{L\bar{L}} (-1)^{M+1} i^{L-\bar{L}} \\ \times \sqrt{(2L+1)(2\bar{L}+1)} \sum_{\nu} \left\langle L\ M\ \bar{L}\ -M|\nu\ 0\right\rangle \left\langle L\ \lambda\ \bar{L}\ -\lambda|\nu\ 0\right\rangle \\ \times \left\langle \mathbf{p}m_s\right| \boldsymbol{\alpha}\cdot\mathcal{A}^{(\lambda)}_{LM}\left|\kappa_n\mu_n\right\rangle \left\langle \mathbf{p}m_s\right| \boldsymbol{\alpha}\cdot\mathcal{A}^{(\lambda)}_{\bar{L}M}\left|\kappa_n\mu_n\right\rangle^* P_\nu(\cos\theta),\end{aligned} \tag{A.46}$$

where $P_\nu(\cos\theta)$ is Legendre polynomials, the matrix elements of the operator $\boldsymbol{\alpha}\cdot\mathcal{A}^{(\lambda)}_{LM}$ are further calculated stepwise by following Eqs. A.37 - A.39. In all cases, $M = m_s - \mu_n$. Of course, if one is interested in the separation into spin-flip and non-spin-flip contributions in photoionization of $s_{1/2}$ states over the whole angular range in a relativistic description, one has to use Eq. A.46 and simply discard the summation over the electron spin $m_s = \pm 1/2$.

Bibliography

[1] F Bosch. "The planned heavy-ion storage-cooler rings: powerful tools for new experiments in nuclear and atomic physics". In: *Physica Scripta* 36.4 (1987), p. 730.

[2] R Schuch et al. "Storage rings, a new tool for atomic physics". In: *Nuclear Instruments and Methods in Physics Research Section B: Beam Interactions with Materials and Atoms* 43.3 (1989), pp. 411–424.

[3] D Habs et al. "First experiments with the Heidelberg test storage ring TSR". In: *Nuclear Instruments and Methods in Physics Research Section B: Beam Interactions with Materials and Atoms* 43.3 (1989), pp. 390–410.

[4] M A Levine et al. "The electron beam ion trap: A new instrument for atomic physics measurements". In: *Physica Scripta* 1988.T22 (1988), p. 157.

[5] M A Levine et al. "The use of an electron beam ion trap in the study of highly charged ions". In: *Nuclear Instruments and Methods in Physics Research Section B: Beam Interactions with Materials and Atoms* 43.3 (1989), pp. 431–440.

[6] M Lestinsky et al. "Physics book: CRYRING@ ESR". In: *The European Physical Journal Special Topics* 225.5 (2016), pp. 797–882.

[7] M Durante et al. "All the fun of the FAIR: fundamental physics at the facility for antiproton and ion research". In: *Physica Scripta* 94.3 (2019), p. 033001.

[8] J Eichler and Th Stöhlker. "Radiative electron capture in relativistic ion–atom collisions and the photoelectric effect in hydrogen-like high-Z systems". In: *Physics Reports* 439.1-2 (2007), pp. 1–99.

[9] George B Rybicki and Alan P Lightman. *Radiative processes in astrophysics*. John Wiley & Sons, 1991.

[10] Th Stöhlker et al. "Test of strong-field QED". In: *The physics of multiply and highly charged ions*. Springer, 2003, pp. 351–386.

[11] A Wolf et al. "Experiments with highly-charged ions in the storage ring TSR". In: *Zeitschrift für Physik D Atoms, Molecules and Clusters* 21.1 (1991), S69–S75.

[12] T Quinteros et al. “Recombination of D^+ and He^+ ions with low-energy free electrons”. In: *Physical Review A* 51.2 (1995), p. 1340.

[13] H Gao et al. “Observation of enhanced electron-ion recombination rates at very low energies”. In: *Physical review letters* 75.24 (1995), p. 4381.

[14] A Hoffknecht et al. “Recombination of bare Bi^{83+} ions with electrons”. In: *Physical Review A* 63.1 (2000), p. 012702.

[15] D Liesen et al. “X-rays from radiative electron capture of highly-charged heavy ions in an electron cooler”. In: *Zeitschrift für Physik D Atoms, Molecules and Clusters* 30.4 (1994), pp. 307–313.

[16] M Pajek and R Schuch. “X-rays from recombination of bare ions with electrons in an electron cooler”. In: *Nuclear Instruments and Methods in Physics Research Section B: Beam Interactions with Materials and Atoms* 98.1-4 (1995), pp. 165–169.

[17] H F Beyer et al. “X rays from radiative electron capture of free cooling electrons for precise Lamb-shift measurements at high Z: Au^{78+}”. In: *Physics Letters A* 184.6 (1994), pp. 435–439.

[18] R Reuschl et al. “State-selective x-ray studies of radiative recombination into bare and H-like uranium at threshold energies”. In: *Physical Review A* 77.3 (2008), p. 032701.

[19] D Banaś et al. “Subshell-selective x-ray studies of radiative recombination of U^{92+} ions with electrons for very low relative energies”. In: *Physical Review A* 92.3 (2015), p. 032710.

[20] R Reuschl et al. “The Balmer spectrum of H-like uranium produced by radiative recombination at low velocities”. In: *Radiation Physics and Chemistry* 75.11 (2006), pp. 1740–1743.

[21] Ph Pfäfflein et al. “Integration of maXs-type microcalorimeter detectors for high-resolution x-ray spectroscopy into the experimental environment at the CRYRING@ ESR electron cooler”. In: *Physica Scripta* 97.11 (2022), p. 114005.

[22] A Gumberidze et al. “Quantum electrodynamics in strong electric fields: the ground-state lamb shift in hydrogenlike uranium”. In: *Physical Review Letters* 94.22 (2005), p. 223001.

[23] H F Beyer et al. “Measurement of the ground-state lambshift of hydrogenlike uranium at the electron cooler of the ESR”. In: *Zeitschrift für Physik D Atoms, Molecules and Clusters* 35.3 (1995), pp. 169–175.

[24] C Pies et al. “maXs: microcalorimeter arrays for high-resolution X-ray spectroscopy at GSI/FAIR”. In: *Journal of Low Temperature Physics* 167.3 (2012), pp. 269–279.

[25] B Franzke. “The heavy ion storage and cooler ring project ESR at GSI”. In: *Nuclear Instruments and Methods in Physics Research Section B: Beam Interactions with Materials and Atoms* 24 (1987), pp. 18–25.

[26] M Steck and Yu A Litvinov. “Heavy-ion storage rings and their use in precision experiments with highly charged ions”. In: *Progress in Particle and Nuclear Physics* (2020), p. 103811.

[27] D A Knapp et al. “A high-energy electron beam ion trap for production of high-charge high-Z ions”. In: *Nuclear Instruments and Methods in Physics Research Section A: Accelerators, Spectrometers, Detectors and Associated Equipment* 334.2-3 (1993), pp. 305–312.

[28] R E Marrs, S R Elliott, and D A Knapp. “Production and trapping of hydrogenlike and bare uranium ions in an electron beam ion trap”. In: *Physical Review Letters* 72.26 (1994), p. 4082.

[29] P H Mokler and Th Stöhlker. “The physics of highly charged heavy ions revealed by storage/cooler rings”. In: *Advances in Atomic, Molecular, and Optical Physics*. Vol. 37. Elsevier, 1996, pp. 297–370.

[30] Th Stöhlker et al. “Equilibrium charge state distributions for relativistic heavy ions”. In: *Nuclear Instruments and Methods in Physics Research Section B: Beam Interactions with Materials and Atoms* 61.4 (1991), pp. 408–410.

[31] D Möhl. “Phase space cooling in storage rings”. In: *Physica Scripta* 1988.T22 (1988), p. 21.

[32] H Poth. “Electron cooling: theory, experiment, application”. In: *Physics Reports* 196.3-4 (1990), pp. 135–297.

[33] F Nolden et al. “Stochastic cooling at the ESR”. In: *Nuclear Instruments and Methods in Physics Research Section A: Accelerators, Spectrometers, Detectors and Associated Equipment* 441.1-2 (2000), pp. 219–222.

[34] F Nolden et al. “Experience and prospects of stochastic cooling of radioactive beams at GSI”. In: *Nuclear Instruments and Methods in Physics Research Section A: Accelerators, Spectrometers, Detectors and Associated Equipment* 532.1-2 (2004), pp. 329–334.

[35] M Steck et al. “Anomalous temperature reduction of electron-cooled heavy ion beams in the storage ring ESR”. In: *Physical Review Letters* 77.18 (1996), p. 3803.

[36] M Steck et al. “Electron cooling experiments at the ESR”. In: *Nuclear Instruments and Methods in Physics Research Section A: Accelerators, Spectrometers, Detectors and Associated Equipment* 532.1-2 (2004), pp. 357–365.

[37] N Angert and B Franzke. "The GSI heavy ion facility". In: *Challenges and Goals for Accelerators in the XXI Century* (2016), pp. 279–306.

[38] D Möhl et al. "Physics and technique of stochastic cooling". In: *Physics Reports* 58.2 (1980), pp. 73–102.

[39] S Van Der Meer. "Stochastic cooling and the accumulation of antiprotons". In: *Reviews of Modern Physics* 57.3 (1985), p. 689.

[40] D Möhl. "The status of stochastic cooling". In: *Nuclear Instruments and Methods in Physics Research Section A: Accelerators, Spectrometers, Detectors and Associated Equipment* 391.1 (1997), pp. 164–171.

[41] J Marriner. "Stochastic cooling overview". In: *Nuclear Instruments and Methods in Physics Research Section A: Accelerators, Spectrometers, Detectors and Associated Equipment* 532.1-2 (2004), pp. 11–18.

[42] F Nolden et al. "Stochastic cooling developments at GSI". In: *AIP Conference Proceedings*. Vol. 821. 1. American Institute of Physics. 2006, pp. 177–184.

[43] G I Budker, GI Dimov, and VG Dudnikov. "Proceedings of the International Symposium on Electron and Positron Storage Rings, Saclay, 1966". In: (1966).

[44] G I Budker et al. "Experimental studies of electron cooling". In: *Part. Accel.* 7 (1976), pp. 197–211.

[45] J Bosser. *Workshop on beam cooling and related topics*. Tech. rep. European Organization for Nuclear Research, 1994.

[46] W Geithner et al. "Status and outlook of the CRYRING@ ESR project". In: *Hyperfine Interactions* 238.1 (2017), p. 13.

[47] H Danared et al. "Technical Design Report: LSR Low-energy Storage Ring". In: *Manne-Siegbahn Laboratory, Stockholm University, version* 1 (2011).

[48] M Lestinsky et al. *CRYRING@ESR: A study group report*. `https://www.gsi.de/fileadmin/SPARC/documents/Cryring/ReportCryring_40ESR.PDF`.

[49] Z Andelkovic et al. *Technical Design Report: Experimental Instrumentation of CRYRING@ESR*. `https://www.gsi.de/fileadmin/Atomphysik/Sparc/Technical_Design_Report__CRYRING_Instrumentation.pdf`.

[50] F Herfurth et al. "The low energy storage ring CRYRING@ ESR". In: *Proc. COOL'13* (2013).

[51] M J Barnes et al. "Injection and extraction magnets: kicker magnets". In: *arXiv preprint arXiv:1103.1583* (2011).

[52] S Litvinov et al. “A novel scheme for fast extraction of low energy beams from the ESR to the CRYRING”. In: *GSI Report* 1 (2015), p. 433.

[53] Frank Herfurth. *The commissioning of CRYRING@ESR*. URL: https://indico-jsc.fz-juelich.de/event/48/session/31/contribution/78/material/slides/.

[54] H. -J Kluge et al. “HITRAP: a facility at GSI for highly charged ions”. In: *Advances in Quantum Chemistry* 53 (2008), pp. 83–98.

[55] H Danared. “Electron cooling at CRYRING with an expanded electron beam”. In: *Nuclear Instruments and Methods in Physics Research Section A: Accelerators, Spectrometers, Detectors and Associated Equipment* 391.1 (1997), pp. 24–31.

[56] H Danared et al. “Electron cooling with an ultracold electron beam”. In: *Physical Review Letters* 72.24 (1994), p. 3775.

[57] Glenn F Knoll. *Radiation detection and measurement*. John Wiley & Sons, 2010.

[58] S H Byun. *Lecture notes: Radioisotopes and Radiation Methodology (Chapter 8)*. https://www.science.mcmaster.ca/radgrad/programs/courses.html?id=224.

[59] L Fleischmann et al. “Metallic magnetic calorimeters for X-ray spectroscopy”. In: *IEEE transactions on applied superconductivity* 19.2 (2009), pp. 63–68.

[60] C Enss et al. “Metallic magnetic calorimeters for particle detection”. In: *Journal of low temperature physics* 121.3 (2000), pp. 137–176.

[61] A Fleischmann, C Enss, and GM Seidel. “Metallic magnetic calorimeters”. In: *Cryogenic particle detection* (2005), pp. 151–216.

[62] A Fleischmann et al. “Metallic magnetic calorimeters”. In: *AIP Conference Proceedings*. Vol. 1185. 1. American Institute of Physics. 2009, pp. 571–578.

[63] D Hengstler et al. “Towards FAIR: first measurements of metallic magnetic calorimeters for high-resolution X-ray spectroscopy at GSI”. In: *Physica Scripta* 2015.T166 (2015), p. 014054.

[64] C Pies et al. “Metallic magnetic calorimeters for high precision QED tests at GSI/FAIR”. In: *AIP Conference Proceedings*. Vol. 1185. 1. American Institute of Physics. 2009, pp. 603–606.

[65] C Enss and D Mccammon. “Physical principles of low temperature detectors: ultimate performance limits and current detector capabilities”. In: *Journal of Low Temperature Physics* 151.1 (2008), pp. 5–24.

[66] F Salvat, J M Fernández-Varea, and J Sempau. "PENELOPE-2006: A code system for Monte Carlo simulation of electron and photon transport". In: *Workshop proceedings*. Vol. 4. 6222. Nuclear Energy Agency, Organization for Economic Co-operation and Development. 2006, p. 7.

[67] S Kempf et al. "Physics and applications of metallic magnetic calorimeters". In: *Journal of Low Temperature Physics* 193.3 (2018), pp. 365–379.

[68] C R Bates et al. "Reproducibility and calibration of MMC-based high-resolution gamma detectors". In: *Applied Physics Letters* 109.2 (2016), p. 023513.

[69] Daniel Hengstler. "Development and characterization of two-dimensional metallic magnetic calorimeter arrays for the high-resolution x-ray spectroscopy". PhD thesis. Citeseer, 2017.

[70] S Kraft-Bermuth et al. "Microcalorimeters for x-ray spectroscopy of highly charged ions at storage rings". In: *Atoms* 6.4 (2018), p. 59.

[71] Alexandre Gumberidze. "Experimental studies of the ground state QED corrections in H-and He-like Uranium". PhD thesis. Citeseer, 2003.

[72] W E Lamb Jr and R C Retherford. "Fine structure of the hydrogen atom by a microwave method". In: *Physical Review* 72.3 (1947), p. 241.

[73] C R Nave. "HyperPhysics: Hydrogen Spectrum". In: *Georgia State University* (2006).

[74] J J Balmer. "A Note on the Spectral Lines of Hydrogen". In: *Atomic Spectra: The Commonwealth and International Library: Selected Readings in Physics* (2013), p. 101.

[75] P A M Dirac. "The quantum theory of the electron". In: *Proceedings of the Royal Society of London. Series A, Containing Papers of a Mathematical and Physical Character* 117.778 (1928), pp. 610–624.

[76] Hans A Bethe and Edwin E Salpeter. *Quantum mechanics of one-and two-electron atoms*. Springer Science & Business Media, 1977.

[77] Joannes Theodorus Maria Walraven. *Atomic Physics Lectures*. University of Amsterdam, 2021.

[78] P J Mohr. "Energy levels of hydrogen-like atoms predicted by quantum electrodynamics, $10 \leq Z \leq 40$". In: *Atomic Data and Nuclear Data Tables* 29.3 (1983), pp. 453–466.

[79] W R Johnson and G Soff. "The lamb shift in hydrogen-like atoms, $1 \leq Z \leq 110$". In: *Atomic Data and Nuclear Data Tables* 33.3 (1985), pp. 405–446.

[80] M Niering et al. "Measurement of the hydrogen 1 s-2 s transition frequency by phase coherent comparison with a microwave cesium fountain clock". In: *Physical Review Letters* 84.24 (2000), p. 5496.

[81] B De Beauvoir et al. "Metrology of the hydrogen and deuterium atoms: Determination of the Rydberg constant and Lamb shifts". In: *The European Physical Journal D-Atomic, Molecular, Optical and Plasma Physics* 12.1 (2000), pp. 61–93.

[82] Th Stöhlker et al. "1s Lamb Shift in Hydrogenlike Uranium Measured on Cooled, Decelerated Ion Beams". In: *Physical Review Letters* 85.15 (2000), p. 3109.

[83] J P Briand et al. "Observation and measurement of $n = 2 \rightarrow n = 1$ transitions of hydrogenlike and heliumlike uranium". In: *Physical Review Letters* 65.22 (1990), p. 2761.

[84] Th Stöhlker et al. "Ground-state Lamb shift for hydrogenlike uranium measured at the ESR storage ring". In: *Physical Review Letters* 71.14 (1993), p. 2184.

[85] P J Mohr. "Self-energy correction to one-electron energy levels in a strong Coulomb field". In: *Physical Review A* 46.7 (1992), p. 4421.

[86] P J Mohr and G Soff. "Nuclear size correction to the electron self-energy". In: *Physical Review Letters* 70.2 (1993), p. 158.

[87] A N Artemyev, V M Shabaev, and V A Yerokhin. "Relativistic nuclear recoil corrections to the energy levels of hydrogenlike and high-Z lithiumlike atoms in all orders in αZ". In: *Physical Review A* 52.3 (1995), p. 1884.

[88] G Plunien and G Soff. "Nuclear-polarization contribution to the Lamb shift in actinide nuclei". In: *Physical Review A* 51.2 (1995), p. 1119.

[89] G Plunien and G Soff. "Erratum: Nuclear-polarization contribution to the Lamb shift in actinide nuclei". In: *Physical Review A* 53.6 (1996), p. 4614.

[90] V A Yerokhin and V M Shabaev. "Two-loop self-energy correction in H-like ions". In: *Physical Review A* 64.6 (2001), p. 062507.

[91] V A Yerokhin, P Indelicato, and V M Shabaev. "Two-loop self-energy correction in high-Z hydrogenlike ions". In: *Physical Review Letters* 91.7 (2003), p. 073001.

[92] Th Beier and G Soff. "Källén-Sabry contribution to the lamb-shift in hydrogenlike atoms". In: *Zeitschrift für Physik D Atoms, Molecules and Clusters* 8.2 (1988), pp. 129–134.

[93] S M Schneider, W Greiner, and G Soff. "Kallen-Sabry energy shift for hydrogenlike atoms with finite size nuclei". In: *Journal of Physics B: Atomic, Molecular and Optical Physics* 26.17 (1993), p. L529.

[94] H Persson et al. "Accurate vacuum-polarization calculations". In: *Physical Review A* 48.4 (1993), p. 2772.

[95] H Persson et al. "Second-order self-energy–vacuum-polarization contributions to the Lamb shift in highly charged few-electron ions". In: *Physical Review A* 54.4 (1996), p. 2805.

[96] I Lindgren et al. "Second-order QED corrections for few-electron heavy ions: reducible Breit-Coulomb correction and mixed self-energy-vacuum polarization correction". In: *Journal of Physics B: Atomic, Molecular and Optical Physics* 26.16 (1993), p. L503.

[97] V A Yerokhin, P Indelicato, and V M Shabaev. "Two-loop QED corrections with closed fermion loops". In: *Physical Review A* 77.6 (2008), p. 062510.

[98] V A Yerokhin and V M Shabaev. "Lamb shift of $n = 1$ and $n = 2$ states of hydrogen-like atoms, $1 \leq Z \leq 110$". In: *Journal of Physical and Chemical Reference Data* 44.3 (2015), p. 033103.

[99] H F Beyer et al. "FOCAL: X-ray optics for accurate spectroscopy". In: *Spectrochimica Acta Part B: Atomic Spectroscopy* 59.10-11 (2004), pp. 1535–1542.

[100] H F Beyer et al. "Crystal optics for precision x-ray spectroscopy on highly charged ions - conception and proof". In: *Journal of Physics B: Atomic, Molecular and Optical Physics* 48.14 (2015), p. 144010.

[101] A N Artemyev et al. "QED calculation of the $n = 1$ and $n = 2$ energy levels in He-like ions". In: *Physical Review A* 71.6 (2005), p. 062104.

[102] M Trassinelli et al. "Observation of the $2p_{3/2} \rightarrow 2s_{1/2}$ intra-shell transition in He-like uranium". In: *EPL (Europhysics Letters)* 87.6 (2009), p. 63001.

[103] M Trassinelli et al. "Doppler-tuned Bragg Spectroscopy of Excited Levels in He-Like Uranium: a discussion of the uncertainty contributions". In: *Journal of Physics: Conference Series*. Vol. 163. 1. IOP Publishing. 2009, p. 012026.

[104] C T Chantler et al. "Testing three-body quantum electrodynamics with trapped Ti^{20+} ions: Evidence for a Z-dependent divergence between experiment and calculation". In: *Physical Review Letters* 109.15 (2012), p. 153001.

[105] P Beiersdorfer and G V Brown. "Experimental study of the x-ray transitions in the heliumlike isoelectronic sequence: Updated results". In: *Physical Review A* 91.3 (2015), p. 032514.

[106] I Lindgren et al. "Full QED calculations of two-photon exchange for helium-like systems: Analysis in the Coulomb and Feynman gauges". In: *Physical Review A* 51.2 (1995), p. 1167.

[107] V M Shabaev and I G Fokeeva. "Calculation formulas for the reducible part of the two-photon-exchange diagrams in the QED of multicharged ions". In: *Physical Review A* 49.6 (1994), p. 4489.

[108] D R Plante, W R Johnson, and J Sapirstein. "Relativistic all-order many-body calculations of the $n = 1$ and $n = 2$ states of heliumlike ions". In: *Physical Review A* 49.5 (1994), p. 3519.

[109] K T Cheng et al. "Relativistic configuration-interaction calculations for the ground state and $n = 2$ singlet states of heliumlike ions". In: *Physical Review A* 50.1 (1994), p. 247.

[110] V A Yerokhin and V M Shabaev. "Accurate calculation of self-energy screening diagrams for high Z helium-like atoms". In: *Physics Letters A* 207.5 (1995), pp. 274–280.

[111] V A Yerokhin, A N Artemyev, and V M Shabaev. "Two-electron self-energy contribution to the ground-state energy of helium-like ions". In: *Physics Letters A* 234.5 (1997), pp. 361–366.

[112] R E Marrs, S R Elliott, and Th Stöhlker. "Measurement of two-electron contributions to the ground-state energy of heliumlike ions". In: *Physical Review A* 52.5 (1995), p. 3577.

[113] A Gumberidze et al. "Electron-electron interaction in strong electromagnetic fields: The two-electron contribution to the ground-state energy in He-like uranium". In: *Physical Review Letters* 92.20 (2004), p. 203004.

[114] Th Stöhlker et al. "Charge-exchange cross sections and beam lifetimes for stored and decelerated bare uranium ions". In: *Physical Review A* 58.3 (1998), p. 2043.

[115] E Träbert. "Atomic lifetime measurements with ion traps of many sizes". In: *Physica Scripta* 61.3 (2000), p. 257.

[116] R Marrus and P J Mohr. "Forbidden transitions in one-and two-electron atoms". In: *Advances in atomic and molecular physics*. Vol. 14. Elsevier, 1979, pp. 181–224.

[117] G W F Drake. "Spontaneous two-photon decay rates in hydrogenlike and heliumlike ions". In: *Physical Review A* 34.4 (1986), p. 2871.

[118] V G Pal'chikov. "Relativistic transition probabilities and oscillator strengths in hydrogen-like atoms". In: *Physica Scripta* 57.5 (1998), p. 581.

[119] O Jitrik and C F Bunge. "Transition probabilities for hydrogen-like atoms". In: *Journal of Physical and Chemical Reference Data* 33.4 (2004), pp. 1059–1070.

[120] F A Parpia and W R Johnson. "Radiative decay rates of metastable one-electron atoms". In: *Physical Review A* 26.2 (1982), p. 1142.

[121] Th Stöhlker et al. "Strong alignment observed for the time-reversed photoionization process studied in relativistic collisions with bare uranium ions". In: *Physical Review Letters* 79.17 (1997), p. 3270.

[122] A Surzhykov et al. "Lyman-α_1 Decay in Hydrogenlike Ions: Interference between the E1 and M2 Transition Amplitudes". In: *Physical Review Letters* 88.15 (2002), p. 153001.

[123] O Jitrik and C F Bunge. "Salient features of electric and magnetic multipole transition probabilities of hydrogen-like systems". In: *Physica Scripta* 69.3 (2004), p. 196.

[124] G W F Drake. "Energy level calculations and E1M1 two photon transition rates in two electron U^{90+}". In: *Nuclear Instruments and Methods in Physics Research Section B: Beam Interactions with Materials and Atoms* 9.4 (1985), pp. 465–470.

[125] N M Cann and A J Thakkar. "Oscillator strengths for S-P and P-D transitions in heliumlike ions". In: *Physical Review A* 46.9 (1992), p. 5397.

[126] W R Johnson and C D Lin. "Relativistic random phase approximation applied to atoms of the He isoelectronic sequence". In: *Physical Review A* 14.2 (1976), p. 565.

[127] C D Lin, W R Johnson, and A Dalgarno. "Radiative decays of the $n = 2$ states of He-like ions". In: *Physical Review A* 15.1 (1977), p. 154.

[128] J Hata and I P Grant. "MCDF calculations of wavelengths and radiative lifetimes in helium-like ions". In: *Journal of Physics B: Atomic and Molecular Physics* 14.13 (1981), p. 2111.

[129] J Krause. "Relativistic variational theory for two-electron atoms". In: *Physical Review A* 34.5 (1986), p. 3692.

[130] E Lindroth and S Salomonson. "Relativistic calculation of the $2^3\,S^1 \rightarrow 1^1\,S^0$ magnetic dipole transition rate and transition energy for heliumlike argon". In: *Physical Review A* 41.9 (1990), p. 4659.

[131] G Feinberg and J Sucher. "Calculation of the Decay Rate for $2^3\,S^1 \rightarrow 1^1\,S^0$ One Photon in Helium". In: *Physical Review Letters* 26.12 (1971), p. 681.

[132] W R Johnson and C P Lin. "Dirac-Hartree-Fock calculation of the $2^3\,S^1 \rightarrow 1^1\,S^0$ transition rates for the He isoelectronic sequence". In: *Physical Review A* 9.4 (1974), p. 1486.

[133] W R Johnson, D R Plante, and J Sapirstein. "Relativistic calculations of transition amplitudes in the helium isoelectronic sequence". In: *Advances in Atomic, Molecular and Optical Physics* 35 (1995).

[134] Heinrich F Beyer and Viateheslav P Shevelko. *Introduction to the physics of highly charged ions*. CRC Press, 2016.

[135] M F Gu. "Indirect X-ray line-formation processes in iron L-shell ions". In: *The Astrophysical Journal* 582.2 (2003), p. 1241.

[136] M F Gu. "The flexible atomic code". In: *Canadian Journal of Physics* 86.5 (2008), pp. 675–689.

[137] P J Storey and D G Hummer. "Fast computer evaluation of radiative properties of hydrogenic systems". In: *Computer Physics Communications* 66.1 (1991), pp. 129–141.

[138] M Stobbe. "Zur quantenmechanik photoelektrischer prozesse". In: *Annalen der Physik* 399.6 (1930), pp. 661–715.

[139] M Bell and J S Bell. "Capture of cooling electrons by cool protons". In: *Part. Accel* 12 (1982), p. 49.

[140] H F Beyer, O Guzman, and D Liesen. "On the total recombination between cooling electrons and heavy ions". In: *Part. Accel.* 24 (1989), pp. 163–175.

[141] G Kilgus et al. "Dielectronic recombination of hydrogenlike oxygen in a heavy-ion storage ring". In: *Physical Review Letters* 64.7 (1990), p. 737.

[142] H A Kramers. "XCIII. On the theory of X-ray absorption and of the continuous X-ray spectrum". In: *The London, Edinburgh, and Dublin Philosophical Magazine and Journal of Science* 46.275 (1923), pp. 836–871.

[143] W Gordon. "Zur berechnung der matrizen beim wasserstoffatom". In: *Annalen der Physik* 394.8 (1929), pp. 1031–1056.

[144] A Burgess and M J Seaton. "A general formula for the calculation of atomic photo-ionization cross sections". In: *Monthly Notices of the Royal Astronomical Society* 120.2 (1960), pp. 121–151.

[145] I A Kotelnikov and A I Milstein. "Electron radiative recombination with a hydrogen-like ion". In: *Physica Scripta* 94.5 (2019), p. 055403.

[146] Y Hahn and D W Rule. "Direct radiative capture of high-energy electrons by atomic ions". In: *Journal of Physics. B, Atomic and Molecular Physics* 10.13 (1977), pp. 2689–2698.

[147] Y Hahn. "Electron-ion recombination processes-an overview". In: *Reports on Progress in Physics* 60.7 (1997), p. 691.

[148] D J McLaughlin and Y Hahn. "Scaling behavior of radiative recombination cross sections and rate coefficients". In: *Physical Review A* 43.3 (1991), p. 1313.

[149] D J McLaughlin and Y Hahn. "Erratum: Scaling behavior of radiative recombination cross sections and rate coefficients [Phys. Rev. A 43, 1313 (1991)]". In: *Physical Review A* 45.7 (1992), p. 5317.

[150] R H Pratt, A Ron, and H K Tseng. "Atomic photoelectric effect above 10 keV". In: *Reviews of Modern physics* 45.2 (1973), p. 273.

[151] A Ichihara, T Shirai, and J Eichler. "Radiative electron capture in relativistic atomic collisions". In: *Physical Review A* 49.3 (1994), p. 1875.

[152] J Eichler, A Ichihara, and T Shirai. "Alignment caused by photoionization and in radiative electron capture into excited states of hydrogenic high-Z ions". In: *Physical Review A* 58.3 (1998), p. 2128.

[153] A Ichihara and J Eichler. "Cross sections for radiative recombination and the photoelectric effect in the K, L, and M shells of one-electron systems with $1 \leq Z \leq 112$ calculated within an exact relativistic description". In: *Atomic Data and Nuclear Data Tables* 74.1 (2000), pp. 1–121.

[154] H Brysk and C D Zerby. "Photoelectric cross sections in the keV range". In: *Physical Review* 171.2 (1968), p. 292.

[155] M Pajek and R Schuch. "Radiative recombination of bare ions with low-energy free electrons". In: *Physical Review A* 45.11 (1992), p. 7894.

[156] R Schuch, W Zong, and N R Badnell. "Recombination of cooled highly charged ions with low-energy electrons". In: *International journal of mass spectrometry* 192.1-3 (1999), pp. 225–243.

[157] Lyman Spitzer. *Physics of fully ionized gases*. Interscience, New York, 1956.

[158] M Pajek and R Schuch. "Radiative recombination in the low-energy regime". In: *Physics Letters A* 166.3-4 (1992), pp. 235–237.

[159] Igor I Sobelman. *Atomic spectra and radiative transitions*. Vol. 12. Springer Science & Business Media, 2012.

[160] C Heerlein, G Zwicknagel, and C Toepffer. "Radiative recombination enhancement of bare ions in storage rings with electron cooling". In: *Physical Review Letters* 89.8 (2002), p. 083202.

[161] W Shi et al. "Recombination of U^{92+} ions with electrons". In: *The European Physical Journal D-Atomic, Molecular, Optical and Plasma Physics* 15.2 (2001), pp. 145–154.

[162] C Brandau et al. "Recombination of U^{89+} ions with free electrons at the ESR". In: *Hyperfine interactions* 114.1 (1998), pp. 263–266.

[163] A Burgess. "Tables of hydrogenic photoionization cross-sections and recombination coefficients". In: *Memoirs of the Royal Astronomical Society* 69 (1965), p. 1.

[164] E B Menz et al. “First DR experiment at CRYRING@ESR”. In: *Helmholtz Institute Jena Annual Report 2020* (2021), p. 55.

[165] E Spindler, H-D Betz, and F Bell. “Influence of retardation on the angular distribution of radiative electron capture”. In: *Physical Review Letters* 42.13 (1979), p. 832.

[166] A Ichihara and J Eichler. “Angle-differential cross sections for radiative recombination and the photoelectric effect in the K, L, and M shells of one-electron systems calculated within an exact relativistic description”. In: *Atomic Data and Nuclear Data Tables* 79.2 (2001), pp. 187–222.

[167] Jörg Eichler. *Lectures on ion-atom collisions: from nonrelativistic to relativistic velocities*. Elsevier, 2005.

[168] M Kleber and D H Jakubassa. “Radiative electron capture in heavy-ion collisions”. In: *Nuclear Physics A* 252.1 (1975), pp. 152–162.

[169] R Anholt et al. “Observation of radiative capture in relativistic heavy-ion—atom collisions”. In: *Physical review letters* 53.3 (1984), p. 234.

[170] S D Oh and R H Pratt. “Connection between the atomic photoeffect and internal conversion”. In: *Physical Review A* 13.4 (1976), p. 1463.

[171] A Ron et al. “Relativistic, retardation, and multipole effects in photoionization cross sections: Z, n, and l dependence”. In: *Physical Review A* 50.2 (1994), p. 1312.

[172] Th Stöhlker et al. “Radiative electron capture in relativistic heavy-ion atom collisions”. In: *Nuclear Instruments and Methods in Physics Research Section B: Beam Interactions with Materials and Atoms* 98.1-4 (1995), pp. 235–239.

[173] Th Stöhlker et al. “Radiative electron capture studied in relativistic heavy-ion–atom collisions”. In: *Physical Review A* 51.3 (1995), p. 2098.

[174] Th Stöhlker et al. “Angular distribution studies for the time-reversed photoionization process in hydrogenlike uranium: The identification of spin-flip transitions”. In: *Physical Review Letters* 82.16 (1999), p. 3232.

[175] Th Stöhlker et al. “Near-threshold photoionization of hydrogenlike uranium studied in ion-atom collisions via the time-reversed process”. In: *Physical Review Letters* 86.6 (2001), p. 983.

[176] Th Stöhlker et al. “Radiative electron capture studied for bare, decelerated uranium ions”. In: *Physica Scripta* 2001.T92 (2001), p. 432.

[177] Th Stöhlker et al. “L-subshell resolved photon angular distribution of radiative electron capture into He-like uranium”. In: *Physical Review Letters* 73.26 (1994), p. 3520.

[178] J Eichler, A Ichihara, and T Shirai. "Photon angular distributions from radiative electron capture in relativistic atomic collisions". In: *Physical Review A* 51.4 (1995), p. 3027.

[179] J Eichler. "Angular distribution of de-excitation X-rays from radiative electron capture in relativistic atomic collisions". In: *Nuclear Physics A* 572.1 (1994), pp. 147–152.

[180] A Surzhykov, S Fritzsche, and Th Stöhlker. "Photon–photon angular correlations in the radiative recombination of bare high-Z ions". In: *Journal of Physics B: Atomic, Molecular and Optical Physics* 35.17 (2002), p. 3713.

[181] G Weber et al. "Direct determination of the magnetic quadrupole contribution to the Lyman-α_1 transition in a hydrogenlike ion". In: *Physical Review Letters* 105.24 (2010), p. 243002.

[182] A Surzhykov, S Fritzsche, and Th Stöhlker. "Two-step radiative recombination of polarized electrons into bare, high-Z ions". In: *Nuclear Instruments and Methods in Physics Research Section B: Beam Interactions with Materials and Atoms* 205 (2003), pp. 391–394.

[183] A Surzhykov, S Fritzsche, and Th Stöhlker. "Polarization of the Lyman–α1 Line Following the Radiative Recombination of Bare, High-Z Ions". In: *Hyperfine interactions* 146.1 (2003), pp. 35–40.

[184] Th Stöhlker et al. "Angular correlation and polarization studies for radiative electron capture into high-Z ions". In: *Physica Scripta* 2004.T110 (2004), p. 384.

[185] M Lestinsky et al. "CRYRING@ ESR: present status and future research". In: *Physica Scripta* 2015.T166 (2015), p. 014075.

[186] M Steck et al. "Recent results on equilibrium temperatures and cooling forces with electron cooled heavy ion beams in the ESR". In: *Proceedings of EPAC*. 1994, p. 1197.

[187] F M Kröger et al. "New Setup for X-Ray Spectroscopy at the CRYRING@ESR Electron Cooler". In: *Helmholtz Institute Jena Annual Report 2019* (2020), p. 45.

[188] K Rinn et al. "Development of single-particle detectors for keV ions". In: *Review of Scientific Instruments* 53.6 (1982), pp. 829–837.

[189] A Müller et al. "Experimental measurements of field effects on dielectronic recombination cross sections and Rydberg product-state distributions". In: *Physical Review A* 36.2 (1987), p. 599.

[190] W Zong et al. "Low-energy recombination of Ne^{7+}". In: *Journal of Physics B: Atomic, Molecular and Optical Physics* 31.16 (1998), p. 3729.

[191] C Biedermann et al. "Study of radiative recombination into deuterium Rydberg states". In: *Journal of Physics B: Atomic, Molecular and Optical Physics* 28.3 (1995), p. 505.

[192] S Schippers et al. "Storage ring measurement of the C IV recombination rate coefficient". In: *The Astrophysical Journal* 555.2 (2001), p. 1027.

[193] S Böhm et al. "Measurement of the field-induced dielectronic-recombination-rate enhancement of O^{5+} ions differential in the Rydberg quantum number n". In: *Physical Review A* 65.5 (2002), p. 052728.

[194] M Pajek and R Schuch. "Plasma effects in three-body recombination of high-Z bare ions with electrons". In: *Physica Scripta* 1999.T80B (1999), p. 307.

[195] Th Stöhlker et al. "First experiment with decelerated bare uranium ions conducted at the ESR storage ring". In: *Hyperfine Interactions* 108.1 (1997), pp. 29–38.

[196] A Gumberidze et al. "X-ray transitions studied for decelerated bare and H-like uranium ions at the ESR electron cooler". In: *Nuclear instruments & methods in physics research. Section B, Beam interactions with materials and atoms* 205 (2003), pp. 374–377.

[197] Th Stöhlker et al. "Ground state transitions in one-and two-electron Bi projectiles". In: *Physics Letters A* 168.4 (1992), pp. 285–290.

[198] Th Stöhlker et al. "Polarization and angular correlation studies of X-rays emitted in relativistic ion-atom collisions". In: *The European Physical Journal Special Topics* 169.1 (2009), pp. 5–14.

[199] H F Beyer et al. "X-ray transitions associated with electron capture into bare dysprosium". In: *Journal of Physics B: Atomic, Molecular and Optical Physics* 26.9 (1993), p. 1557.

[200] P H Mokler et al. "Radiative electron capture: a tool for structure studies of heavy few-electron ions". In: *Zeitschrift für Physik D Atoms, Molecules and Clusters* 21.3 (1991), pp. 197–200.

[201] D P Dewangan and J Eichler. "Charge exchange in energetic ion-atom collisions". In: *Physics Reports* 247.2-4 (1994), pp. 59–219.

[202] L J Curtis. "A diagrammatic mnemonic for calculation of cascading level populations". In: *American Journal of Physics* 36.12 (1968), pp. 1123–1125.

[203] H Gao et al. "Role of electron-ion recombination processes in the lifetime of stored D^+ beams". In: *Physical Review A* 54.4 (1996), p. 3005.

[204] H Hirayama et al. *The EGS5 code system*. Tech. rep. United States. Department of Energy, 2005.

[205] D Banaś et al. “Two-photon energy distribution from the decay of the $2\ ^1S_0$ state in He-like uranium”. In: *Physical Review A* 87.6 (2013), p. 062510.

[206] Philip Pfäfflein. “PhD thesis in preparation 2023”. PhD thesis.

[207] Felix Martin Kröger. “PhD thesis in preparation 2023”. PhD thesis.

[208] Th Stöhlker et al. “SPARC collaboration: new strategy for storage ring physics at FAIR”. In: *Hyperfine Interactions* 227.1 (2014), pp. 45–53.

[209] H Gao et al. “Energy and charge dependence of the rate of electron-ion recombination in cold magnetized plasmas”. In: *Journal of Physics B: Atomic, Molecular and Optical Physics* 30.14 (1997), p. L499.

[210] O Uwira et al. “Recombination measurements at low energies with Ar^{16+} and Ar^{18+} ions in a dense, cold electron target”. In: *Hyperfine interactions* 108.1 (1997), pp. 167–175.

[211] Q Spreiter and C Toepffer. “A screening model for density enhancement near ions at rest in magnetized electron plasmas”. In: *Journal of Physics B: Atomic, Molecular and Optical Physics* 33.12 (2000), p. 2347.

[212] M Hörndl et al. “Classical dynamics of enhanced low-energy electron-ion recombination in storage rings”. In: *Physical Review A* 74.5 (2006), p. 052712.

[213] Hans A Bethe and Roman Jackiw. *Intermediate quantum mechanics*. CRC Press, 1997.

[214] Walter Heitler. *The quantum theory of radiation*. Courier Corporation, 1984.

[215] A Surzhykov, S Fritzsche, and Th Stöhlker. “Photon polarization in the radiative recombination of high-Z, hydrogen-like ions”. In: *Physics Letters A* 289.4-5 (2001), pp. 213–218.

[216] Morris Edgar Rose. *Elementary theory of angular momentum*. New York: Wiley, 1957.

[217] I P Grant. “Gauge invariance and relativistic radiative transitions”. In: *Journal of Physics B: Atomic and Molecular Physics* 7.12 (1974), p. 1458.

[218] Jörg Eichler and Walter Ernst Meyerhof. *Relativistic atomic collisions*. Academic Press, 1995.

[219] A Surzhykov, P Koval, and S Fritzsche. “Algebraic tools for dealing with the atomic shell model. I. Wavefunctions and integrals for hydrogen-like ions”. In: *Computer Physics Communications* 165.2 (2005), pp. 139–156.

Acknowledgements

I would like to acknowledge both Helmholtz Institute Jena and the class of doctoral fellowship from Chinese Scholarship Council for their financial support, and I am indebted to the donors in providing me complete academic freedom in this research.

An immense thank you to my PhD supervisor Prof. Thomas Stöhlker, who provides me the unique opportunity to do this PhD work, support and guidance throughout the project from him has been invaluable. The course of interaction of high-energy radiation with matter at the University of Jena was a huge influence and without which I would have never followed this path.

I'm extremely grateful to Dr. Günter Weber and to Dr. Alexandre Gumberidze, who have largely contribute to my understanding of physics and supported my work.

For the friendly environment and for their great support I would like to express my deepest appreciation to my colleagues from the Atomic Physics Department of GSI: T. Over, Dr. Z. Andelkovic, Dr. A. Bräuning-Demian, Dr. R. J. Chen, Dr. D. Dmytriiev, Dr. O. Forstner, Dr. F. Herfurth, M. O. Herdrich, Dr. P.-M. Hillenbrand, Dr. A. Kalinin, F. M. Kröger, Dr. M. Lestinsky, Prof. Yu. A. Litvinov, E. B. Menz, W. Middents, T. Morgenroth, Dr. N. Petridis, Ph. Pfäfflein, Dr. M. S. Sanjari, Dr. R. S. Sidhu, Dr. U. Spillmann, Prof. S. Schippers, Prof. R. Schuch, Dr. S. Trotsenko, Dr. L. Varga, Dr. G. Vorobyev.

I would also like to acknowledge the Helmholtz Graduate School for Hadron and Ion Research (HGS-HIRe) and the Research School for Advanced Photon Science (RS-APS) for funding my PhD study and for providing good educational opportunities (soft-skill courses and lecture weeks). In particular, I am also thankful to Christoph Hahn, Dr. Renate Märtin for their warm help to me on the affairs within the RS-APS and the Helmholtz Institute Jena.

A special acknowledgement is devoted to my "alma mater" — Lanzhou University, where I officially started my study in physics. I thank heartily Dr. Aixiang Yang and Prof. Jianxiong Shao for bringing me into the field of atomic physics and also for encouraging me studying abroad.

Last but not least, I could not have undertaken this journey without encouragement from my parents, who have greatly supported me in everything, as well as to my friends. To everyone who helped me to get to this stage, my sincere gratitude.

Public appearances

Peer-reviewed publications:

1. B. Zhu and Th. Stöhlker. Radiative recombination studies for bare lead ions interacting with low-energy electrons. Atoms **11**, 2 (2023).

2. B. Zhu and Th. Stöhlker. Calculation of radiative recombination rates for hydrogen-like ions at high-Z. Accepted by Proceedings of Science "FAIR Next Generation Scientists – 7th Edition Workshop" (2023).

3. B. Zhu, A. Gumberidze, T. Over, Z. Andelkovic, A. Bräuning-Demian, R. J. Chen, D. Dmytriiev, O. Forstner, C. Hahn, F. Herfurth, M. O. Herdrich, P.-M. Hillenbrand, A. Kalinin, F. M. Kröger, M. Lestinsky, Yu. A. Litvinov, E. B. Menz, W. Middents, T. Morgenroth, N. Petridis, Ph. Pfäfflein, M. S. Sanjari, R. S. Sidhu, U. Spillmann, R. Schuch, S. Schippers, S. Trotsenko, L. Varga, G. Vorobyev and Th. Stöhlker. X-ray emission associated with radiative recombination for Pb^{82+} ions at threshold energies. Phys. Rev. A **105**, 052804 (2022).

4. Ph. Pfäfflein, S. Allgeier, S. Bernitt, A. Fleischmann, M. Friedrich, Ch. Hahn, D. Hengstler, M. O. Herdrich, A. Kalinin, F. M. Kröger, P. Kuntz, M. Lestinsky, B. Löher, E. B. Menz, T. Over, U. Spillmann, G. Weber, B. Zhu, Ch. Enss and Th. Stöhlker. Integration of maXs-type microcalorimeter detectors for high-resolution x-ray spectroscopy into the experimental environment at the CRYRING@ESR electron cooler. Phys. Scr. **97**, 114005 (2022).

Annual reports:

1. B. Zhu, A. Gumberidze, T. Over, U. Spillmann, G. Weber, and Th. Stöhlker. Characteristic x-ray transitions in hydrogen-like lead ions recorded at the CRYRING @ESR electron cooler. HI Jena annual report 2021, p.53 (2022).

2. B. Zhu, G. Weber, and Th. Stöhlker. Accurate modelling of radiative recombination into high-Z ions at the CRYRING@ESR electron cooler. HI Jena annual report 2020, p.58 (2021).

3. B. Zhu, P. Pfäfflein, C. Hahn, H. Lin, G. Weber, and Th. Stöhlker. Characterization of a YAP: Ce scintillator for ion detection. HI Jena annual report 2019, p.47 (2020).

Talks:

1. B. Zhu, X-ray Emission Associated with Radiative Recombination Studied at the CRYRING@ESR Electron Cooler. 19th SPARC Topical Workshop (Hybrid), 6-9 September 2022, Jena in Germany.

2. B. Zhu, X-ray Emission Study Performed for Hydrogen-like Lead Ions at the Electron Cooler of CRYRING@ESR, FAIR Next Generation Scientists – 7th Edition Workshop, 23-27 May 2022, Paralia in Greece.

Conference posters:

1. B. Zhu, G. Weber, T. Over, et al. X-ray Emission Study Performed for Hydrogen-like Lead Ions at the Electron Cooler of CRYRING@ESR, 20th International Conference on the Physics of Highly Charged Ions (Online), 29 August-03 September 2022, Matsue in Japan

2. B. Zhu, G. Weber, T. Over, *et al.* X-ray Emission Study Performed for H-like Lead at the Electron Cooler of CRYRING@ESR, 766th WE-Heraeus Seminar on High-Precision Measurements and Searches for New Physics, 09-13 May 2022, Bad Honnef in Germany.

3. B. Zhu, G. Weber, T. Over, et al. X-ray Emission Study Performed for H-like Lead at the Electron Cooler of CRYRING@ESR, 10th International Conference on New Frontiers in Physics (Hybrid), 23 August-02 September 2021, Crete in Greece.

4. B. Zhu, G. Weber, T. Over, *et al.* X-ray Emission of H-like Lead Observed at the Electron Cooler of CRYRING@ESR, 32nd International Conference on Photonic, Electronic and Atomic Collisions (Online), 20-27 July 2021, Ottawa in Canada.

Ehrenwörtliche Erklärung

Ich erkläre hiermit ehrenwörtlich, dass ich die vorliegende Arbeit selbstständig, ohne unzulässige Hilfe Dritter und ohne Benutzung anderer als der angegebenen Hilfsmittel und Literatur angefertigt habe. Die aus anderen Quellen direkt oder indirekt übernommenen Daten und Konzepte sind unter Angabe der Quelle gekennzeichnet

Bei der Auswahl und Auswertung folgenden Materials haben mir die nachstehend aufgeführten Personen in der jeweils beschriebenen Weise entgeltlich/unentgeltlich geholfen:

1. Prof. Dr. Thomas Stöhlker

Weitere Personen waren an der inhaltlich-materiellen Erstellung der vorliegenden Arbeit nicht beteiligt. Insbesondere habe ich hierfür nicht die entgeltliche Hilfe von Vermittlungs- bzw. Beratungsdiensten (Promotionsberater oder andere Personen) in Anspruch genommen. Niemand hat von mir unmittelbar oder mittelbar geldwerte Leistungen für Arbeiten erhalten, die im Zusammenhang mit dem Inhalt der vorgelegten Dissertation stehen.

Die Arbeit wurde bisher weder im In- noch im Ausland in gleicher oder ähnlicher Form einer anderen Prüfungsbehörde vorgelegt.

Die geltende Promotionsordnung der Physikalisch-Astronomischen Fakultät ist mir bekannt.

Ich versichere ehrenwörtlich, dass ich nach bestem Wissen die reine Wahrheit gesagt und nichts verschwiegen habe.

Ort, Datum Unterschrift d. Verfassers